Tool Path Optimization for Free Form Surfaces

By

A. Canberk Manav

A Thesis Submitted to the

Graduate School of Engineering

In Partial Fulfillment of the Requirements for

The Degree of

Master of Science

In

Mechanical Engineering

Koc University

September 2009

ABSTRACT

This study presents a novel approach to generate optimized tool paths for free form surfaces that are commonly used in automotive, aerospace, biomedical, home appliance manufacturing and die/mold industries. The developed tool path optimization approach can handle various objectives under multiple constraints. Due to anisotropic geometry of free form surfaces, tool paths become one of the most critical factors for determining cutting forces. Here, firstly the concept of force-minimal tool path generation is introduced and demonstrated for free form surfaces. Nowadays, process planning engineers must select the tool paths only from a set of ordinary tool paths available in CAM systems. These standard tool paths available in CAM systems are generated based on geometric computations only, not considering mechanics of processes, and most often these paths are away being optimum for free form surfaces. Here, a new methodology is introduced the first time for generating the tool paths based on process mechanics for globally minimizing the cutting forces for any given free form surface [2].

Also, a novel solution for multi-criteria tool path optimization is presented by the assistance of developed mathematical solution within the physical relationship between the mean resultant force, production time and scallop height. In various CNC applications, the geometric dimensions and tolerances of designed geometry need to be precise to get sufficient results. Therefore the production time is basically spend to be removed the surface scallop height to keep designed geometries as requested. This spent time should be as short as possible, since fast production and quick delivery are most of the important things in today's competitive world. Including scallop height and production time and the effective forces on the tool as three-criteria, this triple bounded problem is solved in this study by using the objective weighting based algorithm which creates tool paths according to intended criteria is dominating on the others. Additionally, to mention about general solution, the algorithm need to contain free form surfaces and the experimental validation are also covered in the content of this text.

ACKNOWLEDGEMENTS

I would like to express my gratitude to my advisor, Dr. Ismail Lazoglu for his expert guidance and I would also like to thank Dr. Metin Turkay and Dr. Erhan Budak for reading this thesis and involving in my thesis committee.

I acknowledge Yavuz Murtezaoglu and ModuleWorks GmbH for solid based engagement model and Mustafa Kaymakci for mechanistic ball end-mill cutting force model for free form surfaces.

I would also like to thank all of my friends in the office, especially to H. Sinan Bank for his support.

And finally, I would like to thank to my brother Tugberk Manav, especially to my mother Nesrin Manav and my father Yucel Manav for their life-long love, for the kind of encouragement and support they have provided me throughout my entire education life, and for their absolute confidence in me. This thesis as well as my all previous success is dedicated to my family.

TABLE OF CONTENTS

LIST OF FIGURES

LIST OF TABLES

NOMENCLATURE

x, y, z	coordinates of cutting edge of ball-end mill
R_b	ball radius of the cutter
r	tool radius in x-y plane at a point defined by ψ
β	lag angle between the tangent line at the tip of the flute and axial location z
x_c, y_c, z_c	coordinates of cutting edge of ball-end mill according to rotating frame
φ_{st}	start angle of each discrete disc
φ_{ex}	exit angle of each discrete disc
α	feed inclination angle
t_c	instantaneous chip load
t_x	feed per tooth
θ	immersion angle of cutting point
f_h	vertical feed component in mm/min
f_v	horizontal feed component in mm/min
ψ	cutting element position angle
$(t_c)_{knnew}$	new instantaneous undeformed chip thickness for ball-end mill cutter
dA_c	differential chip load
F_r, F_ψ, F_t	cutting forces in tangential, radial and axial directions
dF_X, dF_Y, dF_Z	differential cutting forces in x, y, and z directions
K_{rc}, $K_{\psi c}$, K_{tc}	tangential, radial and axial cutting force coefficients in milling
K_{re}, $K_{\psi e}$, K_{te}	tangential, radial and axial edge force coefficients in milling
Ω	rotation angle of flute
N_f	number of flutes
n	flute number
β_k	lag angle between the k^{th} discrete point on cutting edge and the cutter tip

ω	spindle speed in revolution per minute
f	feedrate of the cutter in mm per minute
$d\theta$	Integration angle
dz	Integration height
CL	number of G codes for the tool path
$\Delta\theta$	discrete cutting element rotation angle
f_s	data sampling frequency
z_1	measured upper boundary distance from the tip of the sphere part
z_2	measured lower boundary distance from the tip of the sphere part
Δd	distance between consecutive two CL points
t	required time in seconds between consecutive two CL points
V	swept volume in mm^3 between consecutive two CL points
MRR	material removal rate in mm^3/sec
C	total number of CL points in the tool path
f_1	original constant feedrate for the tool path in mm/min
f_2	twice of f_1 feedrate in mm/min
F_1	maximum resultant force value in Newton for the f_1 feedrate value
F_2	maximum resultant force value in Newton for the f_2 feedrate value
$f_{lim,i}$	scheduled feedrate value in mm/min for the i^{th} CL point
$F_{lim,i}$	limiting constant resultant force threshold value
nod	normal offset distance
m	modal mass for transfer function
ζ	damping ratio for transfer function
w_n	natural frequency for transfer function
δ	cutter deflection at point z,
I	area moment of inertia of cutter in mm^4
E	young modulus in MPa

L	projection length of cutter in mm
Ls	length of shank part of the cutter
Ks	clamping stiffness
zc	applied force center in mm
dz	rise of cutter tip in z direction in mm
D	diameter of the cutter in mm
d	effective diameter of the cutter in mm
δ_t	resultant cutter bending deflection
δ_s	deflection of the shank
δ_f	deflection of the flute
δ_{sf}	deflection of the shank due to deflection angle
δ_{st}	deflection of the clamping part which is calculated from the stiffness
ϕ_s	deflection angle
e_f	error due to feed force
e_{cf}	error due to cross feed force
e_{total}	total error in z direction
s_1	stepover distance
s_2	scallop height

Chapter 1
INTRODUCTION

Free form surfaces, nowadays, are widely used in several industries for instance automotive, aerospace, biomedical, home appliance and die–mold industries. They are used in great diversity of products such as dies of automotive body panels, turbine blades, impellers of artificial heart pumps. There might be various reasons for instance aero-fluid dynamics efficiency, ergonomic or aesthetic incentives for designing and manufacturing free form surfaces. Recent developments in CAM systems allowed manufacturing of complex free form part geometries. One of the most critical issues in process planning with CAM is selection of an appropriate tool path for machining of the free form surfaces. Unfortunately, in today's tool path creator CAM programs are just based on geometric calculations. Therefore, created tool paths are far from being optimized in terms of production engineers' perspective.

Presently, production engineers choose the tool paths among conventional tool paths (zig, zigzag, follow periphery, radial tool paths, etc) in commercial CAM software. However, these conventional tool paths would not be optimum for all the free form geometries to be milled. It is shown that by using conventional tool paths the magnitude of cutting forces are varied.

The scallop height is one of the road blocks for cycle time delays to achieve designed part. Generally the tool paths are used to decrease the scallop height by decreasing step over of the CAM settings, which increase cycle time and in these CAM packages. The resultant forces are not calculated, therefore, there is risk of damages on tool is high, deflection of tools and surface form errors on manufactured parts are larger with compare to optimized tool paths. To keep cutting forces, scallop height and cycle time is consisted always minimum in milling, because, firstly, low cutting forces mean longer tool life, less breakage and bending, low on surface defects on part; secondly low cycle times mean fast production and quick delivery in competitive industry and finally lower scallop mean better surface quality and achievement of desired part geometry.

In this study, Lazoglu and Kaymakci's [1] previous enhanced model of free form surface milling mechanics is used to simulate cutting forces. The model is developed

according to the previous studies of Guzel and Lazoglu [2], and Erdim [3]. For tool path optimization part, criteria map (or maps) is selected (e.g. force map, scallop height map, cycle time map) and the appropriate network optimization algorithm is used either the problem is single or multi-criteria.

Chapter 2 provides necessary background and literature review on tool path optimization. Tool path selection strategies in CNC operations, single & multi-criteria network optimization prediction of cutting forces and scallop modeling are reviewed.

Chapter 3 describes force-based (single-criteria) tool path optimization by studying Lazoglu and Kaymakci's [1] enhanced model of free form surface milling mechanics, solid based engagement model of Modulworks and Lazoglu and Kaymakci's mechanistic cutting force model including the determination of the cutting constants (calibration process). The force mapping and MCC-transformed (Minimum Cost Connections) tool path algorithm as single-criteria optimization routine [4] is introduced and described in detail. Performed validation tests are also presented to compare simulated and experimental cutting forces.

Chapter 4 describes multi-criteria optimization including mean cutting force, mean scallop height and total cycle time as selected 3-criteria to optimize. Multi-criteria genetic algorithm and objective weighting based algorithm are studied in this chapter. The 3D scallop model is represented to form the scallop height map. Force, scallop height and cycle time maps are optimized using objective weighting algorithm due to the shorter computation time. For 3-criteria optimization, all non-dominated (pareto optimal) solutions are found as the optimal solutions which form a pareto surface on the boundary of the objective space which includes all possible solutions. Using the pareto surface, various tool paths are determined with specified threshold values and minimization criteria for the objectives and experimental validation tests are performed.

Chapter 2
LITERATURE REVIEW

Since ball-end milling is widely used process in industry, there is lots of research done on this subject. However, studies in the literature on process optimizations consider only geometrical constraints such as distance traveled and cycle time. Literature review about this thesis can be divided into four main sections; modeling of cutting forces in ball-end milling, optimization algorithms for networks, tool path optimization with specified constraints and objectives, and tool path and scallop height analysis.

Cutting forces occurred during machining is one of the most important parameter improving the productivity and part quality, because deflection, tool breakage, stability, surface quality and form errors are mainly influenced by cutting forces.

Determination of chip formation is the first step in mechanistic modeling of cutting forces. Early study of Martelotti [5] showed that the path of the tool tooth is trochoidal, rather than circular because of the combined rotation and translation of the tool towards the workpiece. Martelotti also claimed that when the feed per tooth is much smaller than the tool radius, circular tool path assumption is valid and the error is negligible.

There are many cutting force analyses for ball-end mills with helix angle in literature. Koenigsberger et al [6]. used experimentally determined cutting coefficients and related chip load to cutting forces. However, calibration method used in this study is far from the physics of the process, because empirical curve fitting technique was used instead of mechanistic or orthogonal calibration. Armarego and Deshpande [7] more accurately predicted cutting force by introducing cutting edge force component.

Mechanistic approach had limitations on milling with complex tools which have variable geometry along the axis of tool. Therefore, Yucesan and Altintas [8] presented a semi-mechanistic model to predict shear and frictional load distribution on the rake faces of ball-end mills. As an alternative to the mechanistic approach, orthogonal cutting parameters were developed in order to eliminate the necessity of new calibration tests when the tool geometry changes. Armarego and Whitfield [9]

applied the orthogonal to oblique transformations on cutting force predictions. The idea behind this study is to divide the tool geometry into segments of oblique cutting processes. Budak, Altintas and Armarego [10] identified the material properties such as shear flow stress and friction angle from orthogonal turning tests. This study presented an accurate model to transform the orthogonal cutting parameters to cutting force coefficients. Yang and Park [11] used a similar approach and they used cutting parameters of orthogonal tests and simplified the analysis by approximating oblique cutting on each flute by infinitesimal orthogonal processes. Lazoglu and Liang [12] established a closed-form model for ball-end mill process in the frequency domain using an angular convolution technique.

Studies in the literature on single and multi-criteria network optimization are mostly offered known network solutions such as minimum spanning tree (MST) and minimum cost traveling salesman. Minimum spanning tree (MST) is of high importance in network optimization. The study of She [13] proposes minimum cost tree algorithms for 2D maps with different optimization constraints and objectives including least unit-cost first (LUF), least path-cost first (LPF), min-cost resource first (MCF) and most available first (MAV). Furthermore, Zhou and Gen [14] developed a genetic algorithm for determining multi criteria minimum spanning tree which is used for giving specific weights for discrete objectives and constraints in the optimization.

When the previous studies about tool path optimization are considered, there are not many research are performed in the literature. Studies in the literature on tool path optimization consider only geometrical constraints such as distance traveled and cycle time. Weinert et al. [15] and Altan et al. [146] emphasized on the influence of milling directions and the importance of tool path generation for process optimization of die and mold manufacturing, respectively. Lauwers et al. [17] introduced an extended CAM system for multi-axes milling and integrating tool path generation. The system performs verification of each generated cutter location and applies a collision avoidance algorithm. Castelino et al. [18] optimized the tool path by minimizing the airtime during machining with the proper order of the discrete path segments by solving a generalized traveling salesman problem (TSP). Rangarajan and Dornfeld [19] demonstrated the advantages of orienting the part and tool path and efficient programming for face and rough end milling processes.

Lacalle et al. [20] aimed to increase the surface quality however their algorithm does not consider the problem as a whole single system and stays local in each segment of tool path calculation. Therefore, it does not perform a global optimization. Makhanov et al. [21] perform a geometrical tool path optimization for milling where a single closed Hamiltonian path with minimum distance traveled is obtained for a surface grid by using a space filling curve algorithm. Feng and Su [22] optimized the feed rate with the tool path based on calculation of cutting forces and machining errors in 3D plane surface machining. Budak et al. [23], improved cycle time in sculptured surface machining though force modeling. Monreal and Rodriguez [24] presented the influence of tool path strategy on the cycle time of high speed milling. They investigated the effect of tool path orientation angle on the cycle time. Kim and Choi [25] compared the machining efficiency of direction-parallel tool path with contour-parallel tool path. Other than objectives regarding to geometry or cycle time, Manav et. al. introduced a resultant cutting force based tool path optimization for three-axis free form surface ball end milling [26, 27].

Since complex free-form surfaces are widely used industry, surface form error, scallop formation, tool path generation and comparison are getting more attractive to scholars. Lazoglu [28] employed a Boolean approach in the model and in addition to predicting the cutting forces, the model determined the resulting surface topography and scallop height variations along the workpiece for given cutter/workpiece geometries and CL file. Researchers mainly focus on tool path generations, there is little research on tool path evaluation and comparing tool path selection strategies for complex sculptured surfaces. Chen et. al [29] developed a model to calculate scallop formation in ball-end milling process. Feng et. al. [30] offered a constant scallop height model and an iterative method for tool path generation for three-axis sculptured surface machining Lee et. al [31] presents a new approach to mesh based tool path generation for obtaining constant scallop heights. Agrawal et. al [32] shows that there is a provision for minimizing machining time while implementing isoscallop machining. Kim et. al [33] present a cutter location (CL) surface deformation approach for constant scallop height tool path generation from triangular mesh. Choi et. al [34] develop a tool path generation method for free-form surface machining using Bézier curves and surfaces where cutter location (CL) and cutter contact (CC) points are estimated.

Chapter 3
FORCE BASED (SINGLE-CRITERIA) TOOLPATH OPTIMIZATION

3.1. Introduction

In CNC part programs used in vertical machining center, the cutting tool needs to move along a prescribed path. It is typically described by a sequence of curves. These curves are determined by combining the predefined Cutter Location (CL) points. For the determination of the optimum tool path for cutting of a free form surface, the cutting forces are minimized and limited below a threshold. In order to determine a reference value for the cutting forces in each direction for all CL points referring a uniform Cartesian mesh, a force map is constructed showing reference values for all possible cutting forces from each CL point to its neighbors. This reference map is obtained by pre-computation combining engagement and force simulations of slot cutting operations in each direction. The force simulation of the optimized path and its experimental validation are obtained and compared.

Since ball-end milling is widely used process in industry, tool path generation and optimization to increase productivity with decreasing cycle time and increasing surface quality in machining is a challenging subject for research. Research on this topic can be divided into two parts; optimization algorithms for networks and tool path optimization with specified constraints and objectives.

In cutting operations with step-over percentage lower than 100% of the cutting tool diameter, slot cutting forces for each connection give only reference values for the actual cutting forces since early chip removal near a CL point affects the prospective engagement at that point. For this case, a dynamic optimization is needed for the determination of the global optimum tool path for an objective concerning minimization of the cutting forces.

The problem is defined as passing over all the CL points determined on the 2D uniform grid of the part surface with the minimization of the cutting forces. As an example, for a 40x40x6 mm part surface (MATLAB’s peak function) tool path should be optimized for all CL points determined on a 2x2 mm mesh grid as shown in Figure 3.1.

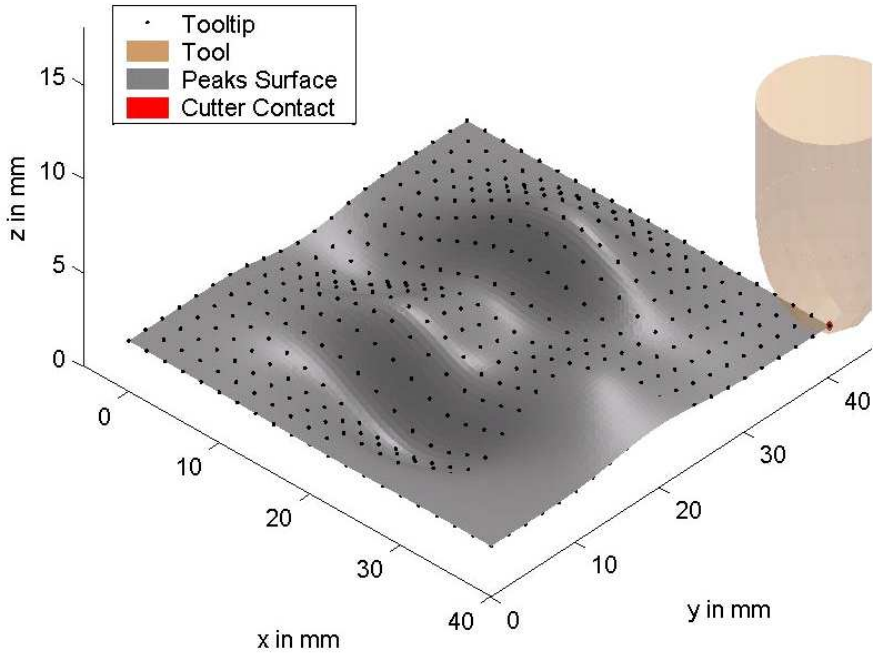

Figure 3.1. CL points on a 2x2 mm mesh grid for a 40x40x6 mm part surface

For the solution path to the problem, firstly CL points should be determined. A collision detection based algorithm is introduced to determine both the CL and cutter contact (CC) points with a user defined sensitivity (CC points is used for scallop height determination in multi-criteria optimization). Next step is the prediction of the slot cutting forces for each connection from CL points to its neighbors. Thanks to the predicted forces, force map is constructed which represents all possible movement with a specific reference force value. The last step is implementation of the static optimization algorithm to determine the optimum tool path to minimize the cutting forces. The solution path is demonstrated in the Figure 3.2.

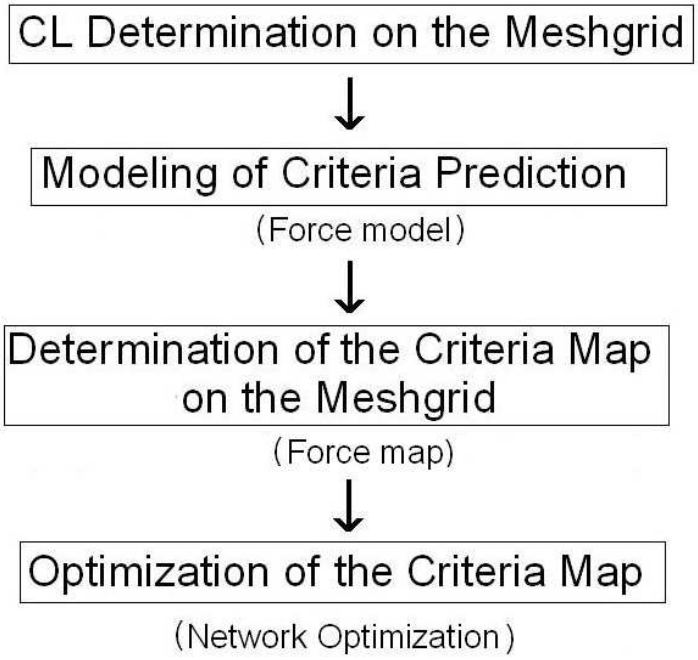

Figure 3.2 Solution path

3.2. Determination of the Cutter Location (CL) and Cutter Contact (CC) Points

Using M. Kochenderfer's collision detection library V-Collide, CL points and CC points are determined where the solid tool geometry is traveled through each 2D mesh grid point along the vertical axis. For demonstration, MATLAB's peak function is selected to create a sample for a free-form surface as shown in Figure 3.3. The 3D CAD model is obtained in Unigraphics NX 6 (UG NX 6). For the determination of the CL and CC points, the part surface obtained in UG NX6 is exported into MATLAB in STL format with 0.001 mm edge tolerance.

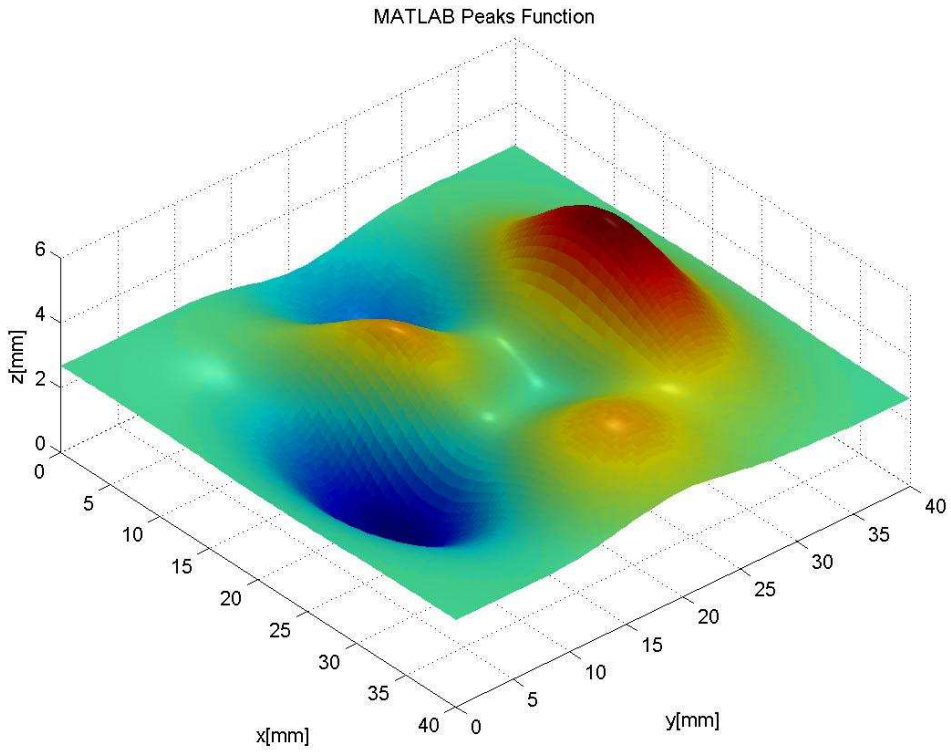

Figure 3.3 MATLAB peaks function

Then the part surface is scanned for a uniform XY via a collision detection algorithm grid with 2 mm step size to determine the CL and CC points. Further a finer grid of 1x1mm is also obtained for CC points in order to better represent the cut surface profile enclosed by four adjacent CL points. A screenshot of the scanning video in MATLAB are shown in the Figure 3.4 below, where the CL and CC points for a specific XY point is determined and represented in black and red points respectively.

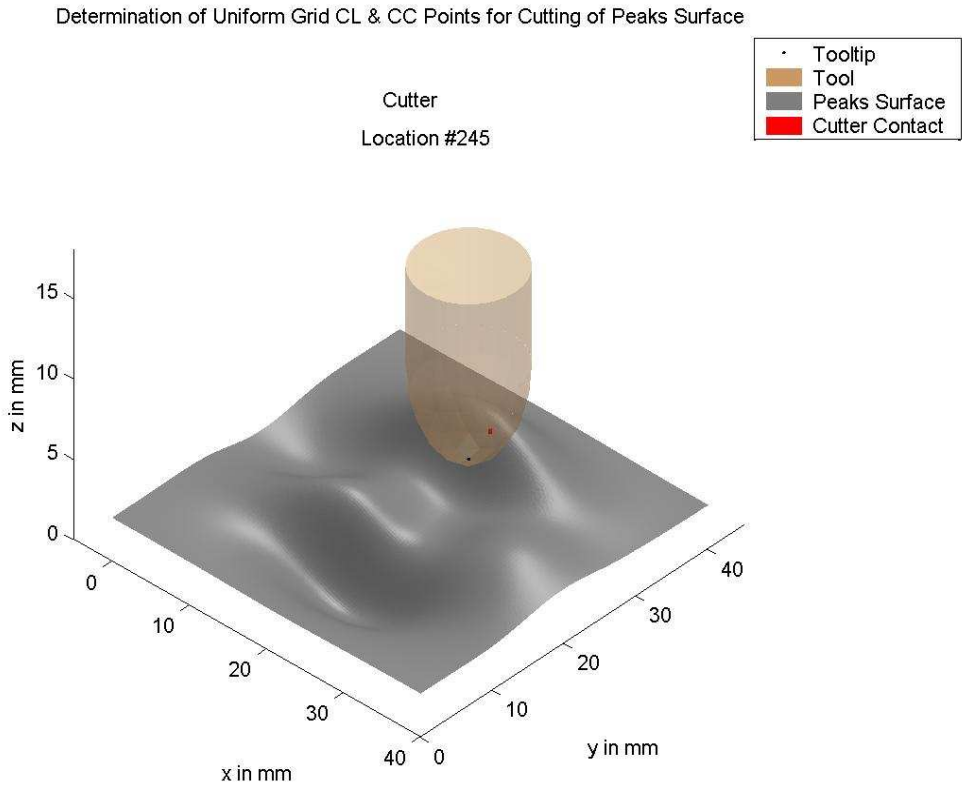

Figure 3.4 Collision detection

3.3. Modeling of Criteria Prediction

3.3.1. Mechanistic Cutting Force Model

Machining is a very complex and widely used process and large variety of milling tools are available and used in most of the industries, such as aerospace, automotive, home appliance and die-mold industries. Tool geometries are designed and optimized in order to maximize productivity and tool life while minimizing the cutting forces occurred during the operation. In the machining of free-form, non-monotonic sculpture surfaces, ball-end mill tools are used. Due to the complexity of cutting geometry of ball-end cutters, it is very difficult to model and predict the cutting forces. Prediction of cutting forces allows user to achieve high quality and faster machining without sacrificing from the tool life.

Cutting forces occurred during machining cause deflection on the ball-end cutter and result in considerable amount of surface error. Currently, the practices in industry, for each set of machining operations, conservative cutting conditions are used to overcome the deflection of the cutter. Conservative cutting conditions prevent

excessive tool deflection, however, productivity and the feasibility of the operation becomes low. The importance of modeling and precisely predicting the cutting forces in ball-end milling for very complex sculptured surfaces is that it can be used to calculate the cutter deflection and surface error and it can be used to increase the productivity by applying feedrate scheduling strategies.

In this section, an accurate and precise ball-end mill cutting force model with calibration developed by Kaymakci [35] is presented together with three modules: tool geometry, kinematics/chip load, and cutting force modules. The model is flexible so that it is valid for any kind of tool-workpiece combination, any type of cutting geometry, and cutting condition. This cutting force model is developed by Kaymakci [35] upon the previous studies of Guzel and Lazoglu [2] and Erdim et al. [3]; and also improved to cover the cylindrical sections of the ball-end mill and the calibration coefficients were determined for the cylindrical part of the tool [35].

End-mills can be characterized with many aspects, such as the macro geometry (helical-end, ball-end, bull-nose, flat-end, tapered, etc.), the micro geometry (helix, rake, clearance angles), the tool material (WC, PCD, HSS), the coating material (nanocomposite PVD, TiAlN, TiCN, etc.), the area of usage (rough, semi-finish, finish, super-finish milling), and the workpiece material (steel, aluminum, titanium, etc.). Detailed explanation of the micro-geometric properties of the end-mills as follows,

- Positive rake angle improves the shearing and cutting while decreasing the cutting forces. On the other hand, it weakens the cutting edge and makes it more vulnerable to wear and breakage.
- High helix angle smoothens and reduces the impact force during entry cutting and it help to remove away the chip.
- Clearance angle reduces the rubbing on the machined surface; therefore, it increases the surface quality. However, it weakens the cutting edge and more importantly, it increase the possibility of chatter vibrations by reducing process damping. A second clearance angle should be provided to reduce the amount of grinding during sharpening.

Helical end-mills have constant radius and helix angle along the depth of cut. Ball-end mills differ from flat end mills by their ball part such that their radius varies

along the ball-end. This varying radius r affects the cutting forces, because cutting speed changes with varying r. On the contrary, flat-end mills have constant cutting speed along the tool axis. The detailed geometry of a ball-end mill is shown in Figure 3.5. It can be observed that each flute lies on the surface of the hemisphere, and has a changing helix angle. Due to the decreasing radius towards the tip of the cutter, the local helix angle changes with varying cutting velocity for a discrete point along the cutting flute.

The equation of the geometry of the ball part is given by,

$$x^2 + y^2 + (R_b - z)^2 = {R_b}^2 \tag{3.1}$$

where x, y, and z are the coordinates of cutting edge ball-end mill according to the coordinate axes shown in Figure 3.5, and R_b is the ball radius measured from the center of the sphere. The cutter radius is zero at the tip and at axial location z, in plane x-y,

$$r^2 = x^2 + y^2 \tag{3.2}$$

The ball-mill cutter used in calibration and validation tests was 12 mm diameter, two fluted ball-end mill from CoroMill series of Sandvik. Cutting edge geometry was taken from Erdim [2]. The author measured the cutting edge with a Coordinate Measuring Machine (CMM). Obtained data points were used to obtain following third degree polynomial that represents the cutting edge geometry for the cutting force model.

$$\beta = 0.0036 \times r^3 - 0.0205 \times r^2 + 0.0547 \times r - 0.041 \tag{3.3}$$

r [mm] is the radius of an arbitrary point on the cutting edge perpendicular to the cutter axis, and β [deg] is the lag angle between the line which connects this arbitrary point to the tip and the line tangent to the cutting edge at the tip. Details of

the cutting edge geometry can be seen in Figure 3.6. The cutting geometry can be represented in the cutter coordinate system as the following;

$$x_c = r \times \cos(\beta), \quad y_c = r \times \sin(\beta), \quad z_c = R_b - \sqrt{R_b^2 - r^2} \tag{3.4}$$

As a result, it is possible to determine cutting edge profile by varying radius (*r*).

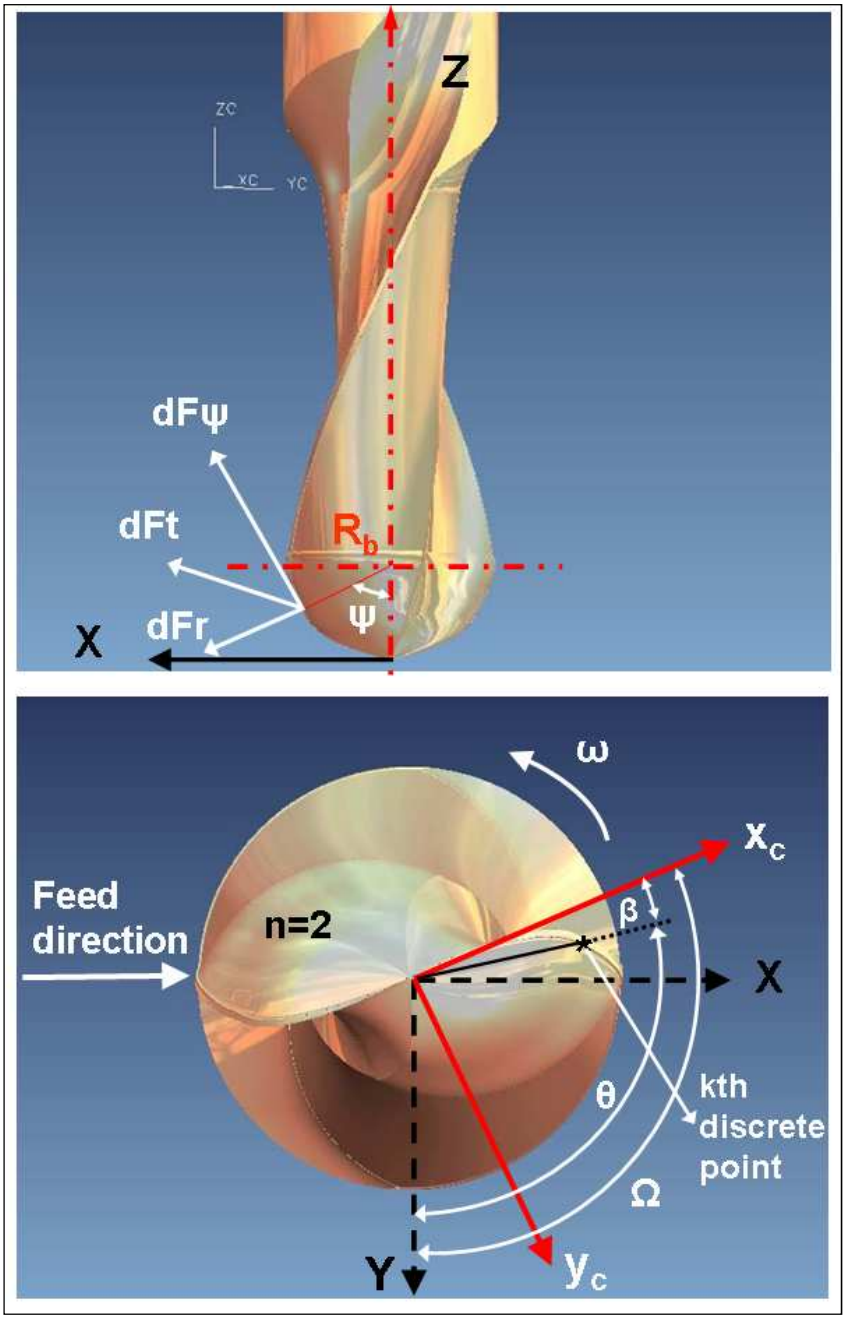

Figure 3.5 Illustration of cutting force vectors and angular relationships from Kaymakci [35]

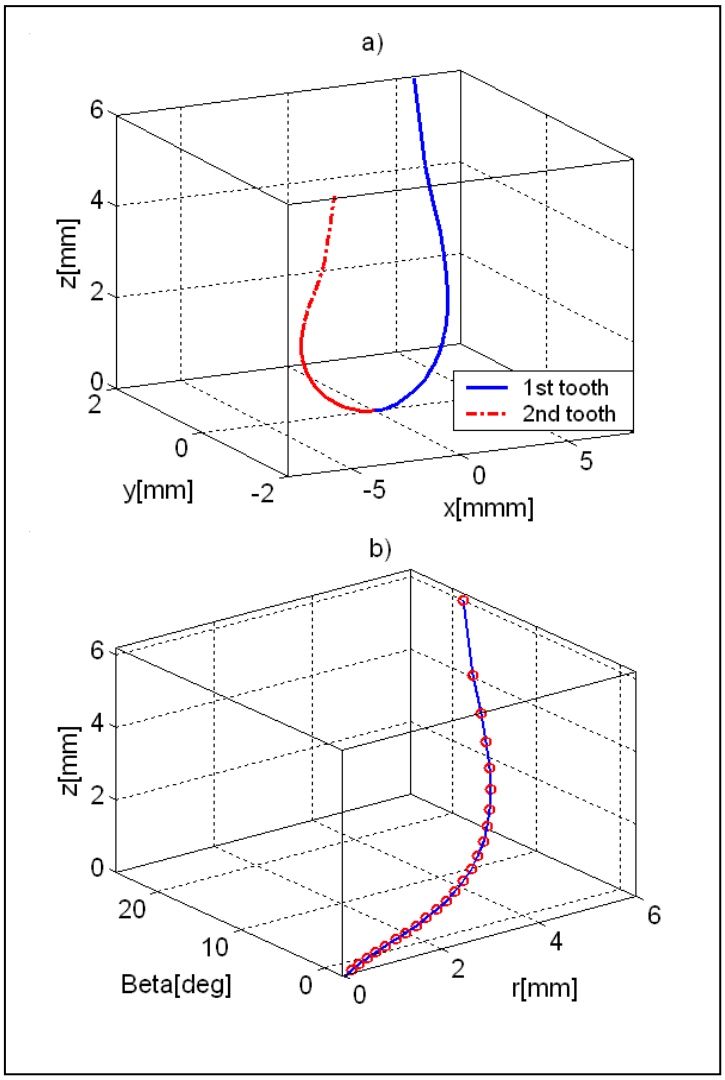

Figure 3.6 Cutter geometry: a) Cutting edges, b) Third degree polynomial fitting for $\beta(r)$.

Since cutting forces are directly related to the instantaneous undeformed chip thickness, uncut chip thickness should be precisely calculated to improve the performance of the cutting force model.

It is possible to understand the chip load of ball-end milling process by examining the early analysis of Martelotti [5]. Martelotti stated that due to the combined rotational and linear motion of the cutter towards the workpiece, the true path of the cutter is an arc of a trochoid, rather than a circle. However, in most practical conditions where feed per tooth is much smaller than the cutter radius; circular tool path assumption is valid, because the error is negligible. The chip formation geometry is shown in Figure 3.7. Chip formation on a flat-end mill is shown as;

$$t_c = t_x \times \sin(\theta) \tag{3.5}$$

where t_c is the instantaneous chip load, t_x is the feed per tooth and θ is the immersion angle of cutting point. This equation is valid for flat-end mills which have only rotational and linear straight motion. However, in order to accurately model instantaneous chip load for ball-end mills, non-horizontal feed motion and spherical part of the ball-mill should be considered.

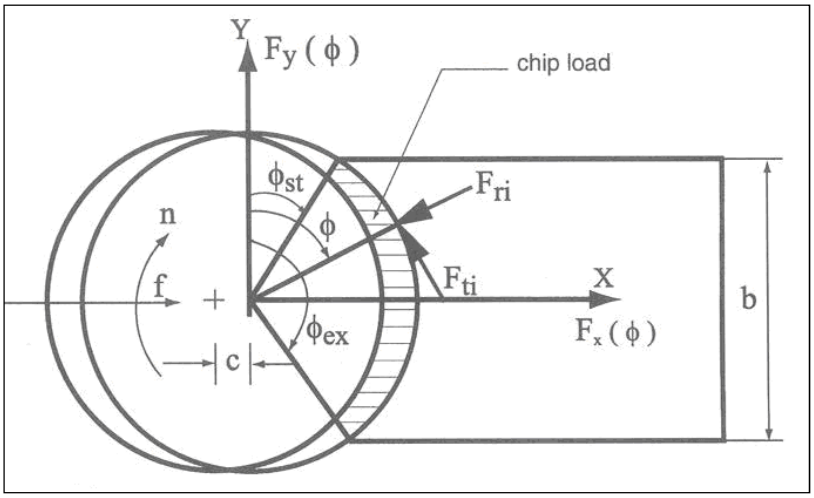

Figure 3.7 Geometry of chip formation in end milling from Altintas [36].

Figure 3.8 represents chip formation in non-horizontal tool motion. During non-horizontal motion, feed (f) can be divided into two components: f_h is the horizontal feed component and f_v is the vertical feed component. When the tool moves with an inclination angle, feed direction is not perpendicular to the tool axis, which results in a different undeformed chip geometry.

If the situation is downward ramping, in order to calculate the uncut chip thickness, due to the drilling effect, following term should be added to chip thickness formula. On the other hand, in upward ramping, this term should be subtracted.

$$\Delta t = t_x \times \cos(\psi) \times \sin(\alpha) \tag{3.6}$$

Modifying the instantaneous chip thickness formulation for non-horizontal motion results in;

$$(t_c)_{kn_{new}} = t_x \times \sin(\theta) \times \sin(\psi) \times \cos(\alpha) \pm t_x \times \cos(\psi) \times \sin(\alpha) \tag{3.7}$$

where $(t_c)_{kn_{new}}$ is the modified ball-end mill instantaneous chip load, t_x is feed per tooth, θ is the immersion angle of cutting point, ψ is the cutting element position angle and α is the feed inclination angle. Feed inclination angle (α) should be between 0° and 90°.

Following chip thickness formation determination, the infinitesimal chip load for each cutting disk which is in contact can be expressed as;

$$dA_c = (t_c)_{kn_{new}} \times (dz)_{kn} \tag{3.8}$$

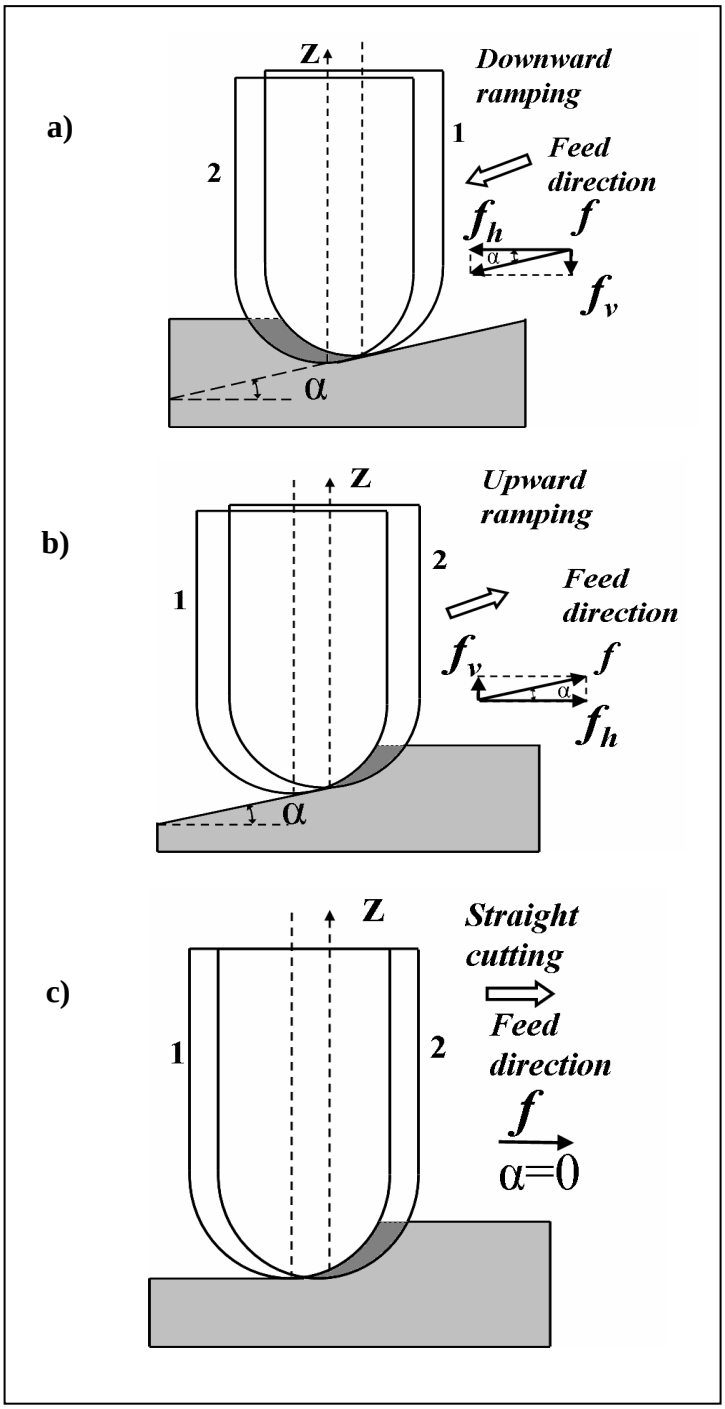

Figure 3.8 a) Downward ramping, b) Upward ramping, c) Straight cutting from Kaymakci [35]

Guzel and Lazoglu [2] stated that for a differential chip load (dA_c) in engagement domain, the differential radial (dF_r), differential zenith (dF_ψ), and differential tangential (dF_t) cutting forces can be expressed as,

$$dF_r = K_{rc} \times dA_c + K_{re} \times dz \tag{3.9}$$

$$dF_{\psi} = K_{\psi c} \times dA_c + K_{\psi e} \times dz$$

$$dF_t = K_{tc} \times dA_c + K_{te} \times dz$$

where K_{rc}, $K_{\psi c}$, and K_{tc} are the radial, zenith, and tangential cutting coefficients and K_{re}, $K_{\psi e}$, and K_{te} are the related edge coefficients respectively. These specific cutting coefficients depend on tool-workpiece combination. These parameters were determined with calibration tests. These calibration tests were performed with 12 mm diameter Sandvik CoroMill series ball-end mill with a helix angle of 25° and an Al7039 workpiece material. Erdim [3] determined cutting coefficients for the same tool-material combination only for spherical part of the tool, thus calibration coefficients for spherical part of the ball-end mill were taken from this research. In Erdim's research, tool has been divided into 7 disks along the tool axis in the spherical part and cutting constants were evaluated for each region separately by performing incremental slot cutting tests with different feedrate values. Details of the calibration process will be explained at the end of this chapter. Once the differential radial (dF_r), differential zenith (dF_ψ), and differential tangential (dF_t) cutting forces were evaluated through the use of Equation 3.9, these cutting force components can be transformed into the global X-Y-Z coordinate system with the following equations;

$$\begin{bmatrix} dF_X \\ dF_Y \\ dF_Z \end{bmatrix} \Bigg|_{k,n} = A \times \begin{bmatrix} dF_r \\ dF_\psi \\ dF_t \end{bmatrix} \Bigg|_{k,n} \tag{3.10}$$

$$A = \begin{bmatrix} -\sin(\psi) \times \sin(\theta) & -\cos(\psi) \times \sin(\theta) & -\cos(\theta) \\ \sin(\psi) \times \cos(\theta) & \cos(\psi)\cos(\theta) & -\sin(\theta) \\ \cos(\psi) & -\sin(\psi) & 0 \end{bmatrix} \Bigg|_{k,n} \tag{3.11}$$

$$\theta = \Omega + \frac{(n-1) \times 2\pi}{N_f} - \beta_k; \;\; n = 1 \ldots N_f \tag{3.12}$$

where θ is the immersion angle for flute n, K represents the total number of discrete points on a cutting edge, ψ is the cutting element position angle, Ω is the cutting edge rotation angle, N_f is the tooth number and β is the lag angle evaluated from Equation 3.3.

$$\begin{bmatrix} F_X \\ F_Y \\ F_Z \end{bmatrix} = \sum_{n=1}^{N_f} \sum_{k=1}^{K} \begin{bmatrix} dF_X \\ dF_Y \\ dF_Z \end{bmatrix} \Bigg|_{k,n} \tag{3.13}$$

Next step is to be taken after prediction of cutting forces is to validate these predictions by performing validation tests. Validation tests and their results are shown in next chapter. The proposed cutting force model is summarized in Figure 3.9. Finally, a pseudo code of the force model is presented in Figure 3.10.

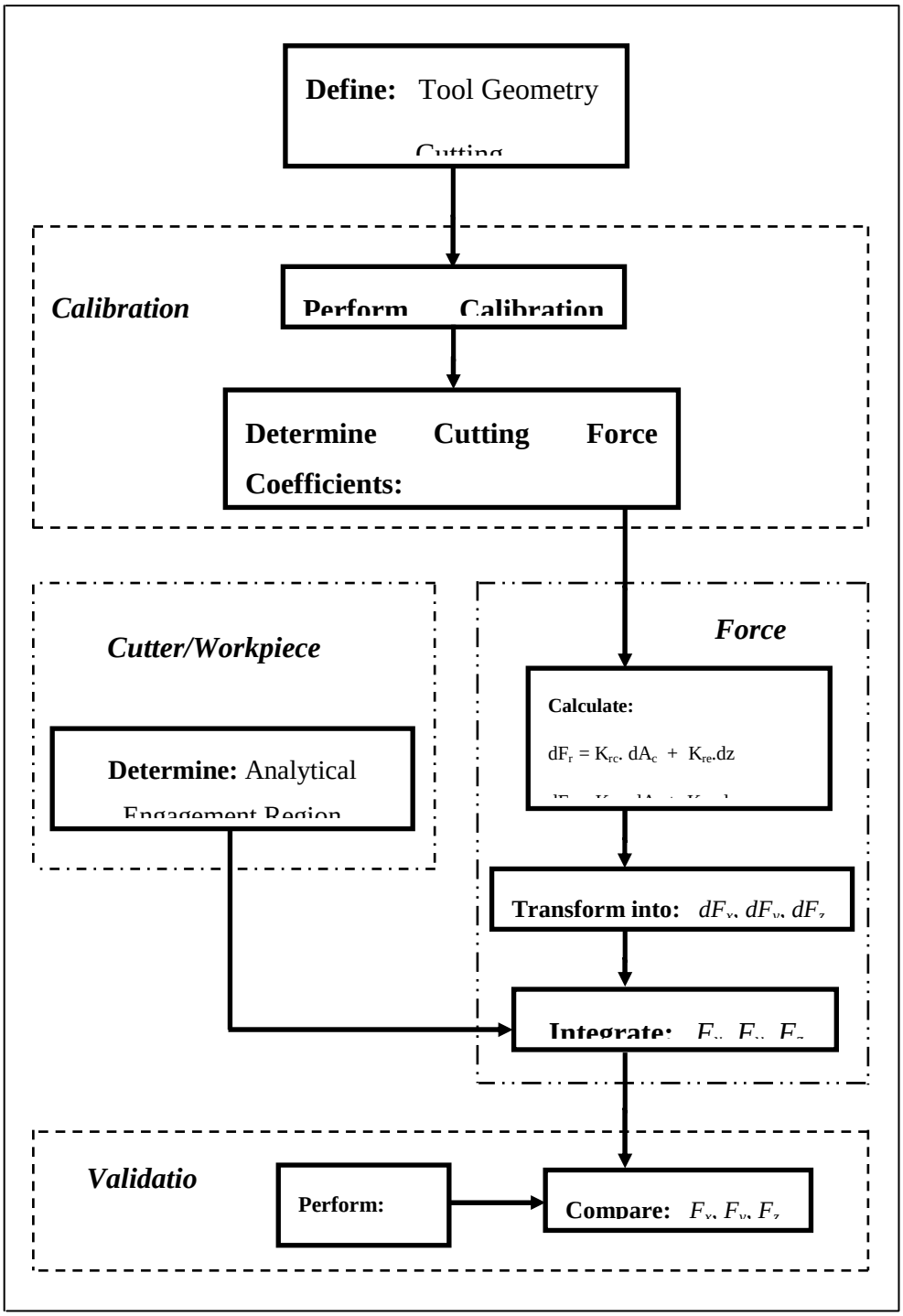

Figure 3.9: Summary of the proposed mechanistic approach.

Inputs:

Cutting conditions : w (spindle speed), f (feedrate)

Tool geometry : D (diameter), β (lag angle), Nf (number of flutes)

Integration angle : dθ

Integration height : dz

Tool path G code : CL (number of G codes)

Outputs:

Cutting force history : Fx, Fy, Fz, Fres

Variables:

$K = \frac{D}{2 \cdot dz}$: Number of axial integration steps

$M = \frac{2\pi}{d\theta}$: Number of angular integration steps

j= 1 to CL : Integrate along the tool path (**1st loop**)

i=1 to M : Angular integration loop (**2nd loop**)

p=1 to Nf : Calculate the force contributions of all teeth (**3rd loop**)

$\theta_1 = i \cdot d\theta + \frac{(p-1) \cdot 2\pi}{Nf}$: Immersion angle for tooth p

k=1 to K : Integrate along the axial depth of cut (**4th loop**)

$z(k) = k \cdot dz$: Axial position

$r = \sqrt{\left(\frac{D}{2}\right)^2 - \left(\frac{D}{2} - z(k)\right)^2}$: Cutting radius

$\psi = a\sin(\frac{2 \cdot r}{D})$: Cutting element position angle

$\theta_2 = \theta_1 - \beta(r)$: Updated immersion angle due helix angle

if $\theta st < \theta_2 < \theta ex$: θst: entry angle of contact, θex: exit angle of contact (**if**)

$$tc_{kn} = \left(\frac{f}{Nf \cdot w}\right) \cdot \sin(\theta_2) \cdot \sin(\psi) \cdot \cos(\alpha) - \left(\frac{f}{Nf \cdot w}\right) \cdot \cos(\psi) \cdot \sin(\alpha)$$

: Chip thickness (α: inclination angle found for CL point

$dAc = tc_{kn} \cdot dz$: Differential chip load

$dF_r = dAc \cdot K_{rc} + dz \cdot K_{re}$
$dF_t = dAc \cdot K_{tc} + dz \cdot K_{te}$: Differential force
$dF_\psi = dAc \cdot K_{\psi c} + dz \cdot K_{\psi e}$

$dFx, dFy, dFz = A \cdot \lfloor dF_r, dF_t, dF_\psi \rfloor$

: In orthogonal directions, A (transformation matrix)

$Fx(i) = Fx(i) + dFx$
$Fy(i) = Fy(i) + dFy$: Sum the cutting forces
$Fz(i) = Fz(i) + dFz$

End (1st loop)

End (2nd loop)

End (3rd loop)

End (4th loop)

Figure 3.10: Pseudo code of cutting force model.

3.3.1.1. Calibration Process:

Cutting force coefficients are contributed by shearing action in radial, zenith, and tangential directions. They are assumed to be constant for tool-workpiece material pair, and can be evaluated either mechanistically or using classical oblique cutting transformations. Although orthogonal calibration is desired, it requires turning tests; therefore mechanistic calibration was used. So in this study, cutting coefficients determined by Kaymakci [35] are used where he was preferred used mechanistic calibration approach. In order to determine the cutting coefficient, Altintas' [36] approach for identification of cutting coefficients in milling has been utilized with certain changes.

First step in the calibration process to determine cutting coefficients is to obtain the cutting forces by conducting a set of milling experiments at different feedrate values. The spherical part of the ball-end mill has been divided into separate disks for detailed analysis. Erdim's [3] study of calibration for the spherical part of the tool was implemented. Full immersion slot cutting tests were implemented and the average cutting forces can be expressed as a linear function of feedrate and an offset contributed by the edge forces.

All cutting forces at different depth of cuts for 192 mm/min can be seen in Figure 3.11. In order to determine the calibration coefficients for a certain disk following procedure has been applied by Kaymakci [35]:

1. Using the inverse transformation of the transformation matrix *A* given in Equation 3.11, collected force components which are in X-Y-Z global coordinate system have been transformed into radial, zenith and tangential force components F_r, F_ψ, and F_t respectively.
2. Maximum values of each tooth for all three components (r-ψ-t) of the cutting force have been found, and the averages of these peak points are taken for certain number of the revolutions in the collected data.
3. The differences between the average points have been obtained for each increment in the depth of cut (e.g., for 4-6 mm interval, cutting forces will equal the difference between 6 mm depth of cut and 4 mm depth of cut cutting forces).
4. Finally, once the Fr, Fψ, and Ft values have been obtained for each depth of cut interval, these values have been plotted versus chip thickness in order to obtain the cutting coefficients. Illustration of this procedure is shown in Figure 3.12.

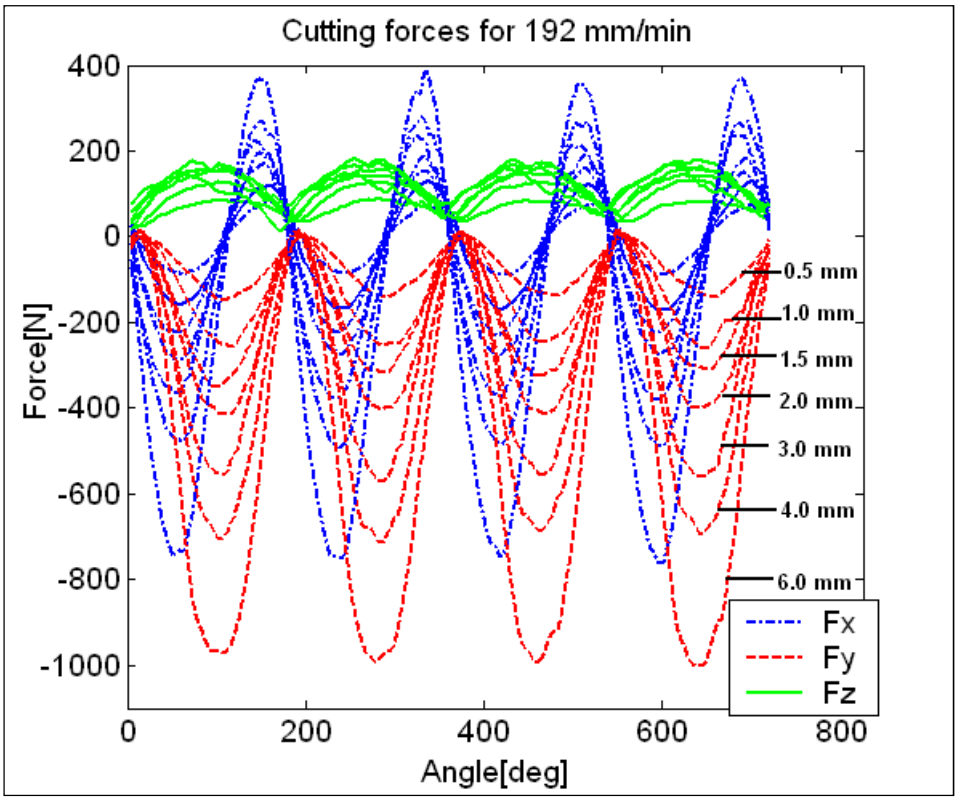

Figure 3.11: Cutting forces with different depth of cuts at f = 192 mm/min from Erdim [2].

Besides spherical part, since ball-end mills have cutter flute on the cylindrical part of the tool, cutting coefficients for the cylindrical part also should be determined. The same procedure applied for the cylindrical part, and since this part is identical along the tool axis, it is not necessary to divide the cylindrical part of the tool into disks. Radial, zenith and tangential forces versus chip thickness plot for cylindrical part of the tool is shown in Figure 3.13. The numerical values of the cutting coefficients determined with the calibration process can be summarized in Table 1. It is observed that Ktc is the most dominant cutting coefficient. The edge coefficients, on the other hand, exhibit an almost completely random behavior; no trend can be clearly identified by observing their behavior with different depth of cuts.

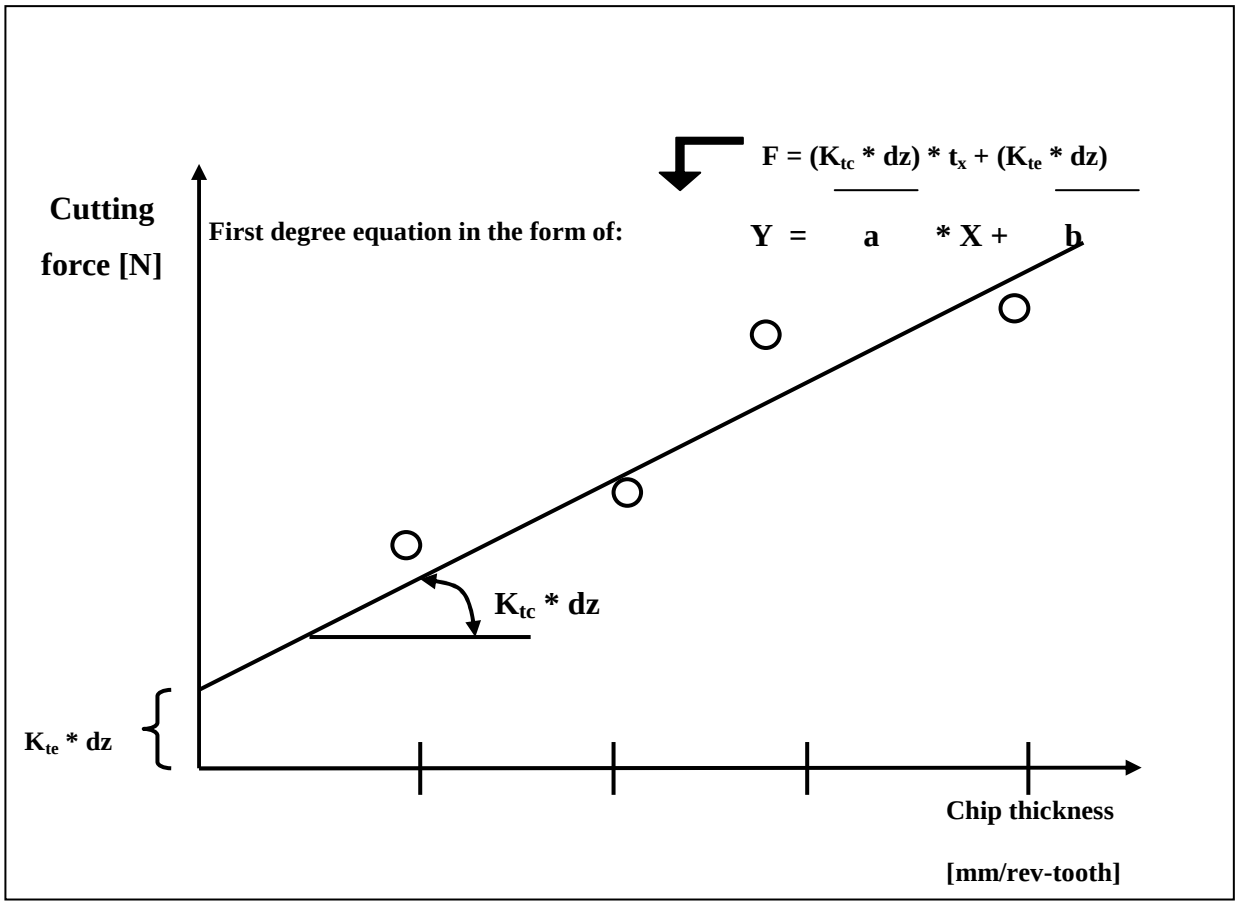

Figure 3.12: Determination of calibration coefficients from calibration experiments.

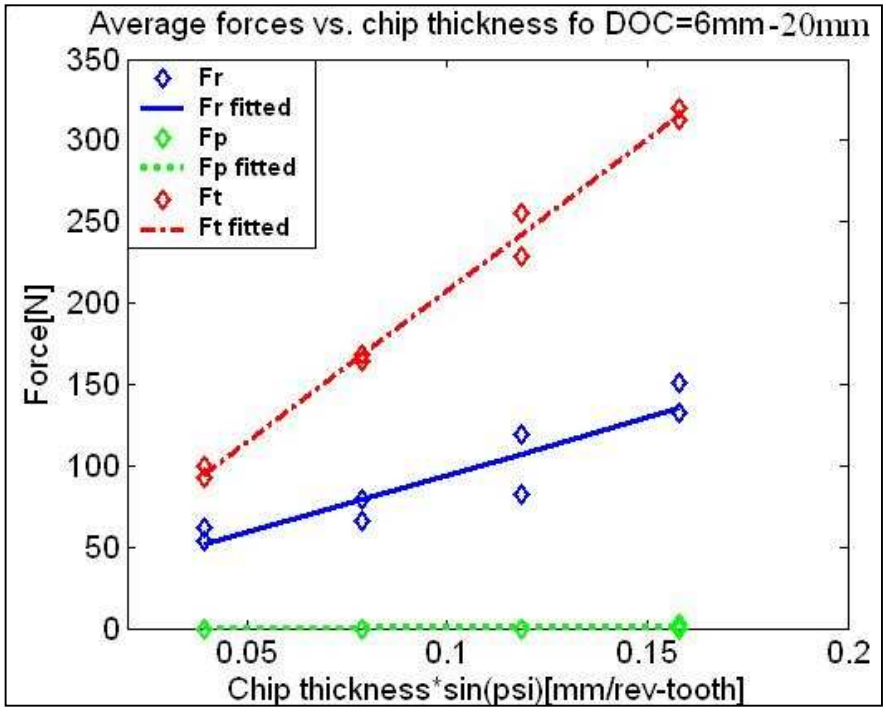

Figure 3.13: Cutting forces vs. chip thickness for 6-20 mm.

Table 3.1 Numerical values of cutting and edge coefficients for different intervals from tip.

Interval from tip / **Coefficients**	**0 - 0.5 [mm]**	**0.5 -1 [mm]**	**1 - 1.5 [mm]**	**1.5 -2 [mm]**	**2 – 3 [mm]**	**3–4 [mm]**	**4 – 6 [mm]**	**6 – 20 [mm]**
K_{rc} [N/mm^2]	2991	695	22	196	105	483	353	268
K_{re} [N/mm]	31	10	9	2	7	15	12	3
$K_{\psi c}$ [N/mm^2]	1113	785	753	179	101	31	6	249
$K_{\psi e}$ [N/mm]	12	13	4	19	14	9	0	3
K_{tc} [N/mm^2]	5354	2549	1182	1429	971	848	932	829
K_{te} [N/mm]	37	17	30	3	16	17	11	12

3.3.2. Solid Model Based Engagement Model

Determining the tool-workpiece engagement is very critical, since it is directly related to the chip load and cutting forces. The aim of the tool-workpiece engagement domain determination model is to obtain which sections of the tool is engaged with the workpiece at any instant of machining process. Moreover, in order to produce parts with complex free-form surfaces in an optimum manner in terms of cycle time, cost and product quality, engagement model needs to be calculated fast and accurately. Therefore, for precise simulation of free-form surface machining, the most important parameter is the accurate determination of the instantaneous chip loads along the tool path.

In this section, solid based approach used to determine the tool-workpiece engagement region for 3D complex sculptured free-form surfaces with ball-end milling. Since other engagement domain calculation approaches (analytical, discretization, Boolean) do not cover non-monotonic surfaces or they are computationally expensive and slow, solid based engagement can be used for every kind of surface and is comparably faster and quite accurate than any other approaches. The solid based engagement model used in this study is developed in Moduleworks GmbH in Germany. Details of the solid based engagement model are presented in Kaymakci et al. [1]. In the process of tool-workpiece engagement model along the tool path, the output (CL file) of any commercial CAM package is post processed by this solid based engagement algorithm.

In the machining of free-form surfaces, axial depth of cut is not constant throughout the tool path. Consequently, engagement region changes at each CL point. Figure 3.14 shows a sample CL output of Unigraphics NX4 CAM module output. Each line represents a CL point. Red sections show the position of the tip of the ball-end mill according to the surface's coordinate system and blue sections show the orientation unit vector of the tool. For three-axis machining, orientation of the tool is constant and equals to (0, 0, 1).ı

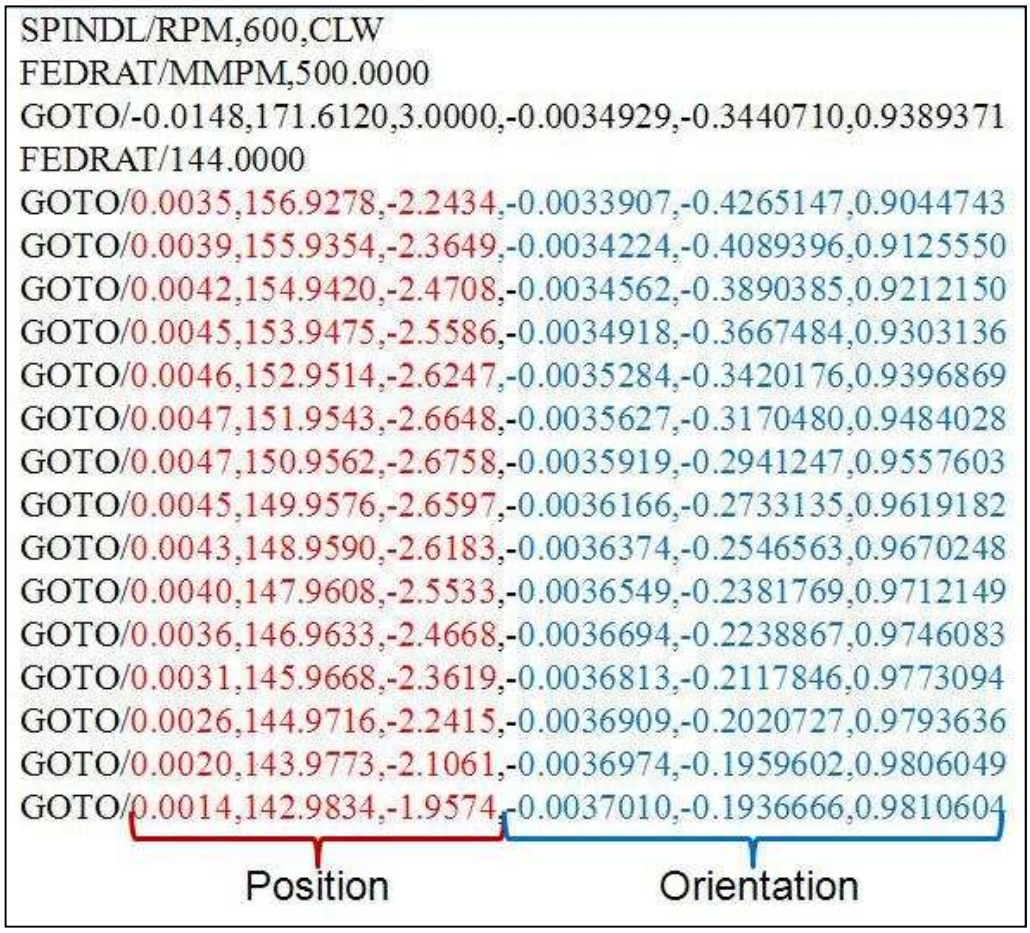

Figure 3.14 An example of a CL-file.

Using a tool-workpiece engagement model, the engagement between tool and workpiece can be calculated at any time of the machining within a controllable accuracy. The initial workpiece definition (stock), geometric definition of tool(s) and the motion of the tool in the workpiece coordinate system must be present to achieve this goal. Another important property of this approach is that engagement can be calculated for any type of tool if the geometric properties of tool (diameter, length, taper angle, flute length etc.) and tool holder (tool offset, diameter, length, taper angle, corner radius etc.) are present. Furthermore, a significant advantage of this model is that any arbitrary shaped model can be used as an initial stock, instead of a rectangular block

An axis-aligned 3 dimensional uniform grid of points is used to describe the initial workpiece prior to machining (Figure 3.15). The density of the grid is controlled through the grid distance which is identical along X, Y, and Z directions. In this study, grid distance which defines the resolution the tool and workpiece was selected as 0.0625 mm. A solid triangulated mesh defines an arbitrary shaped initial

workpiece prior to machining. In order to initialize the grid points with this given mesh, all points inside the solid mesh are marked with collision time $t = \infty$. Outside points are marked with the collision time of $t = -1$. $t = -1$ points are the grid points on the bounding box which covers the workpiece; however they are not in the mesh defined by the workpiece.

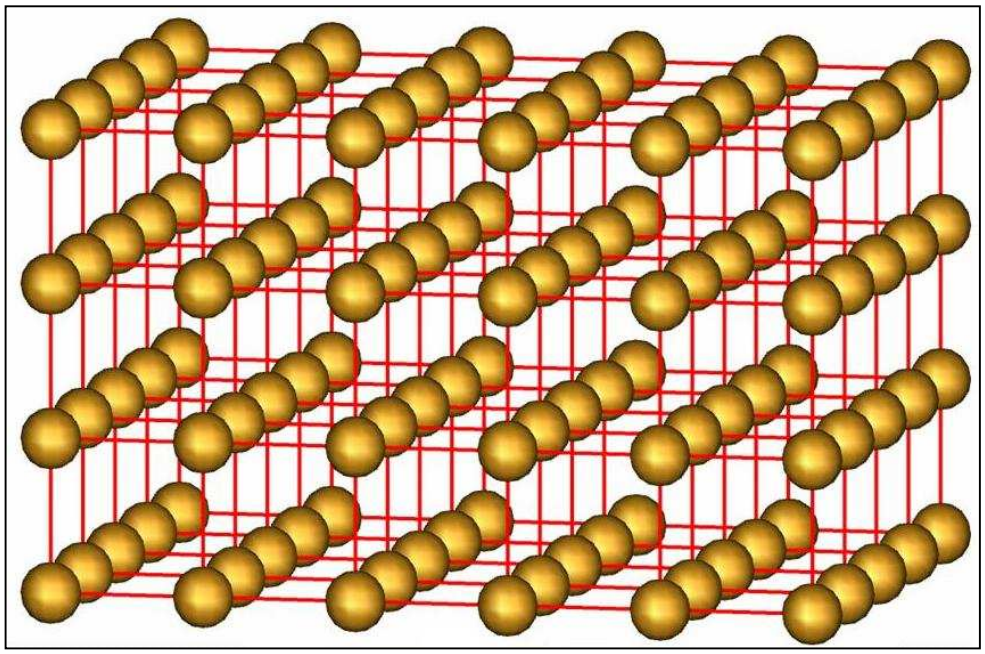

Figure 3.15: 3D grid of points used to describe the initial workpiece.

The motion of the tool path is presented through the tip point of tool in space and the orientation vector of tool axis as a function of t allowing 3, 4 or 5 axis tool paths to be used as input. Further a collision determination method has been implement that delivers the time of first contact between the moving tool which consists of translation and rotation both and a grid point in space (Figure 3.16). For each time slice Δt, the motion of tool from t to $t + \Delta t$ is passed to the collision determination method together with all the points in the local region that might be hit by this sweep motion. Each grid point that has been hit by the tool motion is being marked by the time value of the collision and in the next time interval this grid point does not need to be re-checked for collision since it has been already hit in the past. Further, all the grid points that have been hit within the same time interval are referenced in a list dedicated to this time interval.

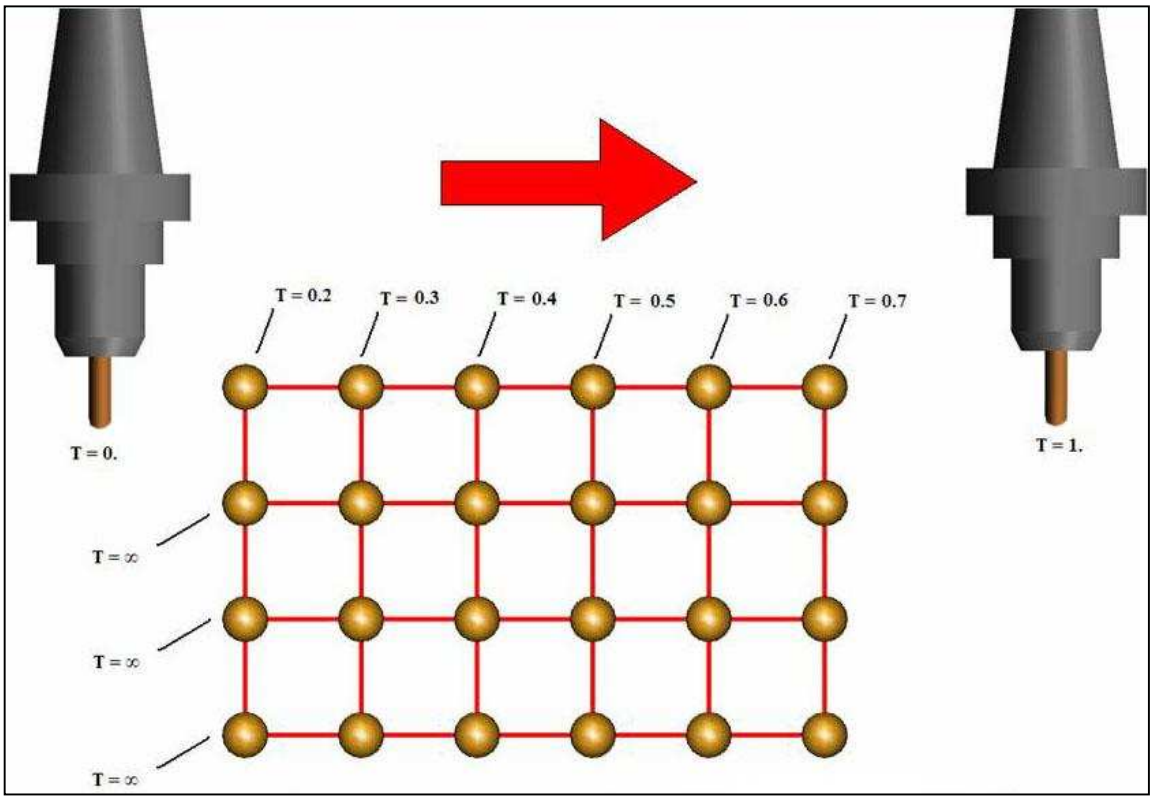

Figure 3.16: Grid cells and their collision time attribute T.

The engagement between tool and workpiece can be calculated for each time interval by analyzing the list of grid points for this time interval from the perspective of a stationary tool. This is done by transforming the mentioned grid points to the coordinate system of stationary tool. Then the tool is sliced along the tool axis to slices with constant thickness. In this study, constant thickness (Δh) is selected as 0.1 mm. As the sliced tool length increases, the computation time increases, thus sliced tool length was determined according to the maximum depth of cut of the machining process. Each slice is between h and $h + \Delta h$ where h is the height of slice from the tool tip point. The grid points are distributed to slices and for each slice the signed minimum and maximum distances from the tool axis in the view defined by the tool motion direction is calculated using all grid points belonging to this slice. Doing this for each slice delivers the engagement for each slice (Figure 3.17).

After all the time intervals are processed, the 3D grid points are marked with different t values. All remaining grid points with the $t = \infty$ describe the remaining stock after the machining and could be used for a coarse visualization using various iso-surface extraction methods at the given level where the level of extraction is the desired time value t. Interesting is that the visualization is also possible for any given

t value since each grid point “knows” when it has been hit by the tool. This opens an interesting perspective for rest-material determination at any stage of machining since the “history” of machining is stored in the 3D grid model.

The above described solid model has been implemented and used for the following cutting force calculation. The run time behavior of the tool-workpiece engagement model is $O(n^3)$ due to three dimensional grid. Computation time of the model for 50x50x6 mm. solid body with 0.0625 mm. grid distance resolution on Pentium 4 2.66 GHz with 2 GB of RAM is approximately 4 hours and 20 minutes.

The accuracy can be controlled through the grid distance, time step value Δt and the tool slicing step value Δh. The output of the solid based engagement model is shown in Table 3.2. In Table 3.2, the engagement is displayed as the minimum and the maximum distances from the tool axis for each discrete disk and that disk’s CL number. In force model, these distances were converted into φ_{st} and φ_{ex} entrance and exit angles respectively. Illustrations of these angles are shown in Figure 3.18. As stated before, it is impossible to calculate the engagement domain for non-monotonic sculptured surfaces using analytical methods. In sculptured surface machining, the engagement between tool and the workpiece is very complex and variable. Variation of engagement domain for different CL points is presented in Figure 3.19 and Figure 3.20.

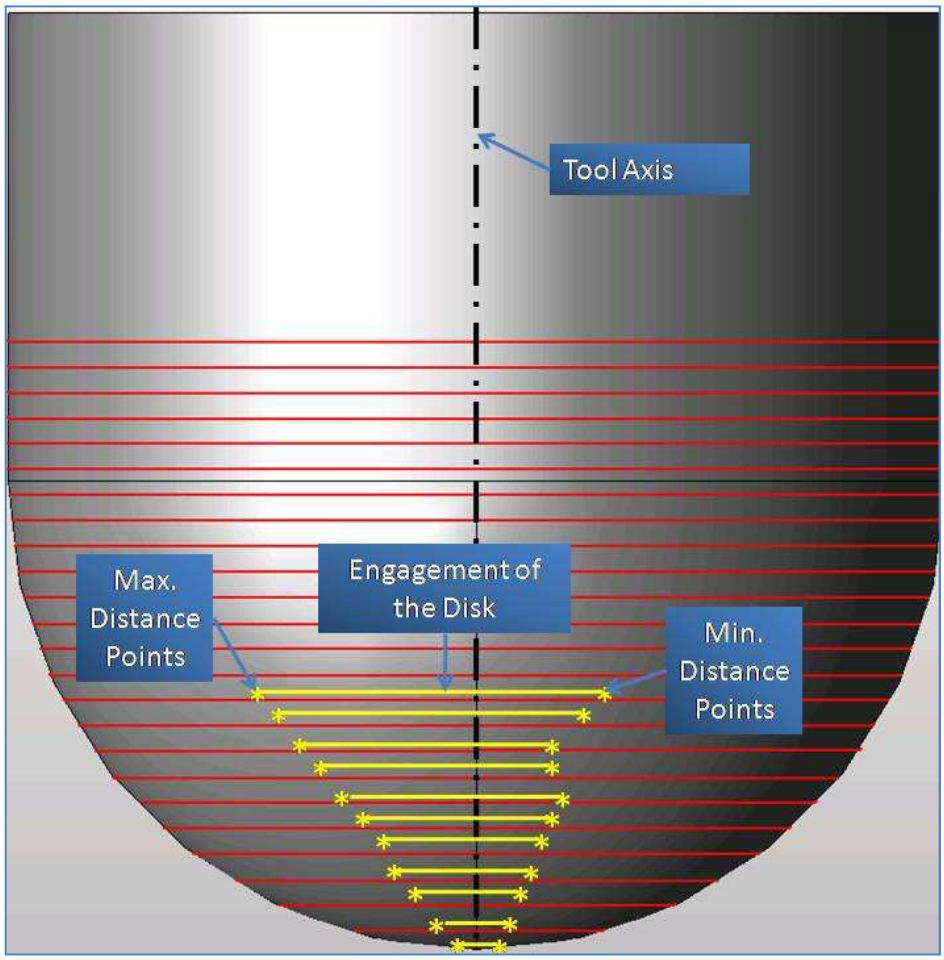

Figure 3.17: Determination of the min. and the max. distance from tool axis for each slice.

Table 3.2 Sample text output of the engagement model.

CL #	Start - End Distances of the Disks from the Tip of the Tool [mm]		Min Width [mm]	Max Width [mm]
19	4	4.1	0.75	5.6875
19	4.1	4.2	1.1875	5.6875
19	4.2	4.3	1.3125	5.75
19	4.3	4.4	1.625	5.75
19	4.4	4.5	1.8125	5.75
19	4.5	4.6	1.9375	5.8125
19	4.6	4.7	2.125	5.8125
19	4.7	4.8	2.25	5.875
19	4.8	4.9	2.3125	5.875
19	4.9	5	2.4375	5.875
19	5	5.1	2.5625	5.8125
19	5.1	5.2	2.625	5.75
19	5.2	5.3	2.75	5.6875
19	5.3	5.4	2.8125	5.625
19	5.4	5.5	2.875	5.4375
19	5.5	5.6	2.9375	5.3125
19	5.6	5.7	3	5.125
19	5.7	5.8	3.0625	4.875
19	5.8	5.9	0	0
19	5.9	6	0	0

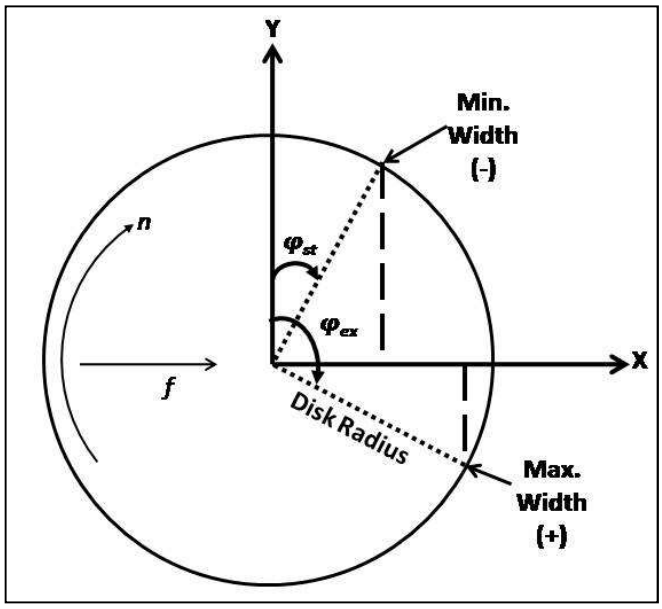

Figure 3.18: Illustration of start and exit angles.

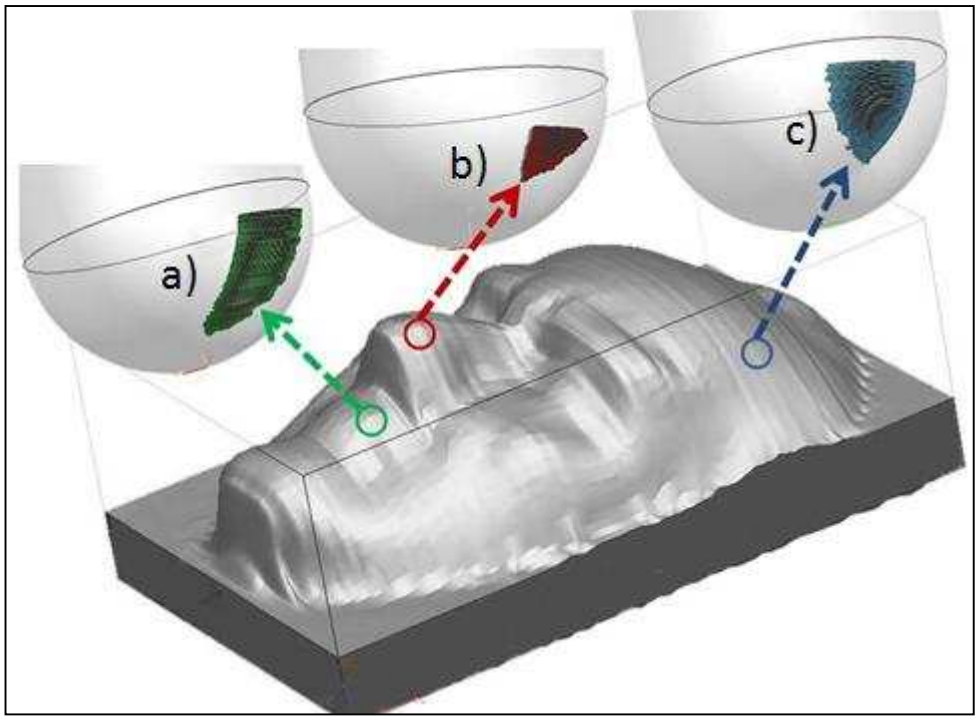

Figure 3.19: Variation of engagement domains along the tool path.

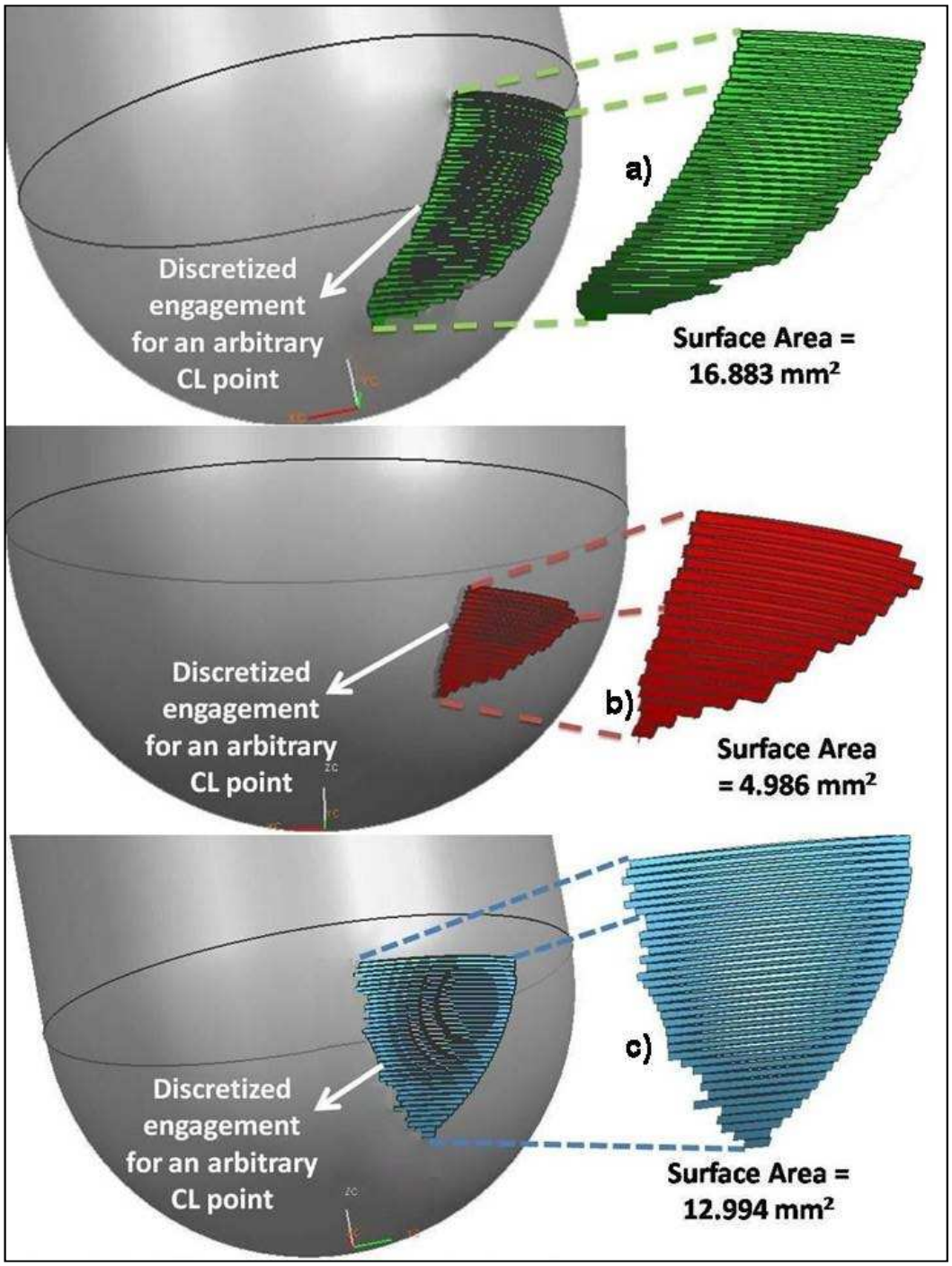

Figure 3.20 Illustration of engagement regions at a), b), and c).

3.4. Determination of the Criteria Map on the Grid Mesh: Force Map Formation

In order to determine a reference value for the cutting forces in each direction for all CL points referring a uniform Cartesian mesh, a force map is constructed showing reference values for all possible cutting forces from each CL point to its neighbors. This reference map is obtained by pre-computation combining engagement and force simulations of slot cutting operations in each direction.

For demonstration, Sine-Cosine surface is selected. On the 3D surface shown in Figure 3.21, 441 CL points are determined with grid size at x = y = 2 mm for a uniform mesh. Force Map is obtained by total of 3280 slot cutting simulations with ball-end mill with diameter of 12 mm each for one connection of the CL points, and shows the inversely proportional weight of the force magnitudes for each CL point in all of the 8 directions relatively to each other where large magnitudes are depicted with short lines and small magnitudes with longer lines. Figure 3.21 and 3.22 depicts the zig path directions and formed force map. The grid size of the engagement tool is z = 62.5 μ, x = y = 312.5 μ, where the engagement of the cutting tool with the workpiece is determined during the whole cutting process.

Figure 3.21 Solid model of the sin-cos surface

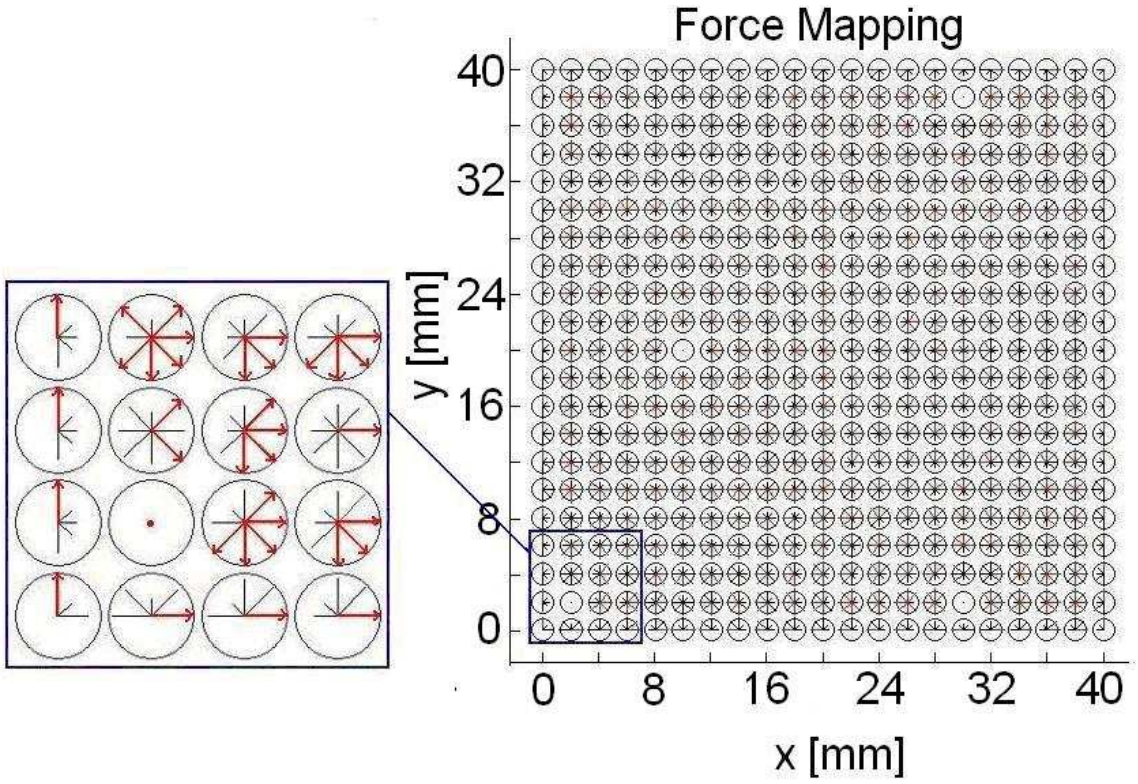

Figure 3.22 Force map

3.5. Optimization of the Criteria Map: Network Optimization

For the optimization process, the objective is minimizing the mean value of cutting forces and limiting the force below a threshold. The problem could be redefined as passing over all the vertices on the graph with minimum cost of weights for a given directed graph (force map) on the set of edges and vertices with weight function assigning a nonnegative real weight (forces) to every edge of the graph. In that sense, the solution for such a problem is known as network optimization.

For a given force map with n x m nodes where each node have a particular force value towards its neighbors, there are possible optimization routines such as 'Minimum Spanning Tree' (MST) and 'Minimum Cost Traveling Salesman' (MCTS) with their objectives as formation of a single minimum cost tree and a minimum cost single path respectively. In that sense, MCTS costs higher since its objective has less freedom of movement and causes possible inclusion of high cost connections to the path. On the other hand, MST's freedom could be only increased by the abandonment of the objective of obtaining single tree.

In the first part of the optimization process, 'Minimum Cost Connections' (MCC) are obtained for the given map where minimum cost target moves from each node are separately collected. Since these connections are separately collected, it may cause disunity and may form more than one tree resulting from possible loops including also two node loops such as connections from i to j and j to i. Each loop creates one disconnection and increases number of discrete trees MCC contained. Prim's algorithm for obtaining MST guarantees that a tree can be transformed to a collection of paths which guarantees arrival of each node from another only once. In that sense, a tree refers to collection of successful paths where a cut surface will not passed secondly.

In the second part of optimization process, all trees obtained from MCC are examined; trees with starting point at the boundary are selected first and other trees are connected to them from their starting points. At the end, all trees have separate boundary starting points and transformed separately to corresponding collections of paths. The advantage of this MCC-transformed optimization from MST lies in the higher freedom of movement increased by the abandonment of the objective of forming a single tree. In that sense, MST has not only higher number of connections, but also may contain higher cost connections to accomplish formation of a single tree. The pseudo code of this MCC transformed algorithm is shown below.

Inputs:

Uniform mesh grid points on the surface : N (number of grid points)
Force map : Map (N x N matrix)

Outputs:

Min. Cost Connections : MCC
MCC transformed path : MCCtf_path

"MCC"

FOR j = 1 to N : For each node of the mesh as destination
  $F_j = 999$: Set minimum cost of the node to 999 (Initialization)
  FOR i = 1 to N : For each node of the mesh as source
    IF $Map_{ij} < F_j$ THEN
      $MCC_j = i$: Set MCC of **j**th node to **i**
      $F_j = Map_{ij}$: Set minimum cost of **j**th node to Map_{ij}
    END IF
  END FOR
END FOR

```
"Trees & Starting Points (MCC Transformation)"
COMPUTE loops in MCC
FOR k = 1 to num_loops                    : For each loop of the MCC
   DELETE max. MCC of the loop            : Break up the loop by deleting the highest cost connection
STORE remained MCC of the loop
          as the k^th tree in Trees_MCC   : Store remained connections as the next tree
   STORE starting point of the k^th tree
          in Starts_Tree                  : Store the connection at the breakup point as starting point
END FOR

"Connection of Trees (MCC Transformation)"

FOR k = 1 to num_Trees_MCC                : For each tree of modified MCC
   IF Starts_Tree_k is at the boundary THEN
      STORE Trees_MCC_k in Trees_B        : Store trees with starting points at the boundary of the mesh
      STORE Starts_Tree_k in Start_B      : Store starting points at the boundary
   ELSE
      STORE Trees_MCC_k in Trees_I        : Store trees with starting points inside the mesh
      STORE Starts_Tree_k in Start_I      : Store starting points inside the mesh
END FOR

REPEAT
    FOR m = 1 to num_ Trees_B             : For each tree in Trees_B
       FOR n = 1 to num_ Trees_I          : For each tree in Trees_I
          IF Start_B_m neighbor to Trees_I_n THEN
             ADD Trees_B_m to Trees_I_n   : Connect tree with inner start to tree with boundary start
             DELETE Trees_B_m , Start_B_m : Delete connected tree and corresponding start point
             DECREMENT num_Trees_B        : Decrease in 1 the number of trees with inner start points
          END IF
       END FOR
   END FOR
UNTIL num_Trees_B = 0

"MCC Transformed Path"

INIT MCCtf_path                           : Initialize MCC transformed path
FOR n = 1 to num_Trees_I                  : For each tree in Trees_I
   COMPUTE paths of Trees_I_n             : Compute the collection of paths in Trees_I_n
   ADD paths to MCCtf                     : Add the collection of paths to the MCC transformed path
END FOR
```

Pseudo code of the MCC Transformed Path Algorithm

For a hypothetical map with 5x5 nodes where each node have a particular cost value towards its neighbors, obtained trees or paths and corresponding mean cost values are shown in Figure 3.23 for Minimum Cost Traveling Salesman (MCST), Minimum Spanning Tree (MST), Minimum Cost Connections (MCC) and MCC transformed path. For MCTS and MST Christofides heuristics and Prim's algorithm are preferred respectively (See Appendix). As mentioned previously, MCST has very low freedom of movement since its objective is to obtain one single path. Therefore, it has a considerably higher mean cost with a value of 36.20 compared to other optimization routines. Moreover, MST has a lower freedom than MCC since its objective is to obtain a single tree compared to MCC transformed path obtained from 3 trees. In that sense, the MCC transformed path has the lowest mean cost with a value of 18.07.

Thanks to the subplots 3 & 4, the MCC transformation can be clearly explained. In the beginning, MCC has 5 trees with two-connection loops. After loops are eliminated by deleting higher force connections in each loop, 3 trees with boundary starting point and 2 trees with inner starting point are obtained. In the next step, trees with inner starting points are connected to trees with boundary starting points. In the last step, these trees are transformed to collection of paths.

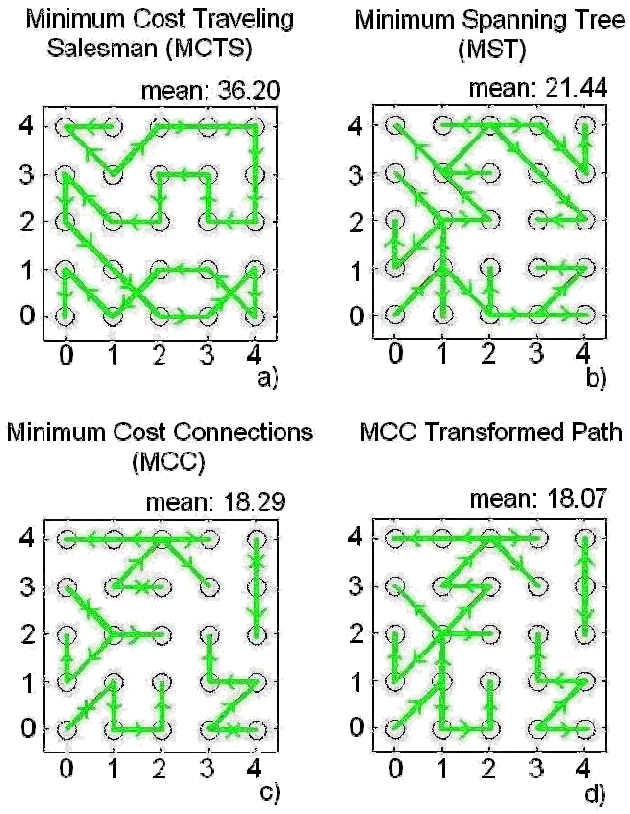

Figure 3.23 Optimization routines for a 5 x 5 force map

The objective of the optimization is minimization of the cutting forces; however the maximum cutting force value during the operation is not taken into account. Therefore, a correction process is used in the third part of the optimization where the minimum of the maximum cutting force results of standard zig direction simulations is selected and connections with higher than this value in MCC are separated for further cutting process in the corresponding zig direction of the selected minimum threshold. This part of the optimization guarantees the minimum threshold value of the standard zig operations and also decreases the mean value of the cutting forces. However, the addition of zig direction cutting parts to the collection of paths decreases the weight of the first objective of minimization of cutting forces. Therefore, the mean force obtained in the third part of the optimization is expected to be higher than mean force in the second part.

3.6. Optimization Results & Validation Tests

3.6.1. Experimental Setup

The experiments for calibration and validation were performed on Mazak FJV-200 UHS Vertical Machining Center (VMC) with 25000 rpm spindle motor, ± 2.5 micron sensitivity, and ± 0.7 micron repeatability. The tool was a carbide ball-end mill cutter from CoroMill Plura series of Sandvik with 12 mm diameter, 37 mm projection length and 30° helix angle. The workpiece material was aluminum blocks (Al7039) with dimensions of 250x170x38 mm. Kistler 3-component dynamometer (Model 9257B) and a charge amplifier have been used to measure cutting forces. The 3-component dynamometer has been fixed to the machine table using fixtures and the aluminum block was attached to the dynamometer using two M10 threaded screws as seen in Figure 3.24.

The cutting forces are sensed by the piezoelectric transducer in the dynamometer and an electric charge output is the outcome of this process. This electric charge is sent to the charge amplifier and converted into voltage output. The sensitivity values for the three channels (X, Y, and Z) of the amplifier were 7.93, 7.90, and 3.69 pC/N respectively. Amplifier gain for the device was set to 300 N/V for all channels. Subsequently, through use of a proper data acquisition card with 200 kS/s sampling rate, ± 10 V analog input and software, the voltage output is displayed and recorded as cutting forces in [N]. Displaying and recording of the measured data was

performed with data acquisition software, MALDAQ module of CutPro 8.0. Figure 5.2 shows a sample output screen of CutPro 8.0. The complete actual testing environment can be seen in Figure 5.3.

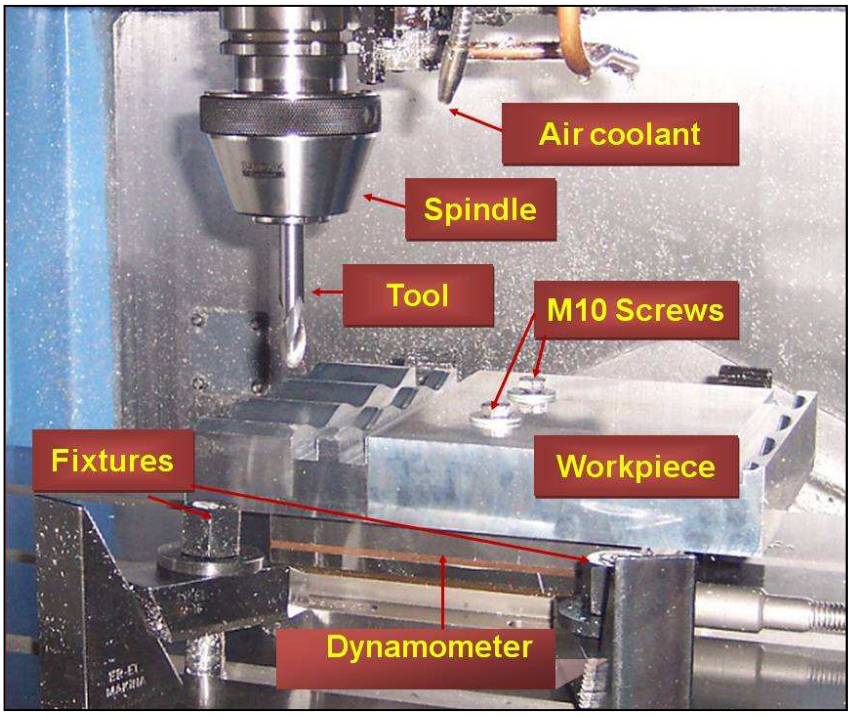

Figure 3.24 Workpiece and 3-component dynamometer fixed to VMC table for cutting tests

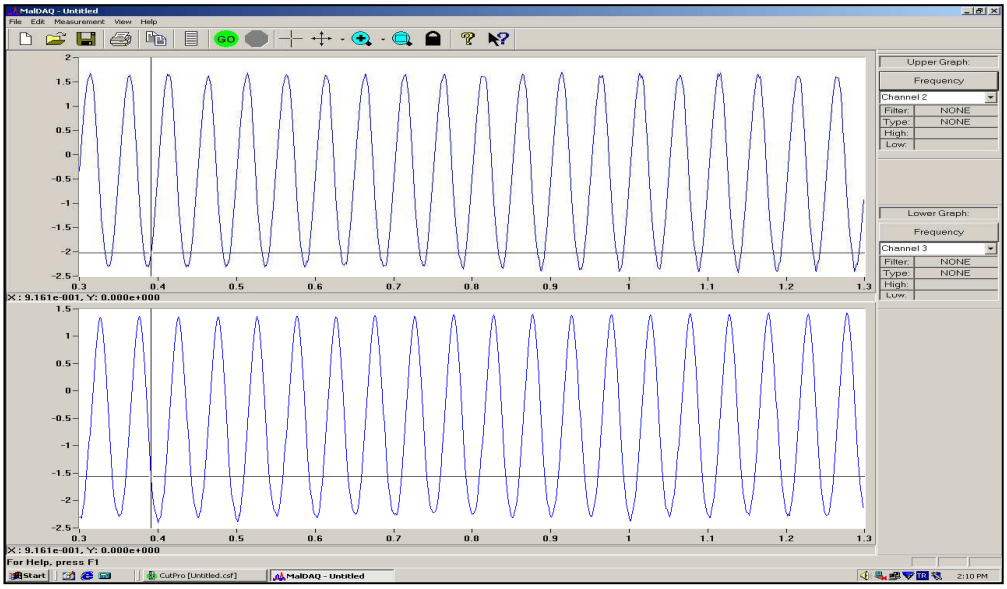

Figure 3.25 Sample output screen in CutPro 8.0 for cutting forces.

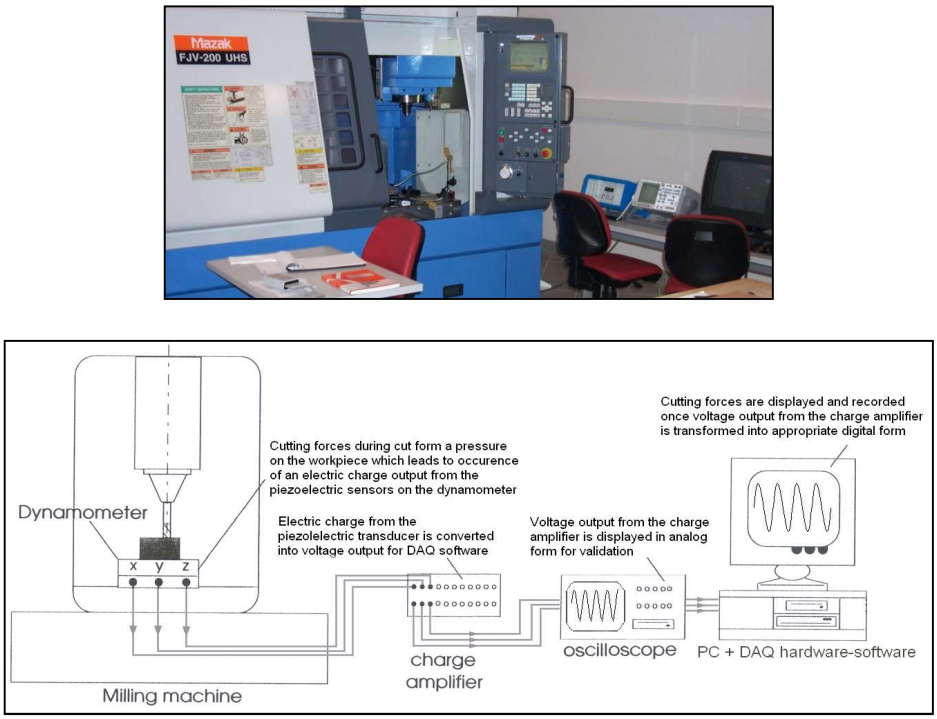

Figure 3.26 The experimental setup for measurement of cutting forces; a) Actual testing environment, b) Detailed illustration.

Differential chip height and the differential rotation angle in simulations were selected to be 0.1 mm and 3.6° respectively which adequately resembled the actual cutting conditions for the mathematical force model. The applied conditions and the results of the performed cutting tests are described in this chapter.

3.6.2. SAMPLE 1: Rough Cutting of Sine-Cosine Surface (170 mm x170 mm x 6 mm)

On the 3D surface shown in Figure 3.27-a, 121 CL points are determined with grid size at x = y = 17 mm for a uniform mesh. Force Map is obtained by total of 840 cutting simulations with ball-end mill with diameter of 12 mm each for one connection of the CL points. Figure 3.27-b depicts the formed force map. The grid size of the engagement tool is z = 62.5 μ, x = y = 312.5 μ, where the engagement of the cutting tool with the workpiece is determined during the whole cutting process. In this case, the step over is higher than tool diameter and the global optimum could be determined with a static global optimization, since the cutting of any edge (or neighborhood) does not affect the possible engagement of the uncut edges. In other words, all cutting operations of the edges between the CL points are exactly slot cutting simulations.

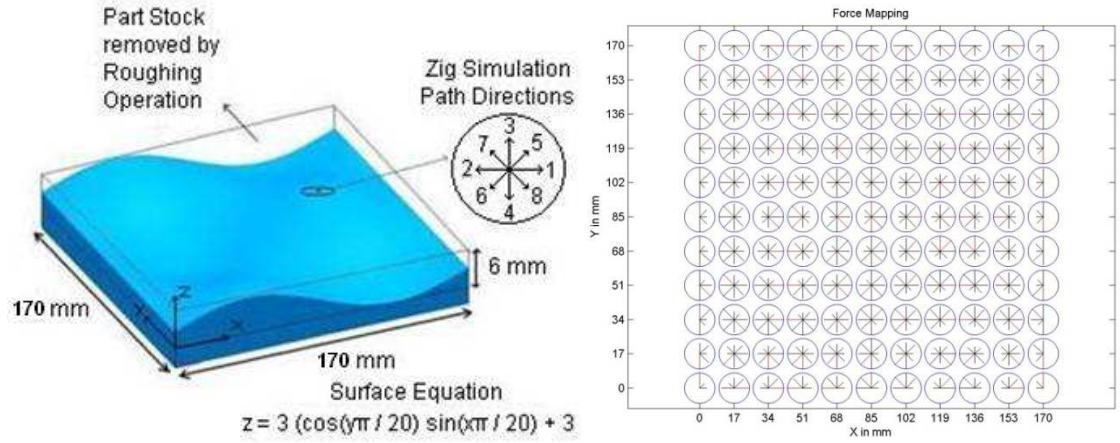

(a) (b)

Figure 3.27 a) Solid model of the sin–cos free form surface b) Global force map.

The collection of the paths are obtained with MCC-transformed optimization and depicted in figure 3.28-a; small circles are start points and crosses are end points of the 2D path. The 3D representation of the tool path on the part surface is shown in figure 3.28-b.

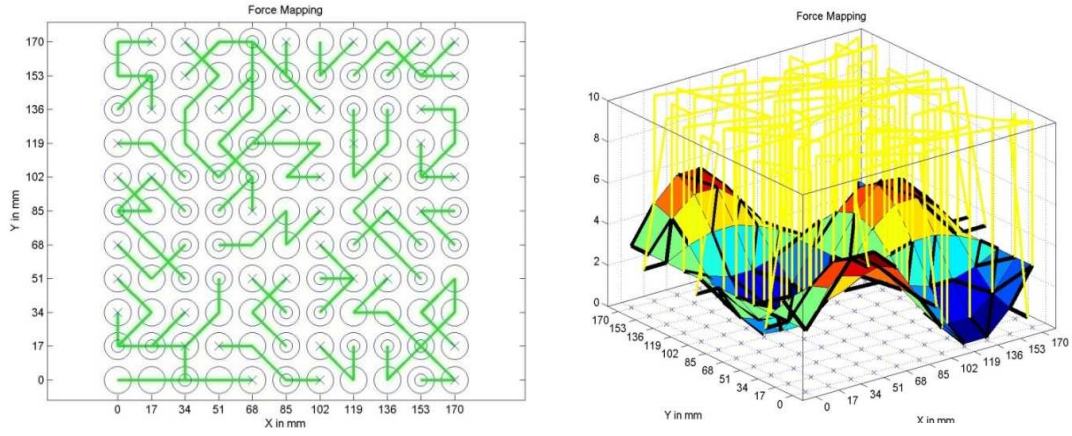

(a) (b)

Figure 3.28 Optimized path shown on the cutting surface a) in 2D & b) in 3D

Comparing simulated cutting forces of 8 predetermined zig paths with the optimized path cutting forces in Figure 3.29, the optimized forces are below 320 N which reaches up to 400 N in standard zig tool path cutting simulations. So, the upper limit for the cutting forces reduces 20% for the optimized tool path. Also the average force in optimized path is 185 N which is 15% lower than 217 N, the minimum of the other 8 paths.

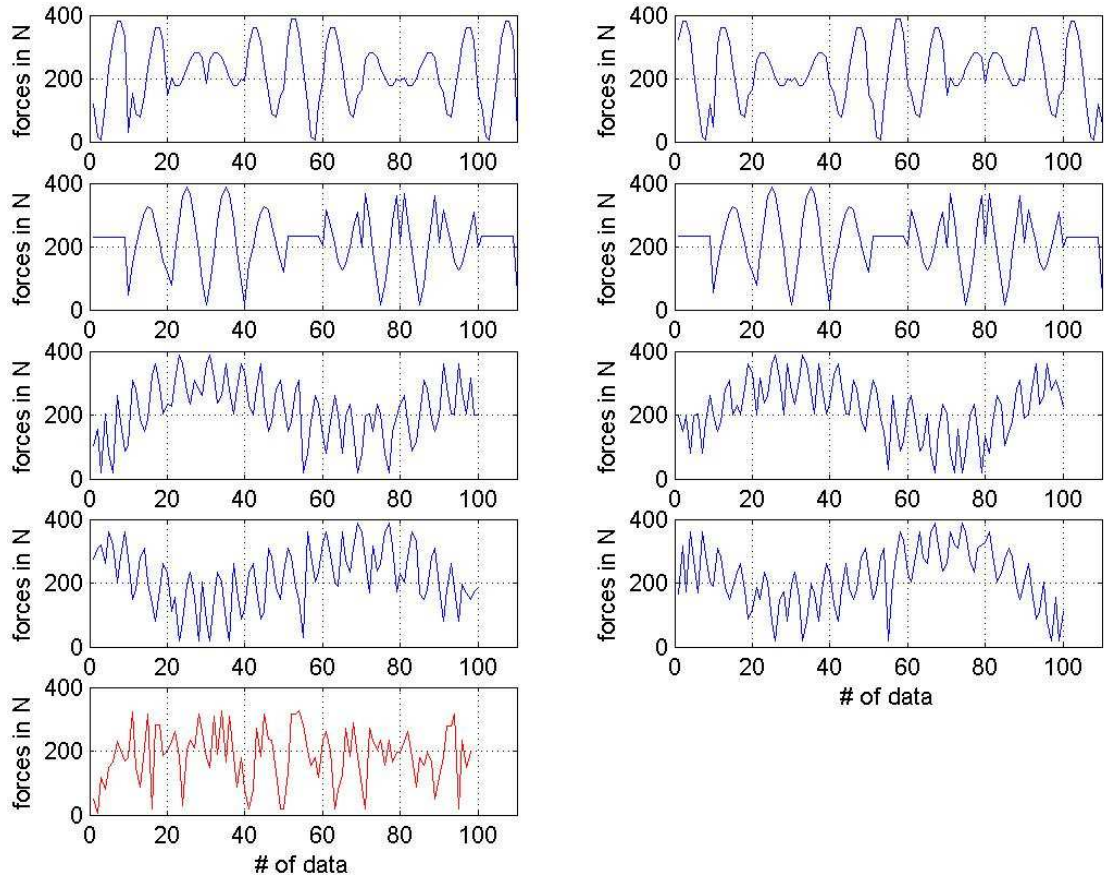

Figure 3.29 Cutting forces of 8 zig path simulations vs of optimized path using force map

Experimental validation test are performed also to compare the simulated cutting force results with the experimental cutting forces with the same conditions. In Figure 3.30 and 3.31, the experimental cutting force results and simulation cutting forces for optimized path are compared where the simulation forces in Figure 3.30 contain the whole simulation cutting forces of the operation; on the other hand Figure 3.31 depicts the simulation forces obtained from the force map. In both figure, the experimental and simulated forces are very close. Also comparing Figure 3.30 and 3.31, the validation of the force map is done.

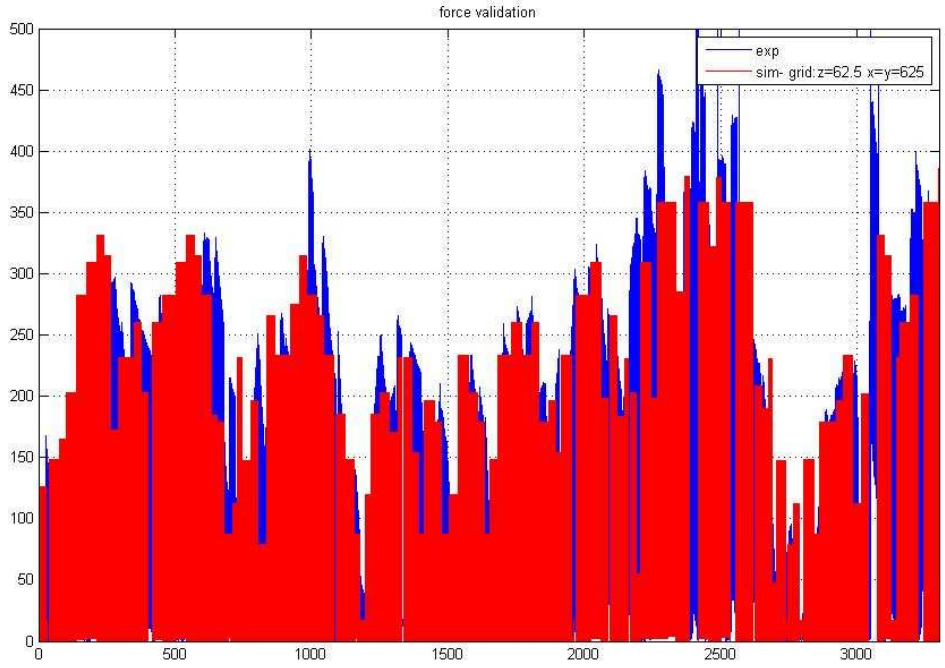

Figure 3.30 Experimental cutting force results vs simulation cutting forces for optimized path

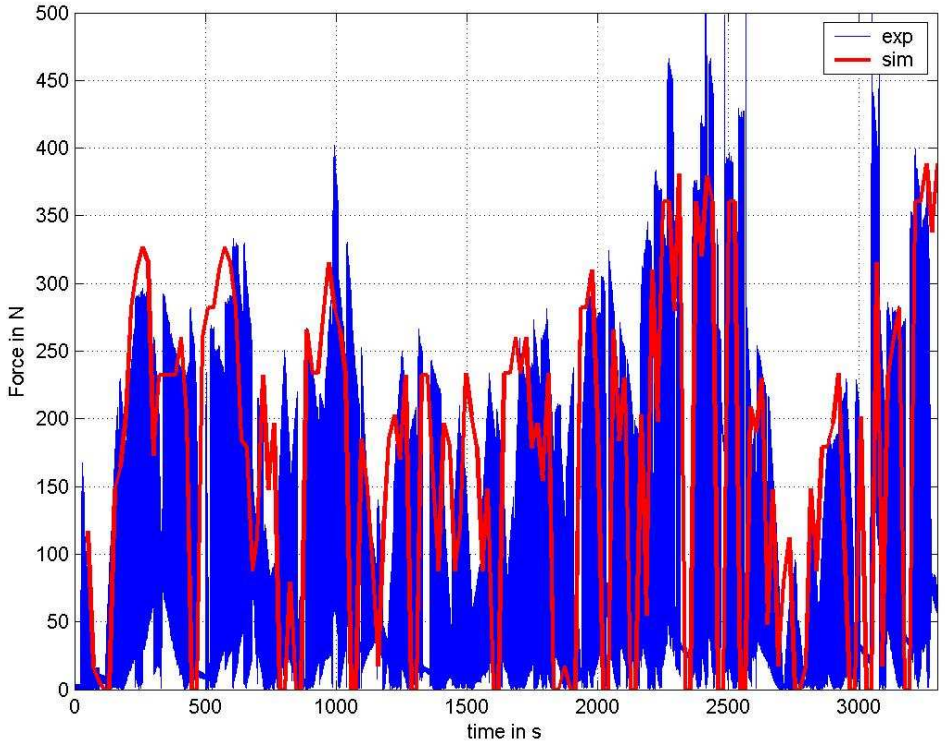

Figure 3.31 Exp. cutting force results vs forces obtained from force map for optimized path

3.6.3. SAMPLE 2: Sine-Cosine Surface (40 mm x 40 mm x 6 mm):

On the 3D surface shown in Figure 3.32, 441 CL points are determined with grid size at x = y = 2 mm for a uniform mesh. Force Map is obtained by total of 3280 slot cutting simulations with ball-end mill with diameter of 12 mm each for one connection of the CL points, and shows the inversely proportional weight of the force magnitudes for each CL point in all of the 8 directions relatively to each other where large magnitudes are depicted with short lines and small magnitudes with longer lines. Figure 3.33 depicts formed force map. The grid size of the engagement tool is z = 62.5 μ, x = y = 312.5 μ, where the engagement of the cutting tool with the workpiece is determined during the whole cutting process.

Figure 3.32 Solid model of the sin-cos surface

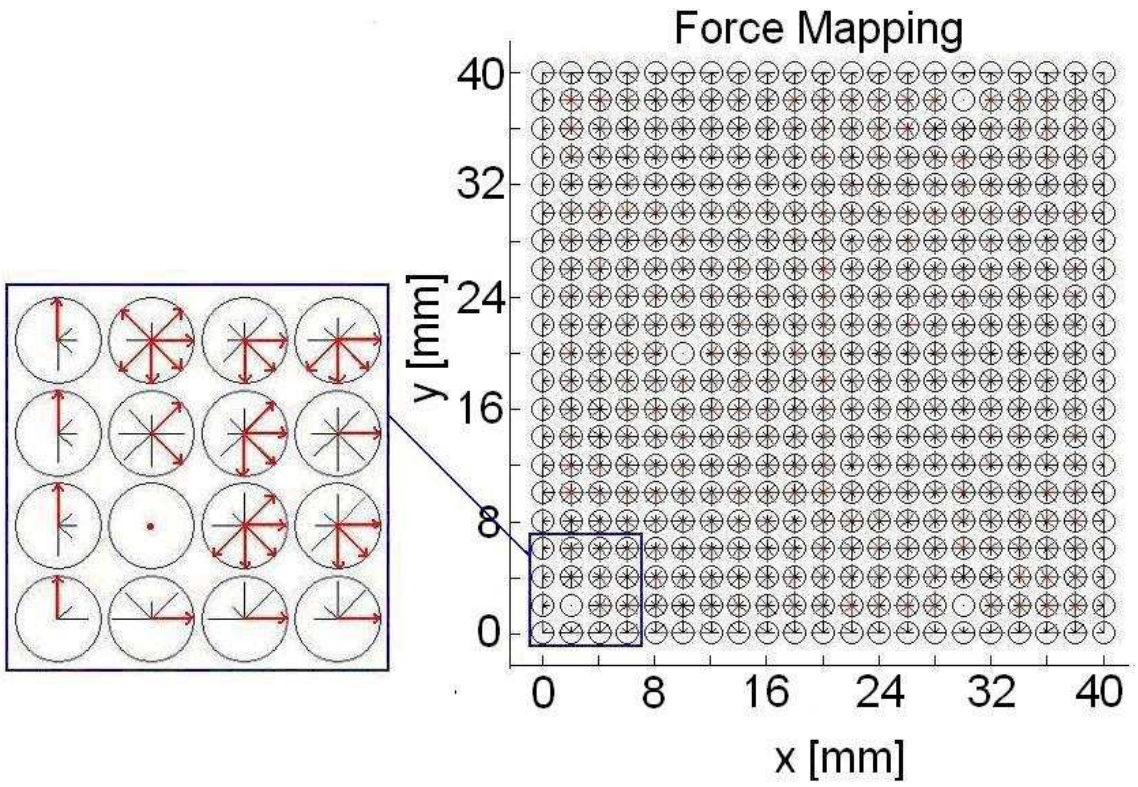

Figure 3.33 Force map and a zoomed section

Since the step over is lower than tool diameter, the slot cutting simulation forces could only be reference values for the optimization, and the possible engagement and the cutting forces of each edge directly depends on the number and position of the cut edges and decreases once the edges in the neighborhood were cut. In that sense, the reference value for each edge obtained from slot cutting simulation determines the maximum threshold of the cutting force. So, it is expected that the cutting simulation forces of the total tool path obtained from optimization would lie under the cutting forces from the force map for the optimized tool path.

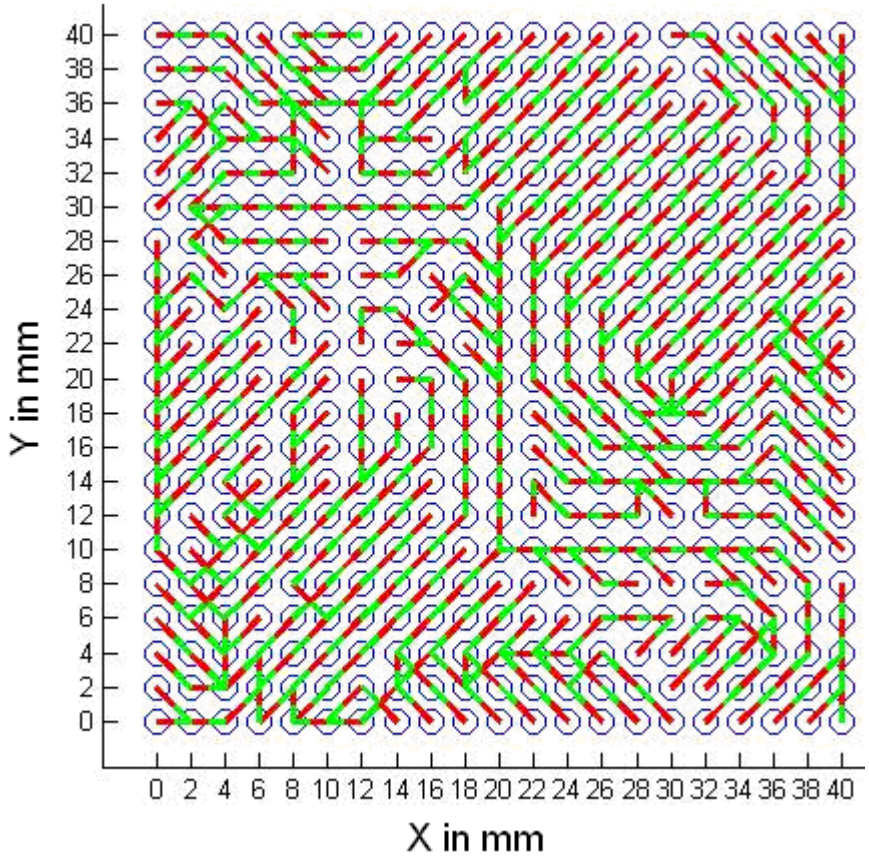

Figure 3.34 Minimum cost connection for the force map

Minimum Cost Connections are obtained as shown in Figure 3.34. The direction of each connection is shown as from green to red part. Further, the collection of the paths are obtained from MCC-transformed optimization and depicted in Figure 3.35; small circles are start points and crosses are end points of the 2D path.

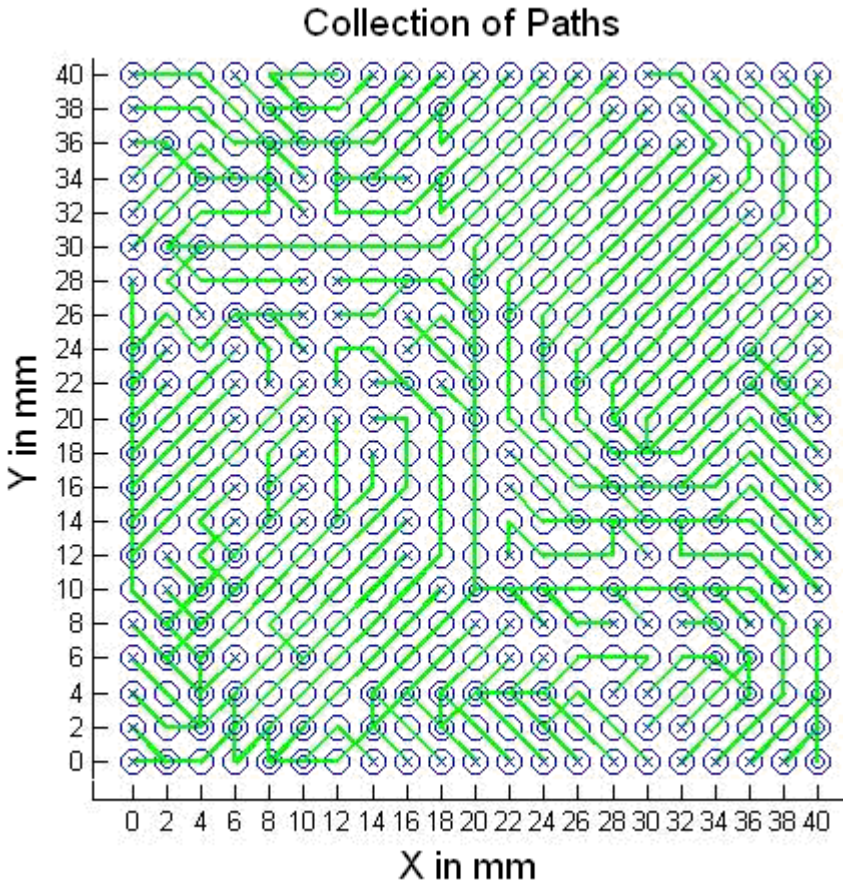

Figure 3.35 Collection of paths from MCC-transformed optimization

Cutting forces for standard zig tool paths obtained from the cutting simulations are depicted in Figure 3.36. On the other hand, cutting forces for optimized tool path obtained both from the force map and the cutting simulation are depicted in the Figure 3.37.

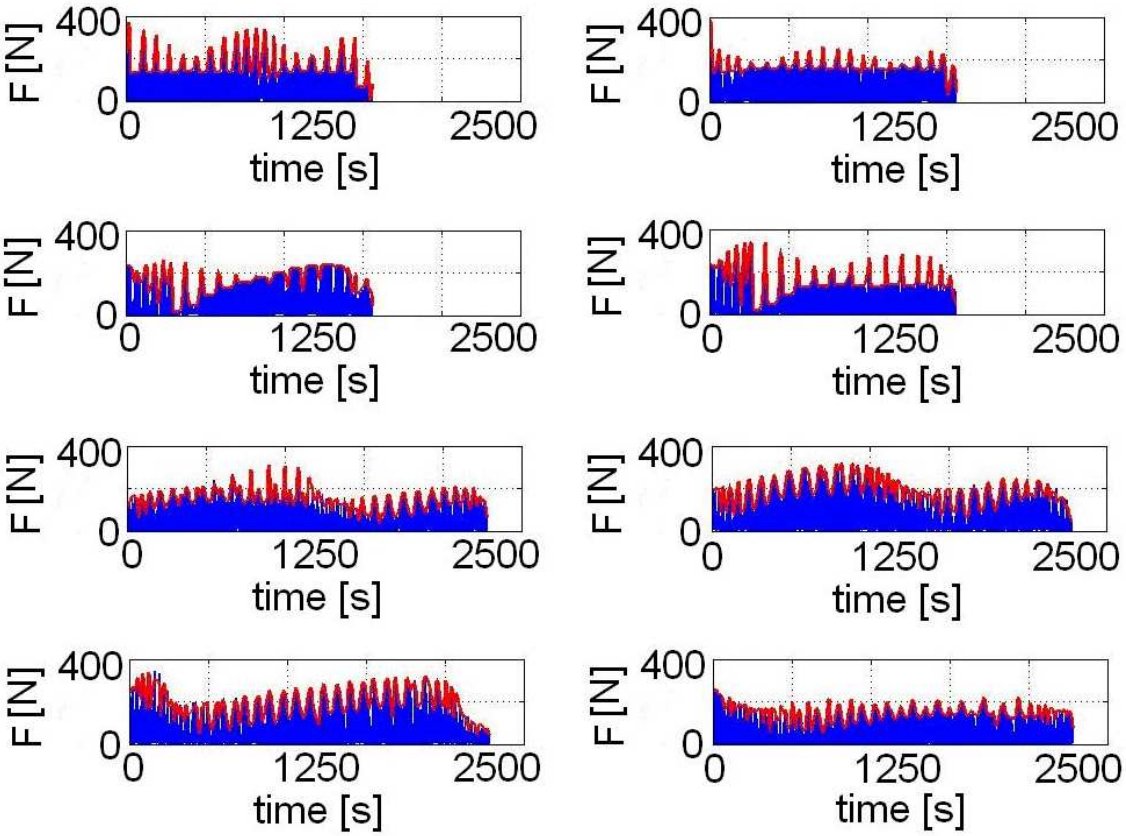

Figure 3.36 Simulated cutting forces

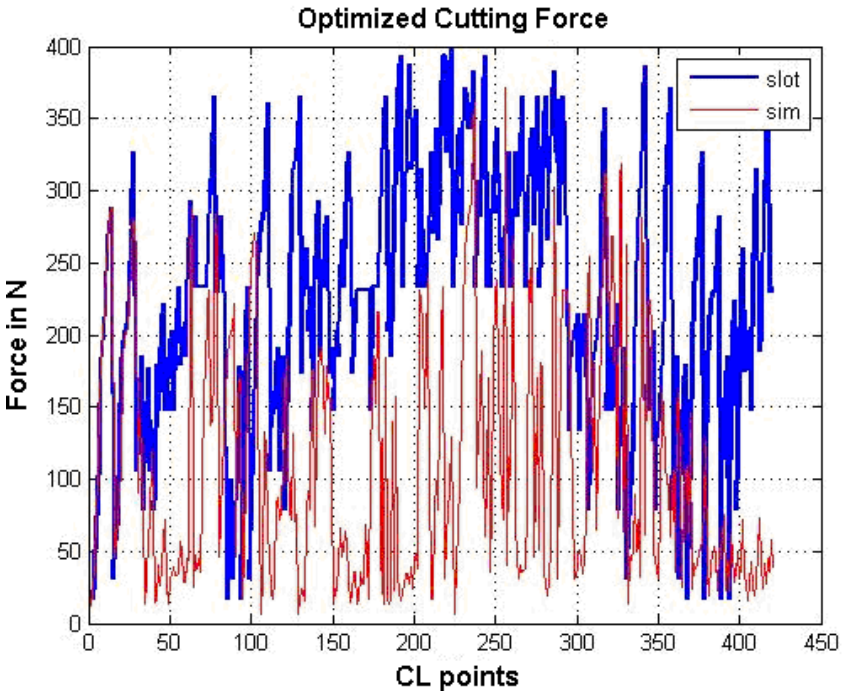

Figure 3.37 Cutting forces of optimized path

The mean and maximum forces are tabulated both for cutting forces obtained from force map and simulations. As shown in the Table 3.3 below, mean forces obtained from force map only decreases 8% for the optimized tool path and maximum force can not be decreased since in CL points with highest depth of cut all slot cutting directions results in higher forces. As compared in simulation results, the decrease in mean forces reaches up to 24%, however maximum force value is nearly 50% higher than possible minimum of the maximum of 8 standard tool paths. The difference in maximum cutting force value in simulations results from early chip removal and dynamical change of the cutting tool engagement occurred during the operation.

Table 3.3 Comparison of mean and maximum resultant forces between eight standard tool paths and optimized tool path.

	Zig 1	**Zig 2**	**Zig 3**	**Zig 4**	**Zig 5**	**Zig 6**	**Zig 7**	**Zig 8**	**Opt**
Slot-mean	240	**239**	240	240	244	245	245	245	**222** *-8%*
Slot-max	399	399	399	399	399	399	399	399	399
Sim-mean	162	140	131	150	118	148	148	**117**	**94** *-24%*
Sim-max	372	385	253	341	308	315	341	**252**	**375**

For the correction part of the optimization, firstly the minimum of the maximum cutting force is determined. Since cutting in direction 8 offers maximum cutting force of 253 N, all connections in MCC higher than this value are separated for further cutting in direction 8 and other connections are again processed in the second part of the optimization. The corrected collection of tool paths in 2D is shown in

figure 3.38-a respectively where green paths obtained from updated MCC-transformed optimization and red colored paths are corrected ones cut in direction 8.

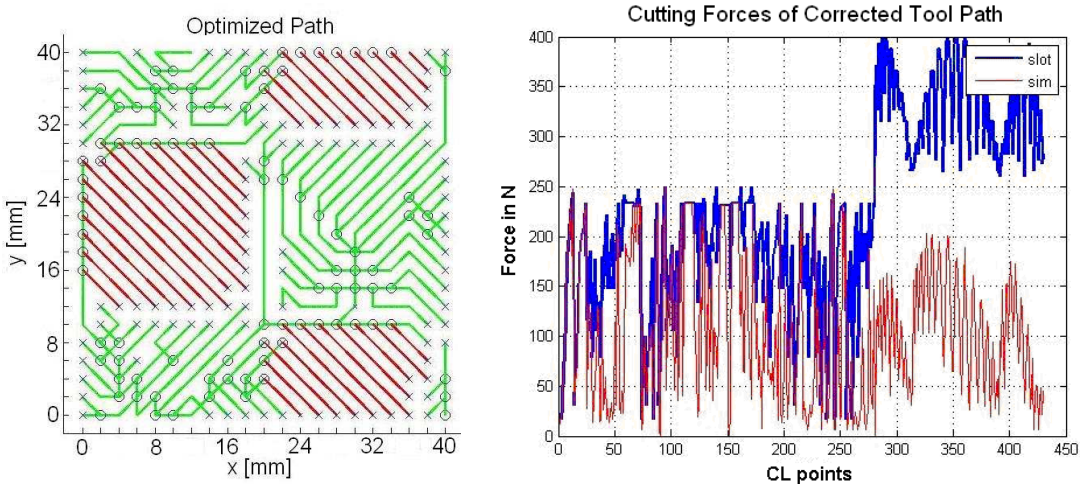

(a) (b)

Figure 3.38 (a) Corrected tool path (b) Forces of corrected tool path

Cutting forces for the corrected tool path obtained from the force map and cutting simulations are depicted in Figure 3.38-b. Furthermore, mean and maximum forces are tabulated both for cutting forces obtained from force map and simulations.

As shown in Table 3.4 below, the weight of the first optimization objective is decreased where the reduction of mean value for the corrected tool path decreases to 5% in the cutting forces obtained from force map and to 13% in the cutting simulations. However, the threshold value is lowered to 249 N. In that sense, with the correction part the optimization method guarantees minimum threshold value of standard zig operations and also decreases mean value of cutting forces up to 13% of the best standard zig operation selection for minimum mean cutting force.

In other words, it is observed that with the optimized tool path can be reached to the minimum average resultant force magnitude along the machining. Depending on the directions, the optimum path can achieve from 13% to 57% less mean force without

violating the preset maximum force threshold (250 N). Moreover, in the optimal tool path the decrease on the maximum force magnitude could reach up to 54%.

Experimental validation test is performed to compare the simulated cutting force results with the experimental cutting forces with the same conditions. In Figure 3.39, the experimental cutting force results and simulation cutting forces for optimized path are compared. As shown in the figure 3.39, the experimental and simulated forces are very close and so simulation results are reliable.

Table 3.4 Comparison of mean and maximum resultant forces between eight standard tool paths and optimized tool path.

	Zig 1	**Zig 2**	**Zig 3**	**Zig 4**	**Zig 5**	**Zig 6**	**Zig 7**	**Zig 8**	**Opt**	**Opt corrected**
Slot-mean	240	**239**	240	240	244	245	245	245	**222** - *7%*	***227*** *-5%*
Slot-max	399	399	399	399	399	399	399	399	399	399
Sim-mean	162	140	131	150	118	148	148	**117**	**94** *-24*	**104** *-13*
Sim-max	372	385	253	341	308	315	341	252	**375**	**249**

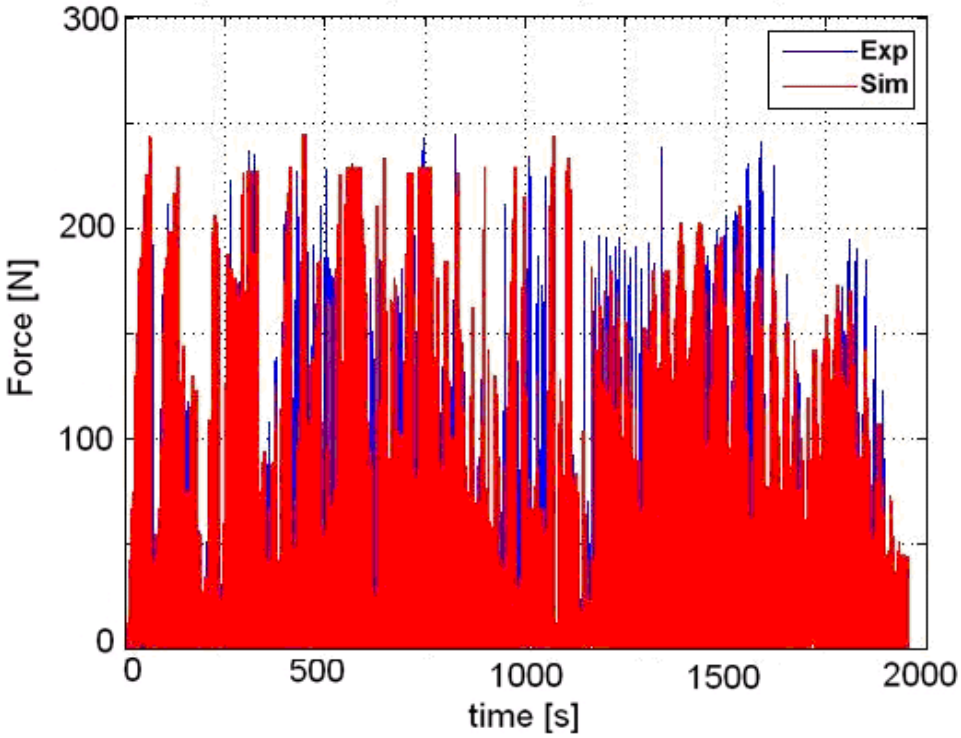

Figure 3.39 Simulation & experimental cutting forces for optimized path

Simulated and experimentally measured resultant forces as well as their envelopes are also shown for the generated optimal path of the free form surface in Figure 3.40. In this figure, blue, black and red colors are showing for instantaneous forces, envelopes of experimental and simulated forces, respectively. First of all, it is seen that the simulated and experimental forces are matching quite well. The maximum force in the optimal simulation is below 250 N as preset value both in the simulation and in the experiment. Further in figure 3.41, simulated cutting force envelopes of standard tool paths are compared with the simulated optimized cutting force envelope.

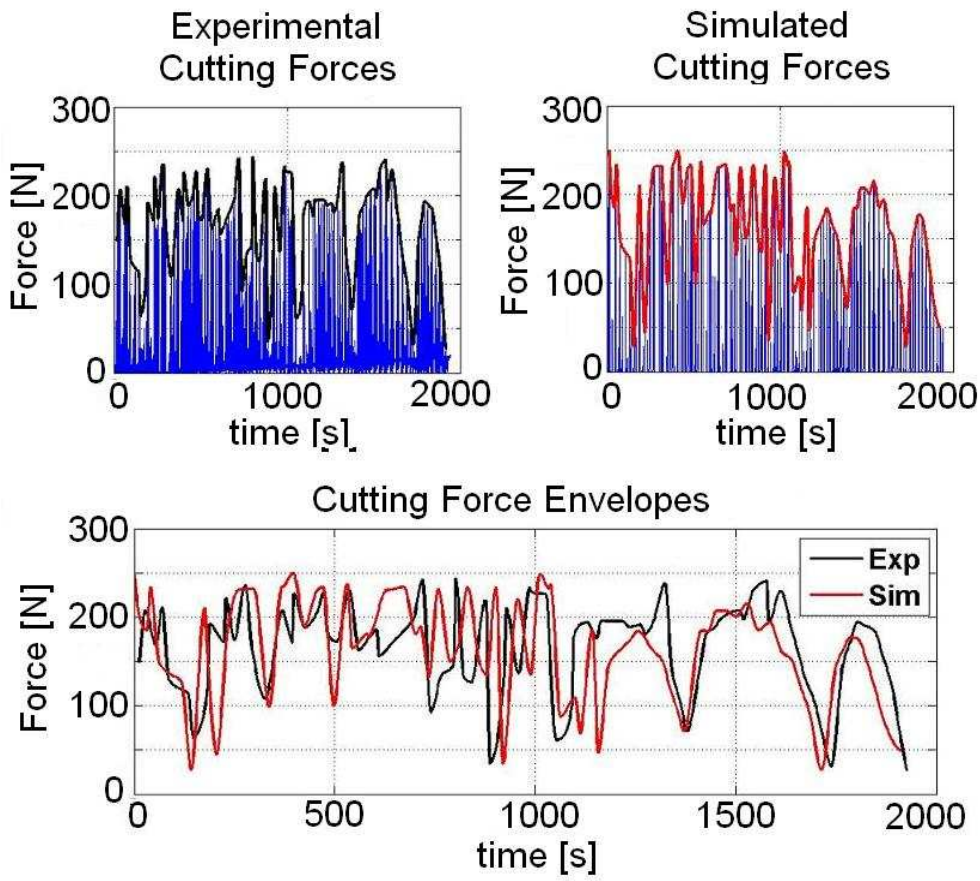

Figure 3.40 Comparing simulated and experimentally measured resultant forces for the optimized tool path

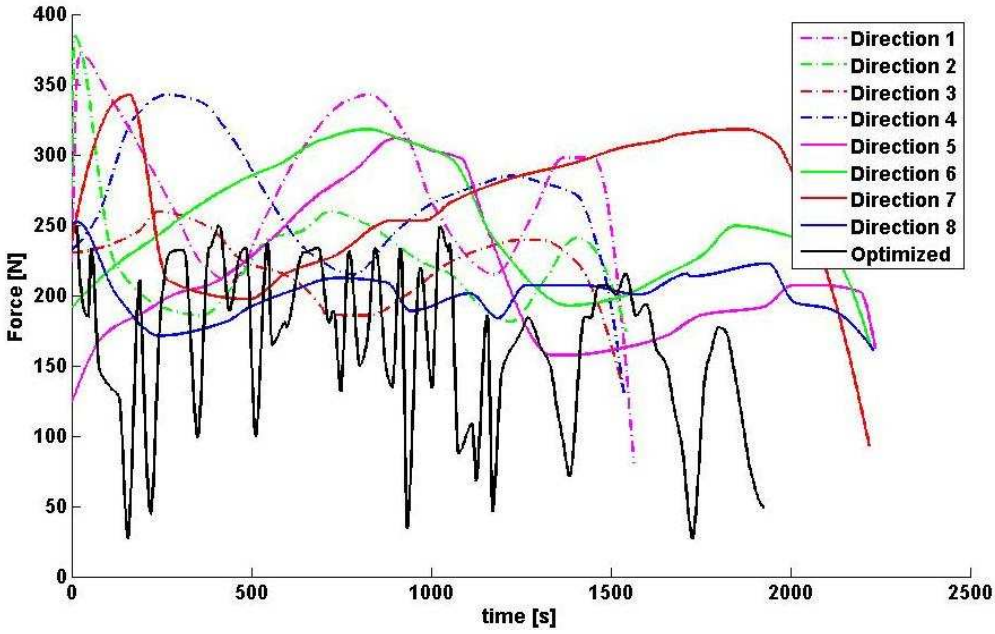

Figure 3.41 Comparison of resultant force envelopes for the eight different tool paths and optimized tool path

The simulated and machined free form surface and optimized tool path in 3D are shown in Figure 3.42.

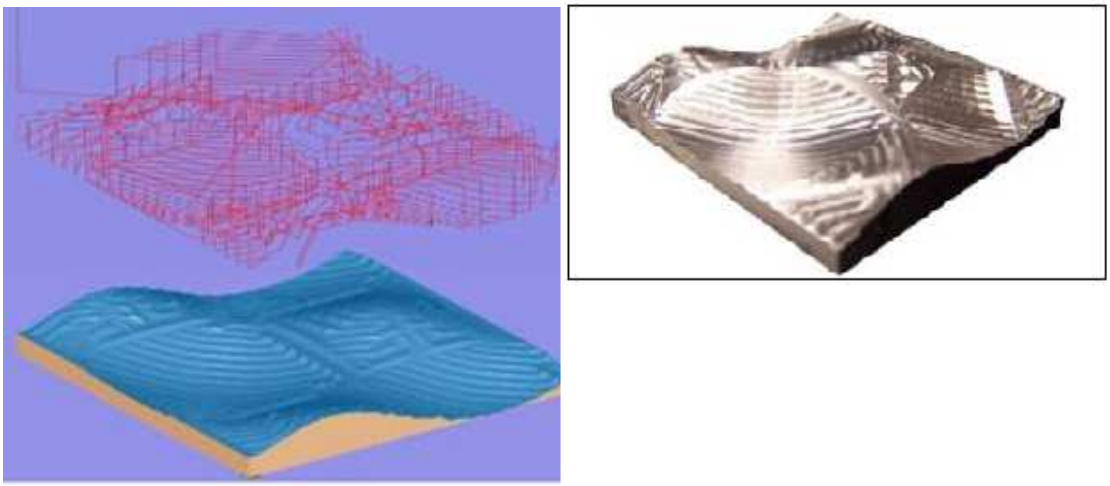

(a) (b)

Figure 3.42 Simulated and machined free form surface and optimized tool path in 3D.

3.6.4. SAMPLE 3: Ataturk Portrait (30 mm × 30 mm × 6 mm)

256 CL points are determined with grid size at x = y = 2 mm for a uniform mesh using collision detection based algorithm and shown in Figure 3.43 with the solid model together. Force Map is obtained by total of 1860 slot cutting simulations with ball-end mill with diameter of 12 mm each for one connection of the CL points. Figure 3.44 depicts formed force map. The grid size of the engagement tool is z = 62.5 μ, x = y = 312.5 μ, where the engagement of the cutting tool with the workpiece is determined during the whole cutting process.

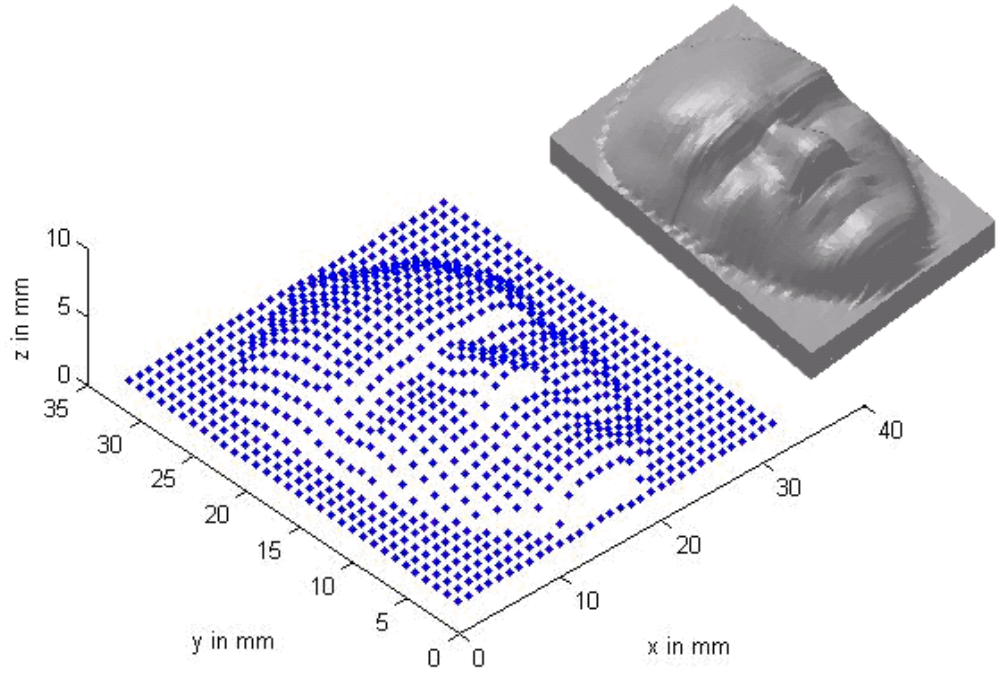

Figure 3.43 3D CAD model and CL points of Ataturk portait

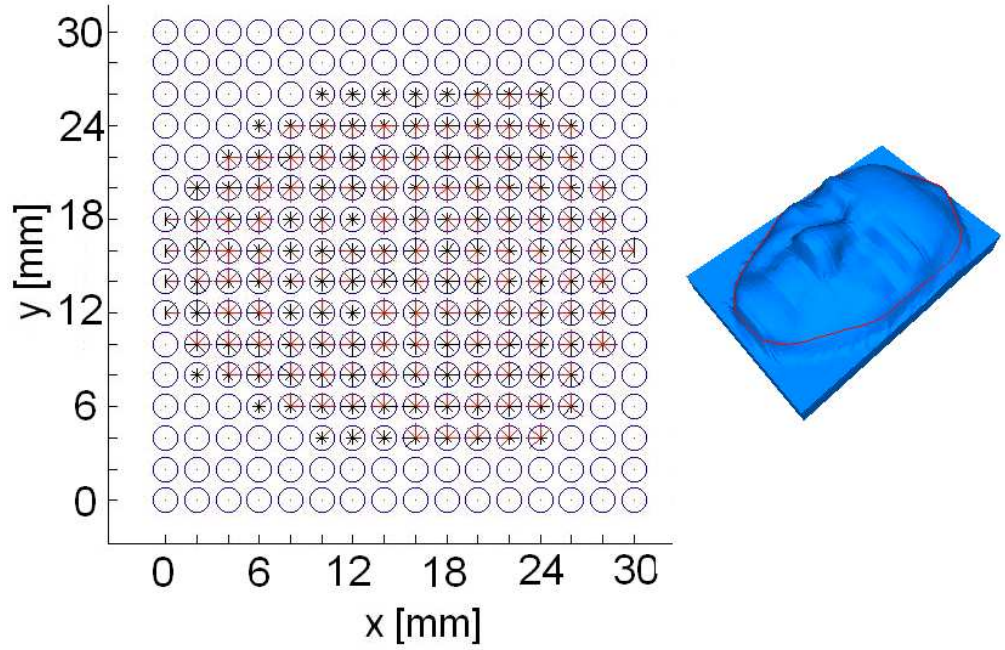

Figure 3.44 Force map for Ataturk portait

The collection of the paths are obtained from MCC-transformed optimization and depicted in Figure 3.45; small circles are start points and crosses are end points of the 2D path.

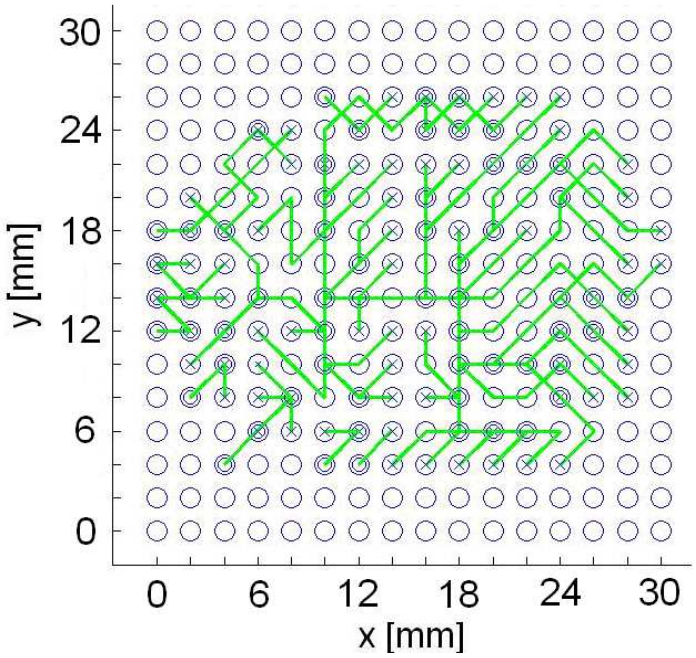

Figure 3.45 Optimized tool path for Ataturk portrait in 2D

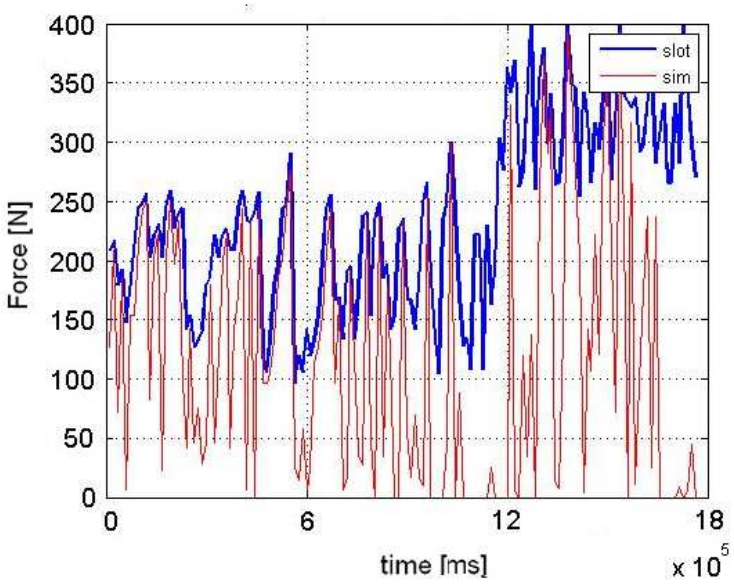

Figure 3.46 Simulated resultant forces vs resultant forces from force map

Cutting forces for the optimized tool path obtained from the force map and cutting simulations are depicted in Fig. 3.46.

Mean and maximum forces are tabulated both for cutting forces obtained from force map and simulations. The mean and maximum force results of the optimized tool path are compared with the results of the cutting simulations in 8 zig directions are shown in Table 3.5. Depending on the directions, the optimum path achieves from

15% to 30% less mean force without violating the preset maximum force threshold (400 N). In this case, there is no need for correction part since all the boundary of the free form part has the highest and same depth of cut of 6 mm. In that sense, the maximum cutting force does not depend on the direction of the tool path and occurs at the boundary cutting.

Table 3.5 Comparison of mean and maximum resultant forces between eight standard tool paths and optimized tool path.

	Zig 1	**Zig 2**	**Zig 3**	**Zig 4**	**Zig 5**	**Zig 6**	**Zig 7**	**Zig 8**	**Opt**
Slot-mean	249	258	260	259	253	261	263	**248**	**222** *-12%*
Slot-max	399	399	399	399	399	399	399	399	399
Sim-mean	139	141	148	164	152	157	143	**136**	**115** *-15%*
Sim-max	399	399	399	399	399	399	399	399	399

The simulated and machined free form surface and optimized tool path in 3D are shown in figure 3.47.

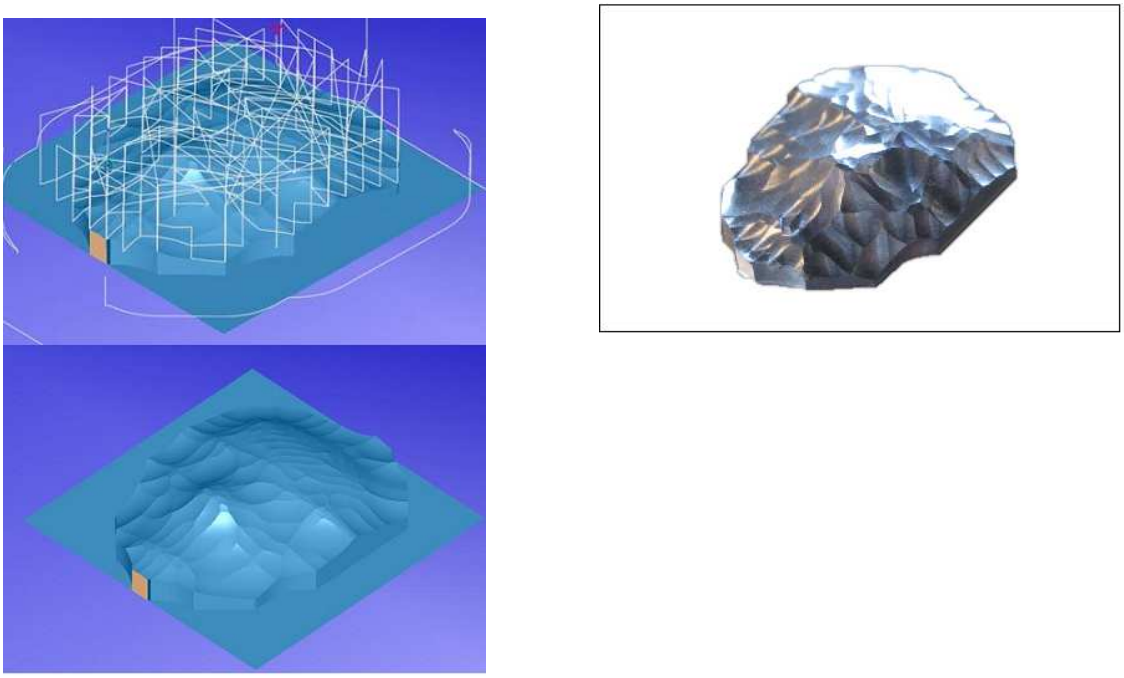

(a) (b)

Figure 3.47 (a) Simulated and (b) machined free form surface and optimized tool path in 3D.

Experimental validation test is performed to compare the simulated cutting force results with the experimental cutting forces with the same conditions. In Figure 3.48, the experimental cutting force results and simulation cutting forces for optimized path are compared. It is seen that the simulated and experimental forces are matching quite well.

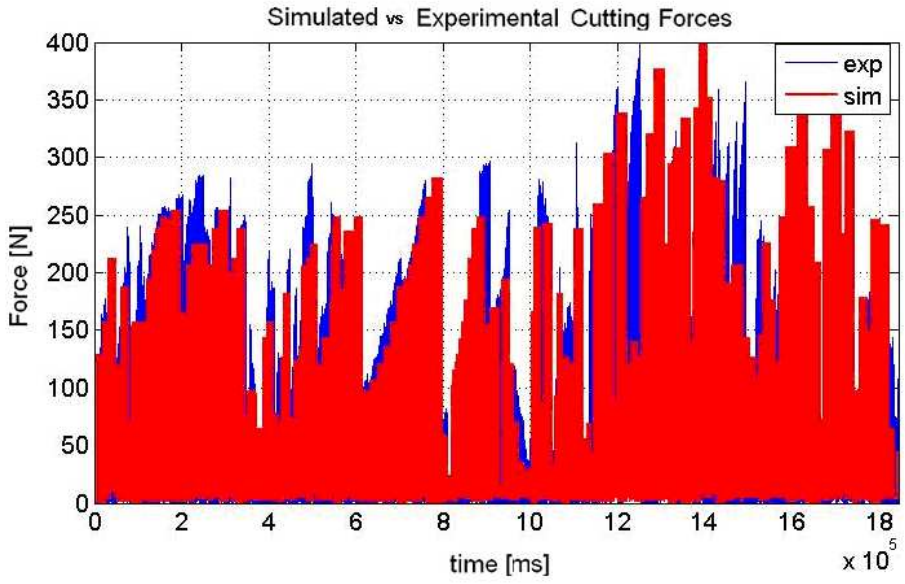

Figure 3.48 Comparing simulated and experimentally measured resultant forces for the optimized tool path.

3.6.5. SAMPLE 4: Buddha Figure (30 mm x 30 mm x 6 mm)

256 CL points are determined with grid size at x = y = 2 mm for a uniform mesh using collision detection based algorithm and shown in Figure 3.49 with the solid model together. Force Map is obtained by total of 1860 slot cutting simulations with ball-end mill with diameter of 12 mm each for one connection of the CL points. Figure 3.50 depicts formed force map. The grid size of the engagement tool is z = 62.5 μ, x = y = 312.5 μ, where the engagement of the cutting tool with the workpiece is determined during the whole cutting process.

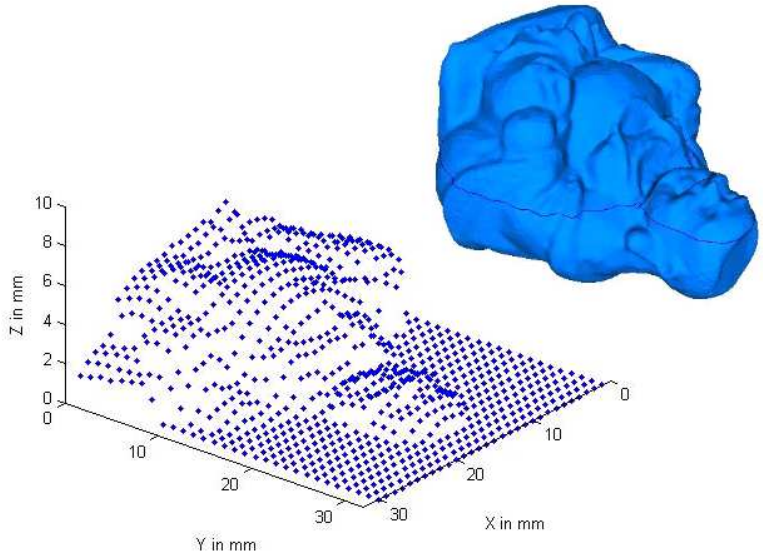

Figure 3.49 3D CAD model and CL points for Buddha Figure

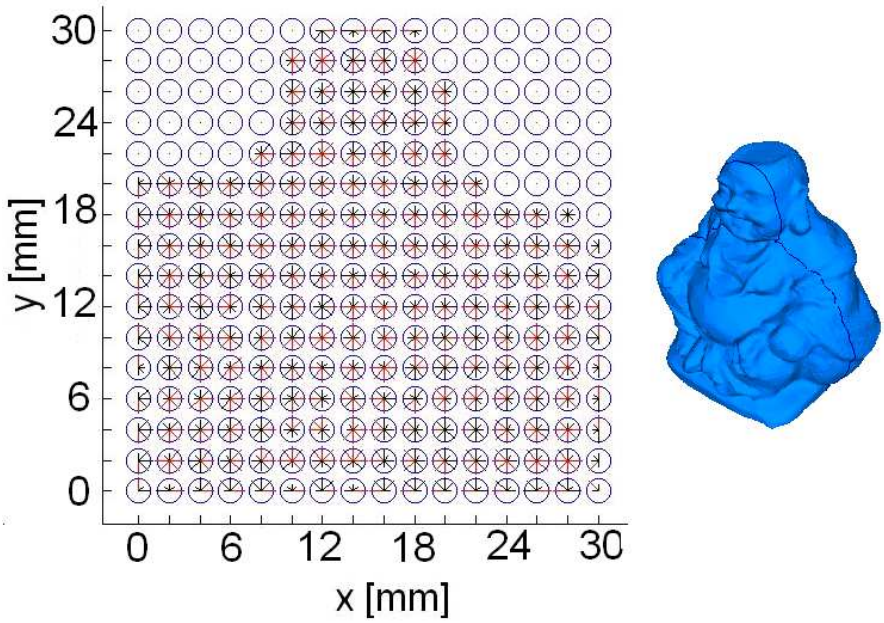

Figure 3.50 Force map for Buddha figure

The collection of the paths are obtained from MCC-transformed optimization and depicted in Figure 3.51; small circles are start points and crosses are end points of the 2D path.

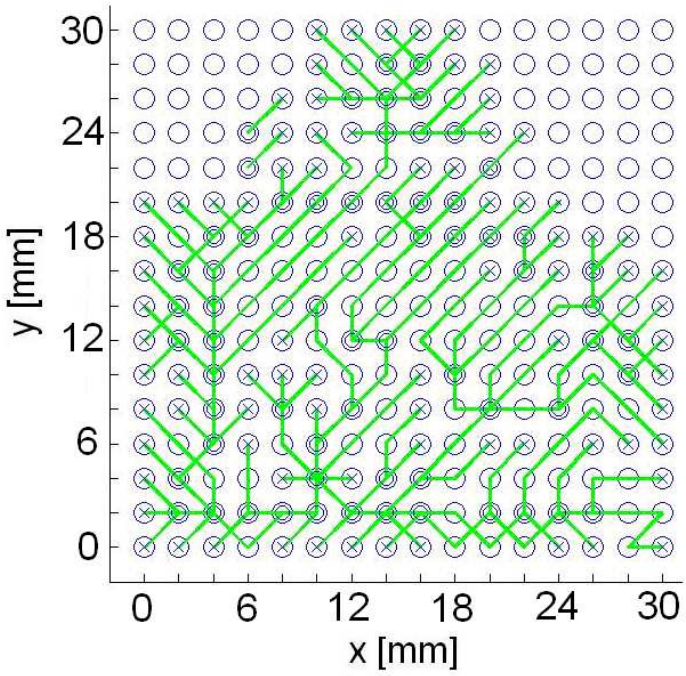

Figure 3.51 Optimized tool path for Buddha figure in 2D

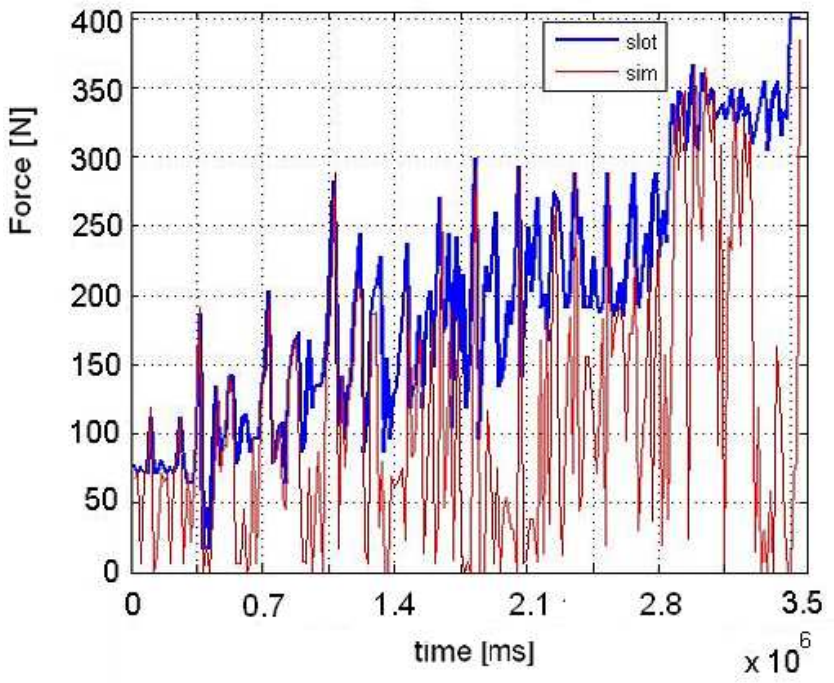

Figure 3.52 Simulated esultant forces vs resultant forces from force map

Cutting forces for the optimized tool path obtained from the force map and cutting simulations are depicted in Figure 3.52.

Mean and maximum forces are tabulated both for cutting forces obtained from force map and simulations. The mean and maximum force results of the optimized tool path are compared with the results of the cutting simulations in 8 zig directions are shown in Table 3.6. Depending on the directions, the optimum paths achieve from 15% to 46% less mean force without violating the preset maximum force threshold (400 N). In the optimal tool path the decrease on the maximum force magnitude could reach up to 4%.

In this case, there is again no need for correction part since all the boundary of the free form part has the highest and same depth of cut of 6 mm. In that sense, the maximum cutting force does not depend on the direction of the tool path and occurs at the boundary cutting.

Table 3.6 Comparison of mean and maximum resultant forces between eight standard tool paths and optimized tool path.

	Zig 1	**Zig 2**	**Zig 3**	**Zig 4**	**Zig 5**	**Zig 6**	**Zig 7**	**Zig 8**	**Opt**
Slot-mean	219	222	222	224	**210**	236	212	233	**197** *-7%*
Slot-max	399	399	399	399	399	399	399	399	399
Sim-mean	149	123	130	140	**117**	142	121	134	**102** *-15%*
Sim-max	399	400	399	401	399	398	403	397	384

The simulated and machined free form surface and optimized tool path in 3D are shown in Figure 3.53.

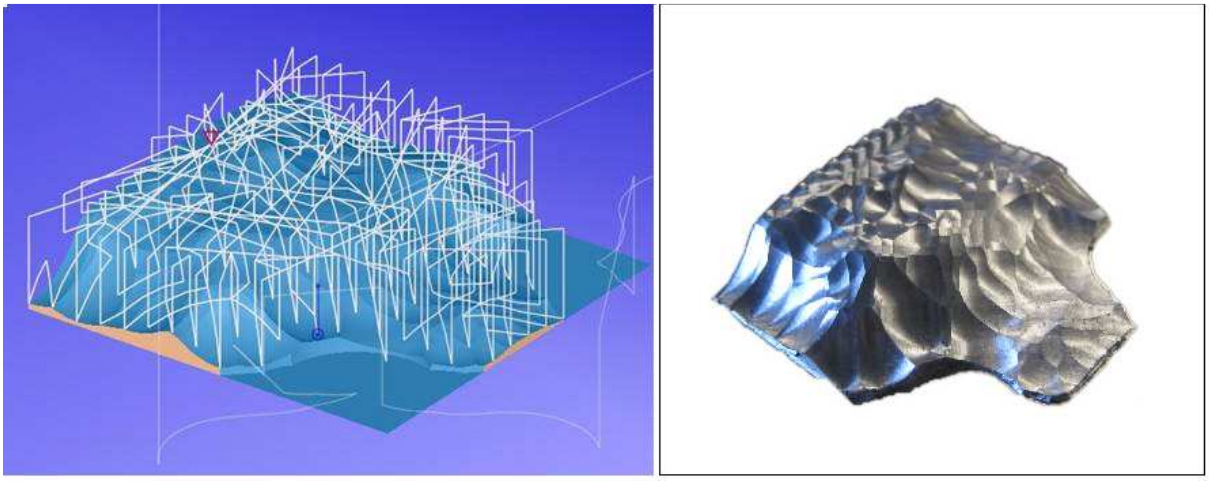

Figure 3.53 Simulated and machined free form surface and optimized tool path in 3D.

Experimental validation test is performed to compare the simulated cutting force results with the experimental cutting forces with the same conditions. In Figure 3.54, the experimental cutting force results and simulation cutting forces for optimized path are compared. It is seen that the simulated and experimental forces are matching quite well.

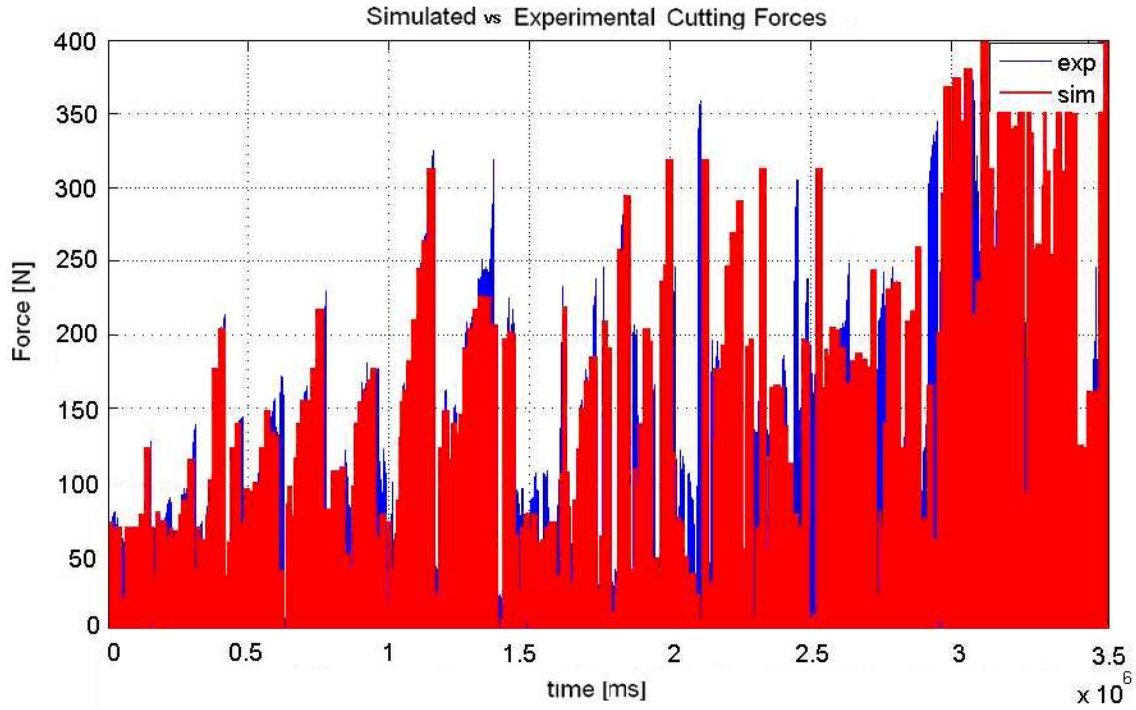

Figure 3.54 Comparing simulated and experimentally measured resultant forces for the optimized tool path

3.6.6. Discussion

Various samples are used to test and validate force-based tool path optimization routine. Depending on the directions, the tool path optimization process reduces mean value of the cutting forces from 13% to 57% compared to standard zig tool path cutting forces without violating the preset maximum force threshold which equals to the minimum of the maximum cutting forces of the standard tool paths. Moreover, in the optimal tool path the decrease in the maximum cutting force magnitude could reach up to 54% compared to standard tool paths. At the end of each optimized cutting simulation, experimental validation tests are performed where simulation and experimental results are compared and closely agreed.

Chapter 4
Multi-Criteria Tool path Optimization

4.1. Introduction

Multi-criteria tool path optimization provides various advantages for CNC operations such as increased controllability of the cutting operation with the specified criteria, determination of all possible pareto optimal solutions, determination of all possible weights of each criteria, ease to observe and analyze the trade-off between each criteria (mostly each criteria conflicts with another), facility of limitation and minimization of each criteria and determination of the corresponding tool path for each solution

Since the problem is now has three objectives, the problem is redefined as passing over all the CL points determined on the 2D uniform grid of the part surface with the specified criteria such as limitation or minimization of the mean cutting forces, mean scallop height and total cycle time.

For the solution path to the problem, firstly CL and CC points should be determined using collision detection based algorithm with a user defined sensitivity (CC points is used for scallop height determination in multi-criteria optimization). Next step is the prediction of the slot cutting forces and scallop heights for each connection from CL points to its neighbors. Thanks to the predicted forces and scallop heights by using mechanistic force model and force mapping and proposed 3D scallop model, force map and scallop map is constructed which represents all possible movement with a specific reference force and scallop height value. 3D scallop model is validated by comparing predicted scallop distribution on the surface with the CAM output of UG NX6 for the same surface. The last step is implementation of the multi-criteria optimization algorithm with the specified criteria including threshold or minimization of the objectives (force, scallop height, cycle time). Since the objectives are conflicting in most cases, user needs to define the criteria for the optimization such as limiting two objectives below a threshold value and minimizing the third objective. The solution path is demonstrated in the Figure 4.1.

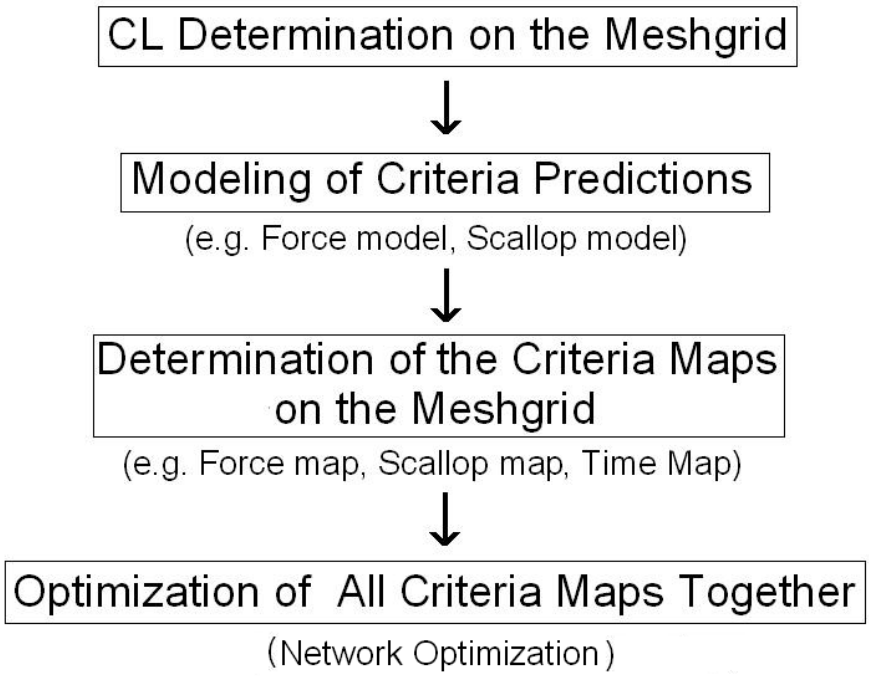

Figure 4.1 Solution path for multi-criteria tool path optimization

4.2. 2D & 3D SCALLOP MODEL

In literature, mostly 2D scallop models are discussed since mostly parallel and continuous tool paths are selected as in Figure 4.2, and therefore the scallop could be modeled in 2D via the cross-section of the part surface for two adjacent CL points along the tool path.

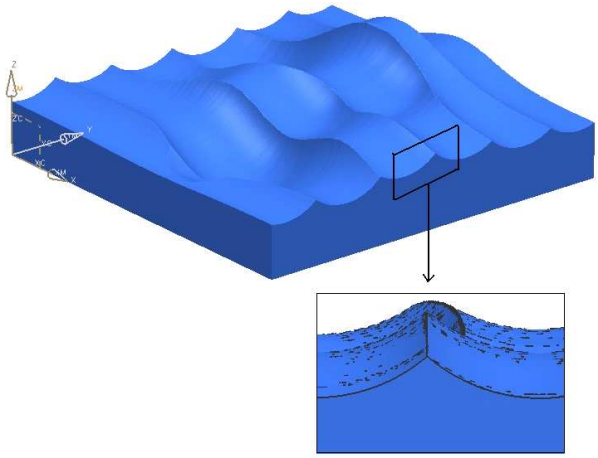

Figure 4.2 Cut surface for a standard zig zag tool path and the zoomed view of a section

The scallop is modeled with the representation of the intersection of two circles and the curve of the surface cross-section at that level as shown in Figure 4.3 below [31]. The calculation differs if the surface section between two cutter contact (CC) points is flat, convex or concave.

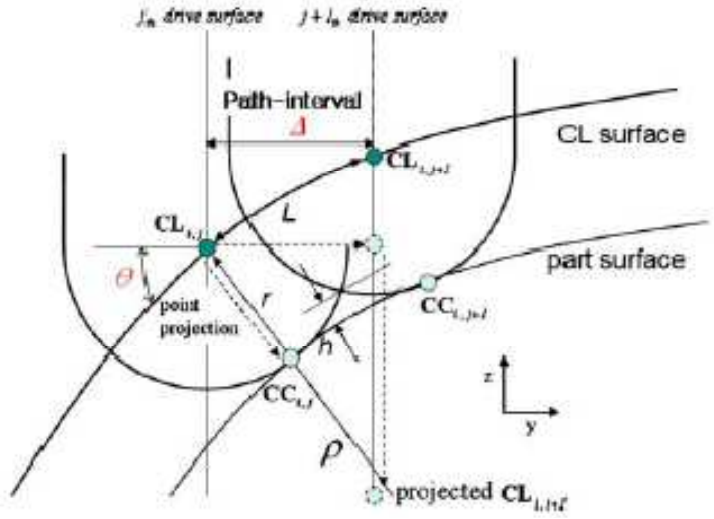

Figure 4.3 2D scallop model and illustration

$$\Delta = 2\cos\theta\sqrt{2rh} \quad \rightarrow \quad h = \frac{\Delta^2}{8r\cos^2\theta} \qquad \text{: flat}$$

$$\Delta = \cos\theta\sqrt{\frac{8rh\rho}{r+\rho}}\frac{r+\rho}{\rho} \quad \rightarrow \quad h = \frac{\Delta^2}{8r\cos^2\theta}\frac{\rho}{r+\rho} \qquad \text{: convex}$$

$$\Delta = \cos\theta\sqrt{\frac{8rh\rho}{r-\rho}}\frac{r-\rho}{\rho} \quad \rightarrow \quad h = \frac{\Delta^2}{8r\cos^2\theta}\frac{\rho}{r-\rho} \qquad \text{: concave}$$

where Δ is the tool path interval, h is the scallop height, ρ is the radius of curvature, r is the tool radius and θ the angle between the horizontal plane and the part surface.

θ and ρ could be calculated as follows:

$$\theta_{i,j} = \tan^{-1}\left(\frac{z_{i+1,j} - z_{i-1,j}}{2\Delta}\right)$$

$$\rho_{i,j} = \frac{2z_{i+1,j} - (z_{i-1,j} + z_{i+1,j})}{\Delta^2})$$

However, for numerous path segments the case is different, since the evolved scallop could not be represented in two 2D always. In Figure 4.4, a piece of a part surface enclosed by 4 CL points is shown. Assume each CL is visited in different path segments and the edges of this section are not cut.

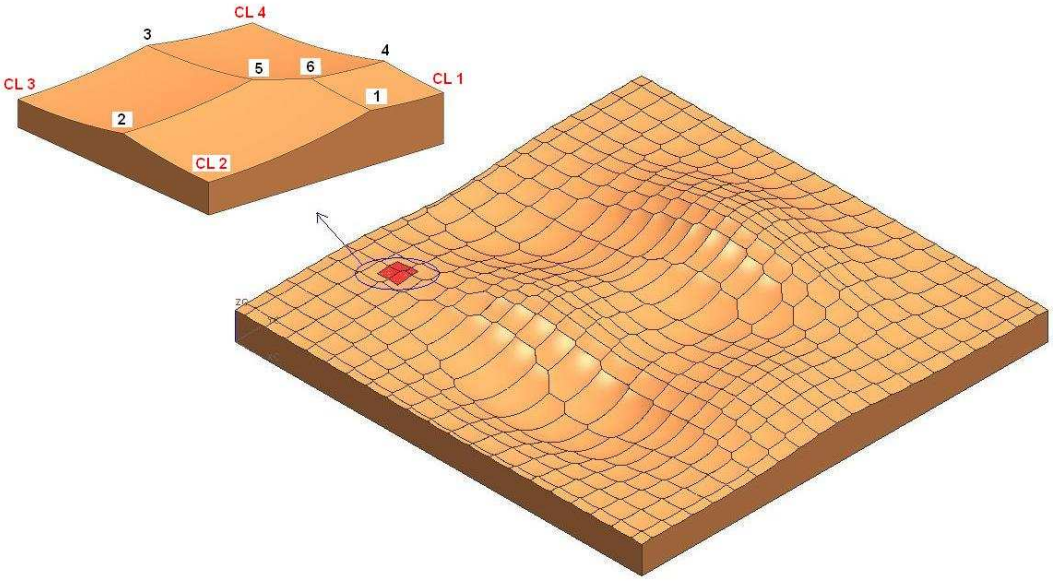

Figure 4.4 Reference cut surface for scallop height map and a zoomed section

So, there are six scallops in this section of the part surface where scallops 1-4 evolved from the intersection of two sphere surfaces and could be represented with the 2D model described above. However, scallops 5 and 6 evolved from the intersection of three sphere surfaces. Three sphere surfaces could possibly intersect in zero, one or two points, but if the $\frac{\text{step size}}{\text{radius}}$ ratio is smaller than $\sqrt{2}$ (2mm/6mm ≈ 0.33 in our case); they intersect in two points where one of them lies on the top hemisphere which actually stays in the tool volume. So, a single intersection point should be determined which lies on the bottom hemisphere surfaces. Furthermore, there are four possible selections of three spheres for the intersection from the group of four spheres and therefore four possible intersection points lying on the bottom hemisphere surfaces. However, every time only two of them evolve since the other two stay in the volume of the fourth sphere and therefore do not evolve. Furthermore, for the case of equal height CL points, the scallops 5 and 6 unite to a single point.

The intersection of three sphere surfaces could be calculated with the given centers and radii of the three spheres. A mathematical derivation for the solution can be found by taking the formulae for three spheres and setting them equal to each other. To simplify the calculations, three constraints are applied to the centers of these spheres; all three spheres are assumed to be centered on the z = 0 plane, one is at the origin, and one other is on the x-axis. It is possible to transform any set of three points to comply with these constraints, find the solution point, and then reverse the translation to find the solution point in the original coordinate system.

It is started with the equations for the three spheres:

$$r_1^2 = x^2 + y^2 + z^2$$

$$r_2^2 = (x-d)^2 + y^2 + z^2$$

$$r_3^2 = (x-i)^2 + (y-j)^2 + z^2$$

A point is needed to be estimated which is located at (x, y, z) that satisfies all three equations. First the second equation is subtracted from the first and solve for x:

$$x = \frac{r_1^{\,2} + r_2^{\,2} + d^2}{2d}$$

It is assumed that the first two spheres intersect in more than one point, that is that d-r1 < r2 < d+r1. In this case substituting the equation for x back into the equation for the first sphere produces the equation for a circle, the solution to the intersection of the first two spheres:

$$y^2 + z^2 = r_1^{\,2} - \frac{(r_1^{\,2} - r_2^{\,2} + d^2)^2}{4d^2}$$

Substituting $y^2 + z^2 = r_1^{\,2} - x^2$ into the formula for the third sphere and solving for y there results:

$$y^2 = \frac{r_1^{\,2} - r_3^{\,2} - x^2 + (x-i)^2 + j^2}{2j} = \frac{r_1^{\,2} - r_3^{\,2} + i^2 + j^2}{2j} - \frac{i}{j}x$$

Now that the x- and y-coordinates of the solution point are estimated, so the formula could be easily rearranged as below for the first sphere to find the z-coordinate:

$$z = \pm\sqrt{r_1^2 - x^2 - y^2}$$

Now the solution to all three points x, y and z are determined. Because z is expressed as the positive or negative square root, it is possible for there to be zero, one or two solutions to the problem.

After the scallop points in the section are calculated, the scallop heights for each have to be determined analytically. It is obtained at least two times finer CC grid of the surface than the CL point grid, so using the CC grid points in the section it is possible to represent the part surface for the section and for each scallop point it could be interpolated for a point on the part surface with the shortest distance to the scallop point. At that point, the surface gradient directs to the scallop point and therefore the scallop height equals to the distance between this point and the scallop point. An example of the modeled cut surface section including the scallops are depicted in the Figure 4.5 below where the curved edges are represented with straight lines for the ease of the geometric representation.

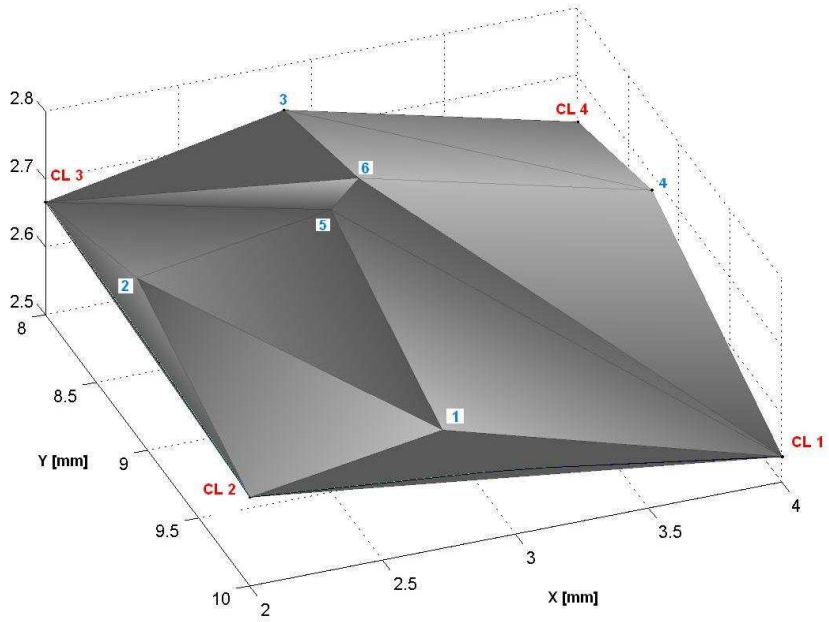

Figure 4.5 A predicted section of reference cut surface via 3D Scallop model

For the scallop optimization, a scallop map should be constructed which includes a scallop height representative for each neighborhood. However similar to the force map, any scallop modeled for the edge between two CL points is also affected from the tool path traveled until to this edge and that makes the scallop map dynamic. In other words, as in the case of the force map, the cut of further edges near an evolved

scallop reduce the height of the scallop. So, the modeled scallops for each neighborhood ignoring the cut of the edges near the CL points could be used as the representative scallop height for this neighborhood similar to force representatives obtained by slot cutting simulations. After that the static optimization could be performed where it is guaranteed that the actual scallops would be less than predicted scallops via the reducing effect of the cut edges.

The case of the cut CL points with all uncut edges (cut of CL points in z-direction only and remain the edges uncut as shown in Figure 4.4) represents the whole scallop map since all edges are uncut and scallops could be calculated exactly with the models described above. Further selection of the edges for the cut in the optimization tool would decrease the scallops predicted and modifies the scallop map, but the map is not updated in this study since a suitable dynamic optimization tool could not be determined in this study. Also the cut surface is plotted via the triangulation of the all obtained scallop and CL points in order to compare with the Figure 4.4 which is obtained with UG NX6 by subtracting the tool from the workpiece for each CL point. The modeled surface is shown in Figure 4.6, where all curved edges are represented with straight lines.

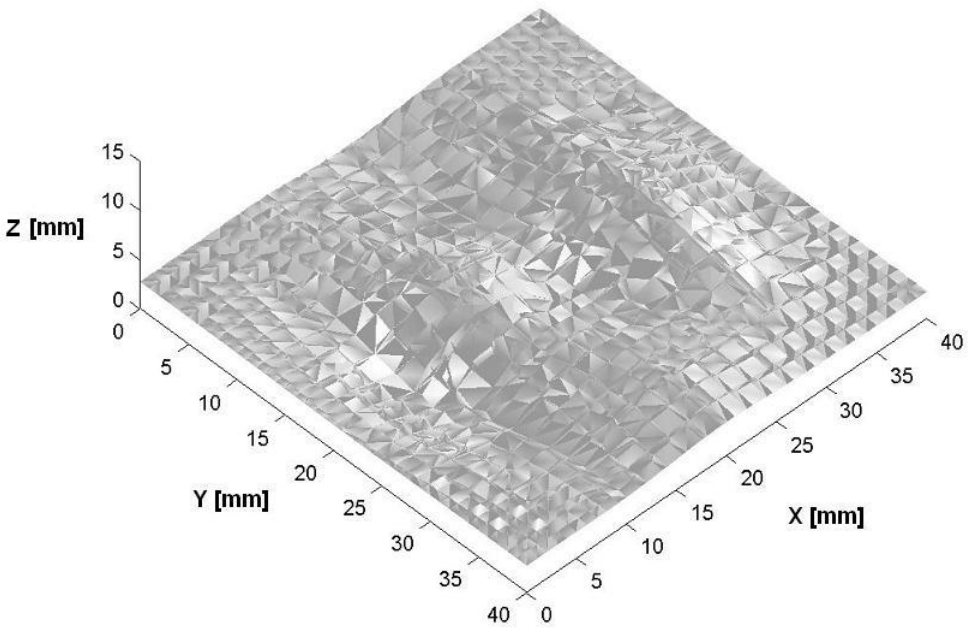

Figure 4.6 Illustration of the predicted reference cut surface

In Figure 4.7, the calculated scallop points are also plotted on the cut surface depicted in Figure 4.4 to visually validate the pattern of the predicted scallops; furthermore the errors are calculated from the distance between the cut surface exported from UG NX6 in STL format with 0.001 mm edge tolerance and the scallop points calculated with scallop models in 2D and 3D discussed above. In Figure 4.8, the error histogram of the scallops is shown. The errors are low and reasonable.

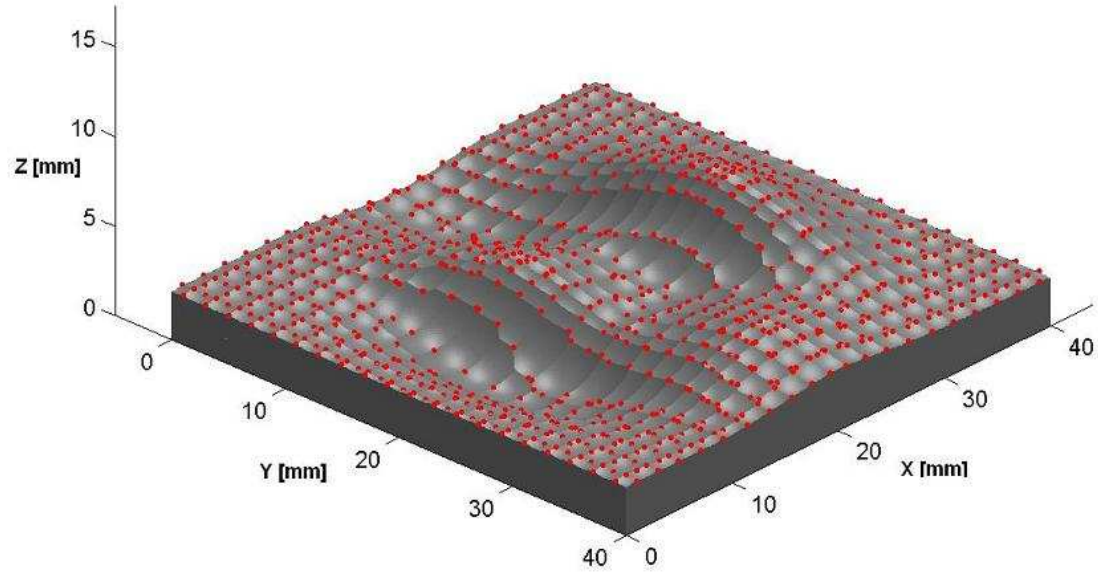

Figure 4.7 Illustration of predicted scallop points on the reference cut surface

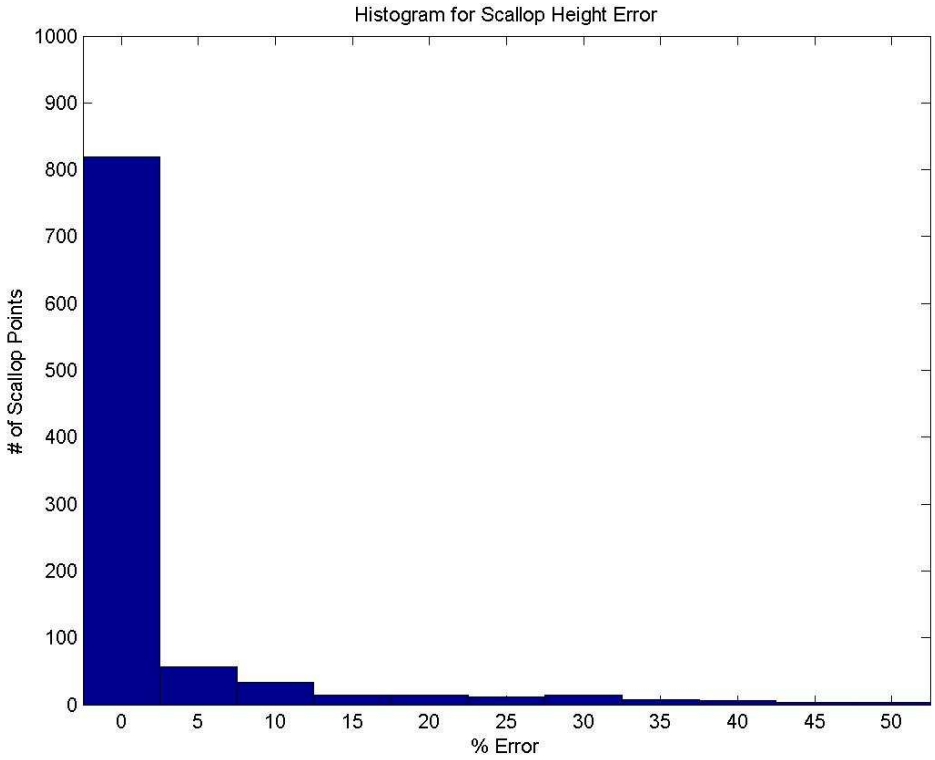

Figure 4.8 Error histogram of predicted scallop heights

4.3. Multi-Criteria Network Optimization

For single objective network problems such as tool path selection with minimized criteria, mostly minimum spanning tree (MST) or Minimum Cost Traveling Salesman (MCTS) are preferred since it can be solved efficiently. In this study, an MCC-based path optimization is introduced and used for single objective problem. However, multi-criteria optimization problem is not simply extended formulations of the single objective problem, since it could not be possible to get an optimal solution because multiple objectives usually conflict with each other in practice. So, firstly multi-criteria decision making should be well understood to understand how solutions of a multi-criteria problem could be defined.

4.3.1. Problem Description

Suppose a connected and directed graph G = (V, E), where V = {v_1, v_2, …., v_n} is a finite set of vertices representing the nodes of the part surface, and E = {e_1, e_2, …., e_m} is a finite set of edges representing connections between these nodes. Each edge has p associated real numbers representing p attributes defined on it (e.g. force, cycle

time, scallop height for the edge) and denoted with $w_i = (w_{1i}, w_{2i}, \ldots, w_{pi})$ (i = 1, 2, …., m). In practice w_{ki} (k = 1, 2, …, p) may represent the attribute value.

Define $x = (x_1, x_2, \ldots, x_m)$ as follows:

$$x_i = \begin{cases} 1 & \textit{if edge } e_i \textit{ selected} \\ 0 & \textit{otherwise} \end{cases}$$

Then a MCC of the graph G can be expressed as the vector x. Let X be the set of all such vectors corresponding to the spanning trees in graph G, the MCC problem can be formulated as follows:

$$\min z_1(x) = \sum_{i=1}^{m} w_{1i} x_i$$

$$\min z_2(x) = \sum_{i=1}^{m} w_{2i} x_i$$

...

$$\min z_p(x) = \sum_{i=1}^{m} w_{pi} x_i$$

where $x \in X$ *and* z_i is the *i*th objective to be minimized for the problem.

So, compared with the traditional problem, the problem only differs in the number of objectives. Because these multiple objectives usually conflict with each other, it can not be determined which edge have the least weight and span one b one to form MCC.

4.3.2. Multiple Criteria Decision Making

Definition 1: Given a set of feasible solution $S = \{x \mid x \in X\}$, solution x^* is denoted as the dominating solution for the problem if and only if all other solutions $x \in S$, the following conditions hold:

$$z_k(x) \geq z_k(x^*), \quad k = 1, 2, \ldots, p$$

Definition 2: As to the problem, the point $z^0(x) = (z_1^0(x), z_2^0(x), \ldots, z_p^0(x))$ in criteria space is denoted as the ideal point, where

$$z_k^0(x) = \min_{x \in X} z_k(x), \quad k = 1, 2, \ldots, p.$$

In the MST with single objective, the ideal point is the dominating solution or optimal solution. But in the mc-MST problem, actually the ideal point does not exist mostly because mostly objectives are conflicting and each objective cost in the ideal point could only be achieved on the objective space at a solution point where it is budged from other objective costs. For the multi-criteria problem, usually the concept of non-dominated solution or Pareto optimal solution is adopted to define its solution.

Definition 3: Given a set of feasible solutions S = {x | x∈ X}, solution x' is denoted as the non-dominated solution or Pareto optimal solution for the problem if and only if there is no other solution x ∈ S, satisfying the following conditions:

$$z_q(x) < z_q(x'), \qquad \text{for some } q \in \{1,2,....,p\},$$
$$z_k(x) \le z_k(x'), \qquad \text{for all } k \neq q,\ k = 1,2,....,p.$$

So, usually multi-criteria problem has a set of Pareto optimal solutions which can form a Pareto frontier. So, the real solutions to multi-criteria optimization problem are a set of Pareto optimal solutions. For a two-criterion problem the objective space which consists all possible solutions forms an enclosed area and pareto front is formed as a discrete curve on the boundary of these region near the ideal point. In the Figure 4.9 below, objective space, ideal point and pareto front of a two-criterion problem is demonstrated. Hence, for a three-criterion problem, the objective space should form an enclosed volume where pareto front would be a discrete surface on the boundary of the objective space volume close to the ideal point.

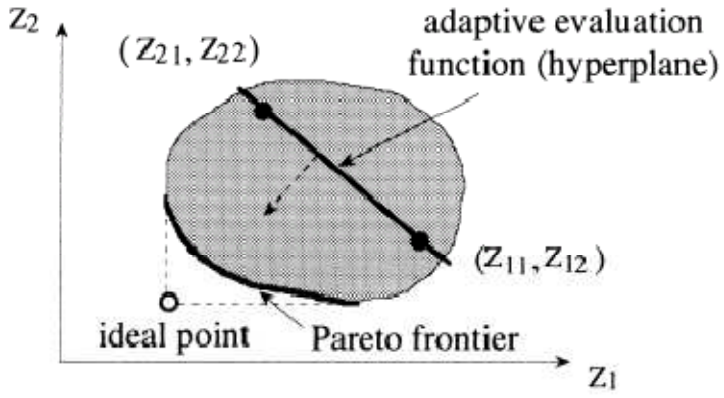

Figure 4.9 Illustration of ideal point, pareto surface and objective space

4.3.3. Optimization Routine

To solve multi-criteria optimization problem, evolutionary algorithm is suitable since it specialize in solving multi-objective problems, especially the problems with competing criteria are best solved by genetic algorithm than any other method of solution known. The ability of evolutionary algorithms especially genetic algorithm to explore many points in the search space has been a powerful tool for multi-objective optimization problems. Another alternative method is objective weighting which is easier and faster to implement, however it could not provide solutions for objectives which could not be valued for the edges. For instance, force, time or scallop height for each edge move could be modeled and represented with a value, which could be further used in objective weighting. However, some objective, especially conditional ones are hard to be modeled analytically and added to each edge. For instance: an objective which requests to have at most 20 rapid runs, in other words 21 discrete tool path segments, or an objective which requests to cut at least 60% of the edges and guarantee to not excess a specific force value. For these cases, genetic algorithm is easily applicable where the objective evaluation is encoded to the chromosome. For this study, two multi-criteria optimization routine is introduced: both genetic algorithm (GA) based optimization which uses non-domination sort to determine the pareto frontier; and the single-objective optimization using varying objective weighting.

4.3.3.1 GA Approach with Non-Domination Sort

Encoding & Decoding

For the GA optimization, the solution trials which are actually different spanning trees should be encoded as parent chromosomes, and after each generation the population should be decoded back to spanning trees in order to evaluate the objective costs. Here, the encoding of the solution trials to form chromosomes is critical, since the convergence interval of the optimization depends highly to the heritability of the encoding. For instance, low heritability causes similar parent chromosomes to generate strange children which not resemble to the parents; this is against the nature of the evolutionary approach and increases randomness, so the

convergence will take more time. There are several encoding techniques to be used for spanning trees. One of them is Prufer number consists of n-3 genes where n is number of the nodes and n-1 number of the selected edges of $x = (x_1, x2, \ldots, x_m)$. This is a simple encoding since it has not much genes, however it has low heritability as investigated as below:

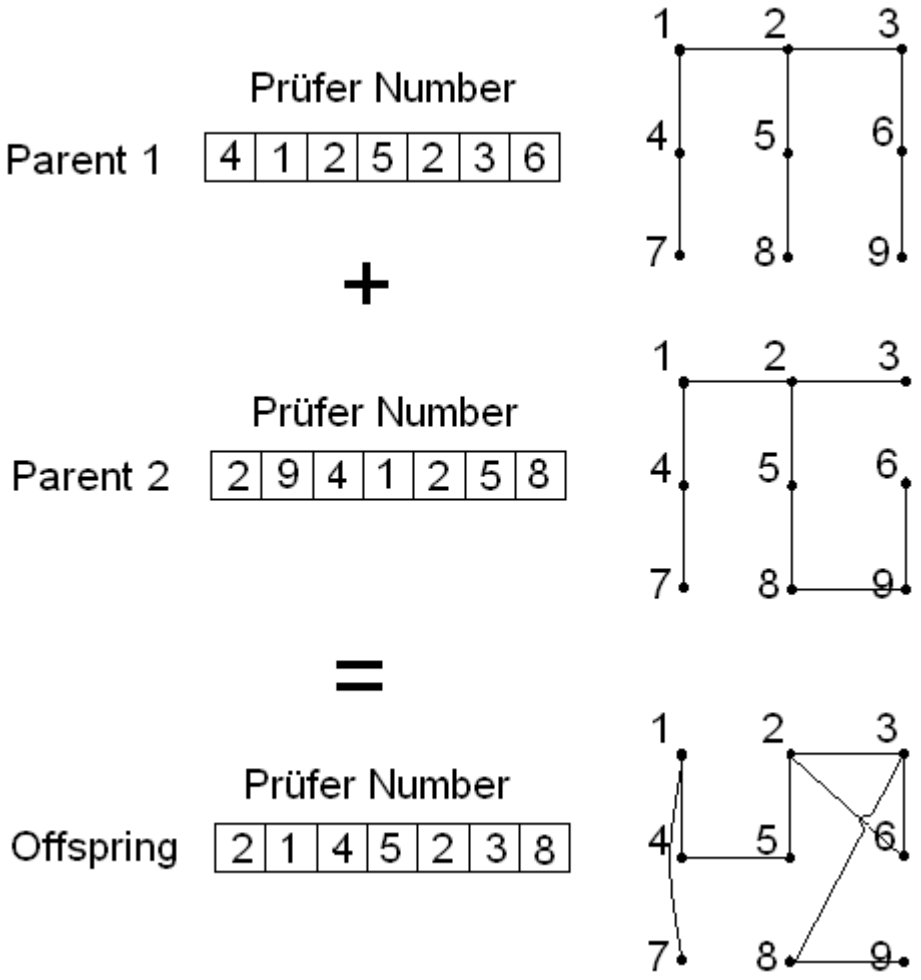

Another encoding technique which has high heritability is weighted coding, where a chromosome consists of m genes where m is number of the all possible edges of $E = \{e_1, e2, \ldots, e_m\}$ and each gene takes a value between 0 and 1 to determine the weight of the edge for the possibility to be selected in the spanning tree solution $x = (x_1, x2, \ldots, x_m)$.

For an n-noded graph, number of possible edges is $8n^2 - 52n + 4$. So, this encoding will cause a longer generation time than Prufer number; however converges faster since the genes are heritable. Even though computation is longer, weighted coding is preferred in the GA optimization routine due to the higher heritability.

Crossover & Mutation

For crossover, a random mask with length of the parent chromosomes is formed from 0s and 1s for the selection of genes from the parents. According to this mask, the genes of the parents are selected for the offspring as shown in Figure 4.10 below.

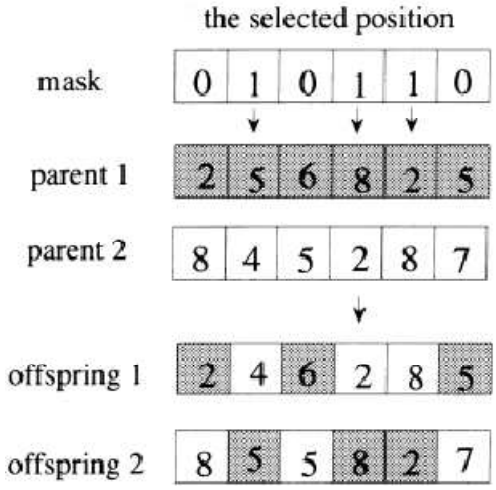

Figure 4.10 Illustration of crossover

For mutation, one of the genes on the chromosome is selected and replaced with a random possible value. Crossover and mutation probabilities are determined by the decision maker in the optimization routine.

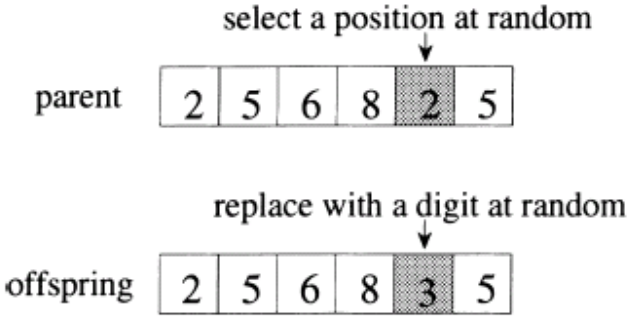

Figure 4.11 Illustration of mutation

Non-Domination Sort

Before the selection is performed in nondominated sorting, the population is ranked on the basis of an individual's nondomination. The nondominated individuals present in the population are first identified from the current population. Then all these individuals are assumed to constitute the first nondominated front in the population

and assigned a large dummy fitness value. The same fitness value is assigned to give an equal reproductive potential to all these nondominated individuals. To maintain diversity in the population, these classified individuals are then shared [10] with their dummy fitness values. Sharing is achieved by performing selection operation using degraded fitness values that are obtained by dividing the original fitness value of an individual by a quantity proportional to the number of individuals around it. This causes multiple Pareto optimal points to co-exist in the population.

After sharing, these nondominated individuals are ignored temporarily to process the rest of the population in the same way to identify individuals for the second nondominated front. These nondominated points are then assigned a new dummy fitness value that is kept smaller than the minimum shared dummy fitness of the previous front. This process is continued until the entire population is classified into several fronts. The population is then reproduced according to the dummy fitness values.

Procedure:

Step 1: Determine all nondominated individuals P_c from the current population, and assign a large dummy fitness value to them.

Step 2: Calculate each individual's niche count m_j:

$$m_j = \sum_{k \in P_c} sh(d_{jk})$$

$$where \quad sh(d_{jk}) = \begin{cases} 1 - \left(\dfrac{d_{jk}}{\sigma_{share}} \right)^2 & if \quad d_{jk} < \sigma_{share} \\ 0 & otherwise \end{cases}$$

and d_{jk} is the phenotypic distance between two individual j and k in the current nondominated solution set and σ_{share} is the maximum phenotypic distance allowed between any two individuals to become members of a niche.

Step 3: Calculate the shared fitness value of each individual by dividing its dummy fitness value by its niche count.

Step 4: Ignore all sorted nondominated individuals, go to step 1 and continue the process until the entire population is all sorted.

As to the selection, only the roulette wheel selection is adopted. Because the other dummy fitness value for the following sorted nondominated individuals is just kept smaller than the minimum shared dummy fitness of the previous nondominated set, the individuals in the first nondominated set have more chance to be selected in the next generation than those in the rest of nondominated set. This is intended to search for the whole nondominated regions or Pareto optimal frontier.

Validation of Multi Criteria GA Algorithm

Hypothetical maps of 3 x 3 vertices below are created to represent the distribution of two objective functions between each vertex. The function value of 10000 for a vertex pair index ij indicates that vertex i and j are not neighbors and so it is not possible to select a path from i to j.

Table 4.1 Objective map #1

	1	2	3	4	5	6	7	8	9
1	10000	7.4239	10000	7.2637	5.8294	10000	10000	10000	10000
2	7.4239	10000	5.6489	4.0223	4.1966	6.6004	10000	10000	10000
3	10000	5.6489	10000	10000	6.2107	4.7952	10000	10000	10000
4	7.2637	4.0223	10000	10000	6.9335	10000	4.0395	7.0147	10000
5	5.8294	4.1966	6.2107	6.9335	10000	7.6798	5.471	6.9251	7.6192
6	10000	6.6004	4.7952	10000	7.6798	10000	10000	6.5272	6.1951
7	10000	10000	10000	4.0395	5.471	10000	10000	5.3408	10000
8	10000	10000	10000	7.0147	6.9251	6.5272	5.3408	10000	5.5676
9	10000	10000	10000	10000	7.6192	6.1951	10000	5.5676	10000

Table 4.2 Objective map #2

	1	2	3	4	5	6	7	8	9
1	10000	71.123	10000	74.512	73.038	10000	10000	10000	10000
2	71.123	10000	72.534	95.08	64.87	84.659	10000	10000	10000
3	10000	72.534	10000	10000	99.149	70.004	10000	10000	10000
4	74.512	95.08	10000	10000	81.26	10000	68.794	70.993	10000
5	73.038	64.87	99.149	81.26	10000	89.694	92.236	81.04	59.695
6	10000	84.659	70.004	10000	89.694	10000	10000	78.46	61.721
7	10000	10000	10000	68.794	92.236	10000	10000	96.579	10000
8	10000	10000	10000	70.993	81.04	78.46	96.579	10000	82.777
9	10000	10000	10000	10000	59.695	61.721	10000	82.777	10000

Using these objective maps, two-criterion optimization is performed with multi-criteria GA approach. Obtained population of optimized solutions is plotted with objective points of numerous random selected paths for the 3 x 3 map as shown in Figure 4.12. As seen in the Figure 4.12, optimized solution points are non-dominated solutions and determine the pareto frontier of the objective space. In two-criterion problem, the objective space is 2D and encloses a specific area; and the pareto frontier becomes a curve at the boundary of the objective space.

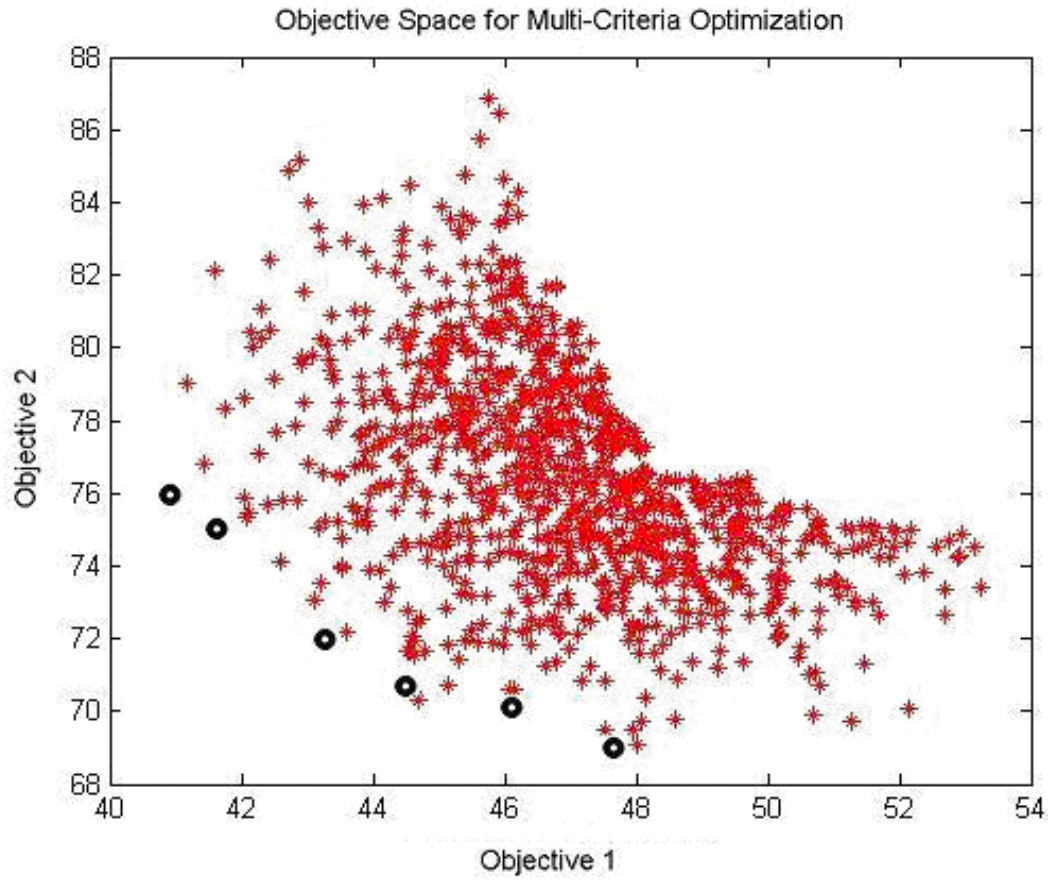

Figure 4.12 Predicted pareto points in the objective space

4.3.3.2 Varying Objective Weighting Algorithm

A common solution to the problem is to simplify multiple objectives into a single objective because network optimization algorithms such as MST or MCTS are only effective with single objective by using objective weighting method. But only one single-point solution in the sense Pareto optimality can be obtained. However, the decision maker in practice may prefer one Pareto optimal point over the others on the

situation. So, it is useful to calculate all possible Pareto optimal solutions, and the optimization routine should be repeated by changing objective weighting several times.

Optimizing each objective seperately:

$$\min z_1(x) = \sum_{i=1}^{m} w_{1i} x_i$$

$$\min z_2(x) = \sum_{i=1}^{m} w_{2i} x_i$$

...

$$\min z_p(x) = \sum_{i=1}^{m} w_{pi} x_i$$

There are respectively p optimal solutions x^k , each for one single objective; and p optimal cost values for the objectives, one of each solution minimizes a single objective, each of them lies on the pareto frontier. However, each of them conflicts with another, each cost value should be evaluated with a weighting to determine a total cost value, which means that how much the user desire to get close to the optimal cost of each objective. The total cost function could be written as below:

$$\min z(x) = \sum_{k=1}^{p} \lambda_k z_k(x) \quad where \ x \in X$$

If each optimal solution in equation is put into the total cost equation:

$$\min z(x) = \sum_{k=1}^{p} \lambda_k \sum_{i=1}^{m} w_{ki} x_i = \sum_{k=1}^{p} \sum_{i=1}^{m} (\lambda_k w_{ki}) x_i \ \ where \ x \in X$$

So, it is concluded that weighting of single optimal cost of each objective could be maintained by weighting w_{ki} , the cost values of each objective at each edge, with λ_k , the corresponding weighting value for the objective.

Validation of Objectıve Weigthing Algorithm

Hypothetical maps of 3 x 3 vertices below are created to represent the distribution of two objective functions between each vertex. The function value of 10000 for a vertex pair index ij indicates that vertex i and j are not neighbors and so it is not possible to select a path from i to j.

Table 4.3 Objective map #1

	1	2	3	4	5	6	7	8	9
1	10000	85.766	10000	89.296	86.393	10000	10000	10000	10000
2	80.539	10000	63.485	74.946	98.143	59.247	10000	10000	10000
3	10000	52.076	10000	10000	56.707	84.172	10000	10000	10000
4	64.077	81.135	10000	10000	58.088	10000	66.307	61.408	10000
5	82.476	79.111	63.406	90.747	10000	93.635	98.732	97.535	82.427
6	10000	50.59	95.444	10000	95.016	10000	10000	75.265	88.507
7	10000	10000	10000	93.33	56.631	10000	10000	82.974	10000
8	10000	10000	10000	59.055	64.187	74.385	52.284	10000	88.952
9	10000	10000	10000	10000	64.676	92.685	10000	93.844	10000

Table 4.4 Objective map #2

	1	2	3	4	5	6	7	8	9
1	10000	5.2979	10000	4.1654	5.9453	10000	10000	10000	10000
2	5.2979	10000	4.4711	4.8039	6.9516	4.9157	10000	10000	10000
3	10000	4.4711	10000	10000	4.7068	4.5223	10000	10000	10000
4	4.1654	4.8039	10000	10000	7.1285	10000	7.0089	5.4116	10000
5	5.9453	6.9516	4.7068	7.1285	10000	5.3423	7.0113	6.5423	5.3699
6	10000	4.9157	4.5223	10000	5.3423	10000	10000	5.5649	7.9023
7	10000	10000	10000	7.0089	7.0113	10000	10000	6.9978	10000
8	10000	10000	10000	5.4116	6.5423	5.5649	6.9978	10000	6.6986
9	10000	10000	10000	10000	5.3699	7.9023	10000	6.6986	10000

Using these objective maps, two-criterion optimization is performed with varying objective weighting approach. Obtained population of optimized solutions is plotted with objective points of numerous random selected paths for the 3 x 3 map as shown in Figure 4.13. As seen in the figure, optimized solution points are non-dominated solutions and determine the pareto frontier of the objective space. In two-criterion problem, the objective space is 2D and encloses a specific area; and the pareto frontier becomes a curve at the boundary of the objective space.

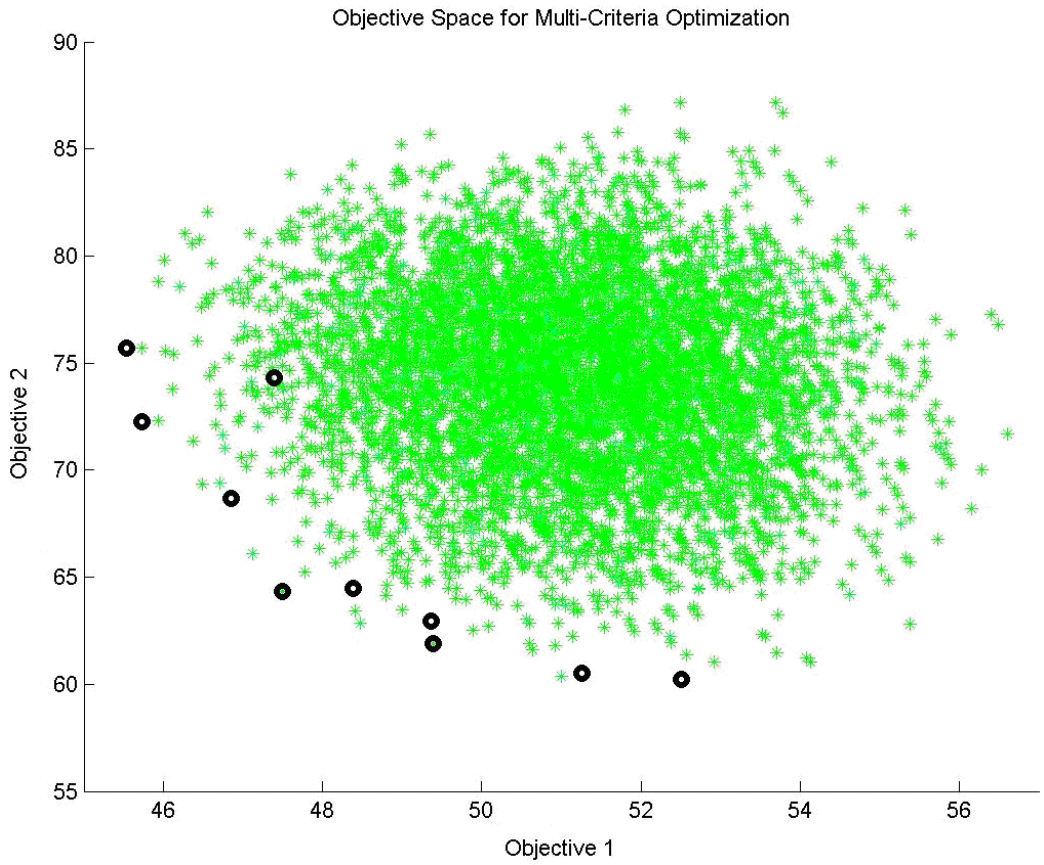

Figure 4.13 Predicted pareto points in the objective space

4.3.4 Discussion

Both GA approach and varying objective weighting methods determines successfully the nondominated solutions of the optimization problems; however varying objective weighting method supersedes GA approach when compared the computation times. Computation of GA approach directly depends on the number of the genes of a chromosome which is determined according to the both the number of vertices in the network and the encoding method used to represent the chromosome.

With Prufer number encoding, number of genes in the chromosome is equal to n-2, where n is the number of vertices in the network; however Prüfer number encoding has a low heritability which also increases the convergence time for the optimization. On the other hand, for …. encoding, the heritability is high and convergence is better where each gene in a chromosome represents the encoded weighting of possibility of a specific edge to occur in the tool path. In that sense, the number of genes equals to the number of all possible edges in the mesh. For an n x n

mesh, number of genes equals $8n^2$-12n + 4; so when the number of vertices increases linearly, the number of genes and therefore computation time increase quadratically.

On the other hand, computation time of varying objective weighting equals to the multiplication of computation time of preferred single-objective optimization routine for a weighted objective and the number of user defined objective points on the pareto front obtained by changing the weightings of the objectives. In that sense, using a fast MST algorithm and varying the weightings of the objectives from 0% to 100% with a reasonable incremental percentage would result much faster computation for the non dominated solutions. In order to increase compatibility of GA approach, encoding method could be changed in order to increase the heritability or to decrease the number of genes to represent individual solutions as chromosomes.

4.4. Cutting Force-Cycle Time-Scallop Height Optimization Using Varying Objective Weighting Approach

4.4.1. Investigation of the Physical Relations between cutting force, cycle time and scallop height

To implement the multi-criteria tool path optimization algorithm for free form surface machining, varying objective weighting approach is preferred where objectives are mean cutting force, mean scallop height and total cycle time. In order to investigate the physical relations of the objectives for multi-criteria free form surface tool path optimization, a hypothetical force, scallop height and cycle time map is selected and numerous tool path solutions are optimized using varying objective weighting with 1% sensitivity where weights of each criterion (mean cutting force, mean scallop height, total cycle time) changed from 0% to 100%. After that, all obtained nondominated solutions are plotted to obtain the pareto surface as shown in Figure 4.14. On the black curve, weight of mean scallop height minimization (wS) is 0%. In other words, scallop height is not included into the optimization. Also on the arrow direction on the black curve, weight of mean cutting force minimization (wF) is increasing from 0% to 100% where weight of total cycle time minimization (wT) is decreasing from 100% to 0%. Similar explanations could be easily made for the red and blue curves when observing the figure. When the figure is observed, it could also be realized that the objectives are conflicting in most

regions as expected where minimizing one of the objective values, other objective values tend to increase. So, there could be determined several criteria by the user for multi-criteria tool path optimization.

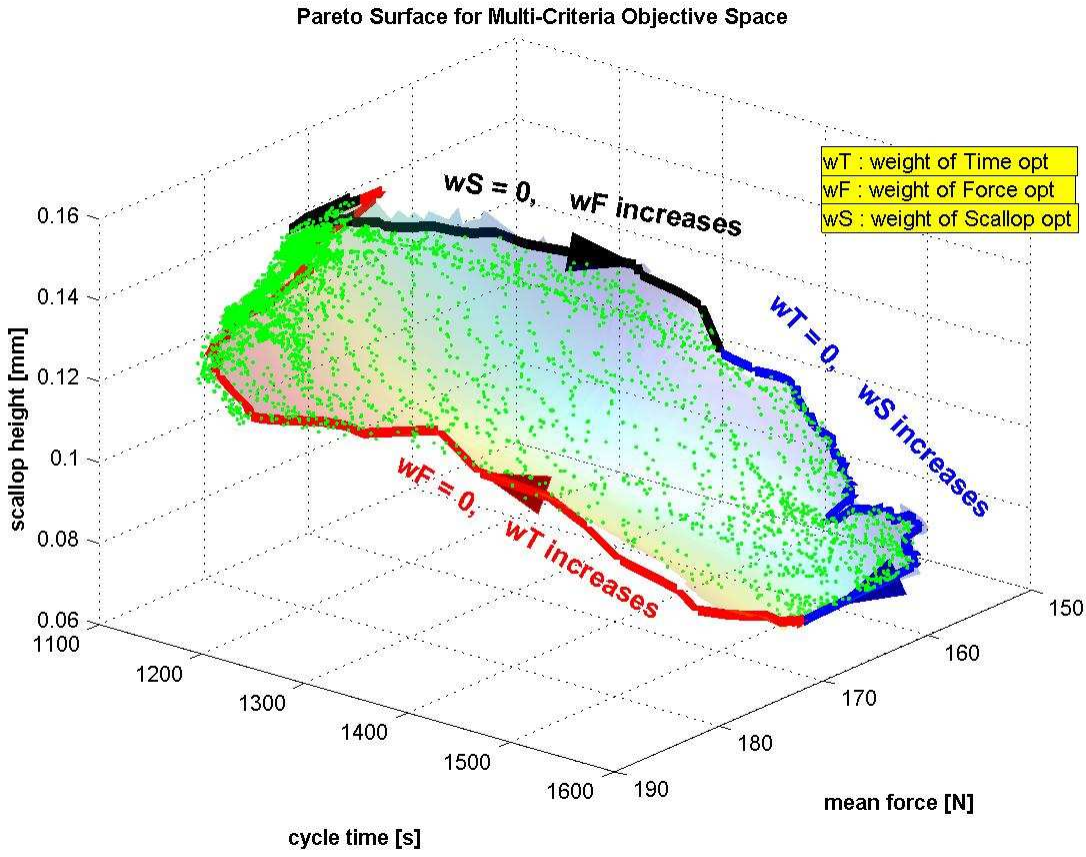

Figure 4.14 Pareto surface for hypothetical criteria maps

When the pareto surface is investigated, it is recognized that there are accumulation of solutions on the top and the bottom regions. The top region is the solutions with lowest total cycle time which could be achieved by escaping from diagonal edges since they have longer distance to travel. Since diagonal edges have longer distance to travel and higher scallop heights to remove, so preferring diagonal edges increases both cycle time and cutting force, but decreasing the mean of the remained scallop height. So, the bottom region contains tool path solutions with mostly diagonal edges, where total cycle times are high, but mean scallop heights and mean cutting forces are low.

4.4.2. Validation Tests for Multi-Criteria Free Form Surface Tool Path Optimization

For validation tests, three different free form surfaces are selected and two different criterions are implemented for each surface. First optimization criterion is selecting all objective weights equal (wF = wT = wS ≈ 33%). Second optimization criterion includes two maximum threshold values for two objectives and one objective minimization (Mean Cutting Force < 260 N, Mean Scallop Height < 100 μm, Minimize Cycle Time).

So, totally 6 multi-criteria tool path optimizations are performed where estimated pareto surfaces, scallop model validations and experimental cutting force and cycle time validations are represented. All experiments were performed with spindle speed of 600 rpm and feedrate of 48 mm/min.

4.4.2.1 SAMPLE 1: Free Form Surface #1 (40 mm x 40 mm x 6 mm)

Free Form Surface #1 obtained from modified MATLAB's peak function with dimensions 40 mm x 40 mm x 6 mm is illustrated in Figure 4.15 where the equation of the surface is also explicitly shown.

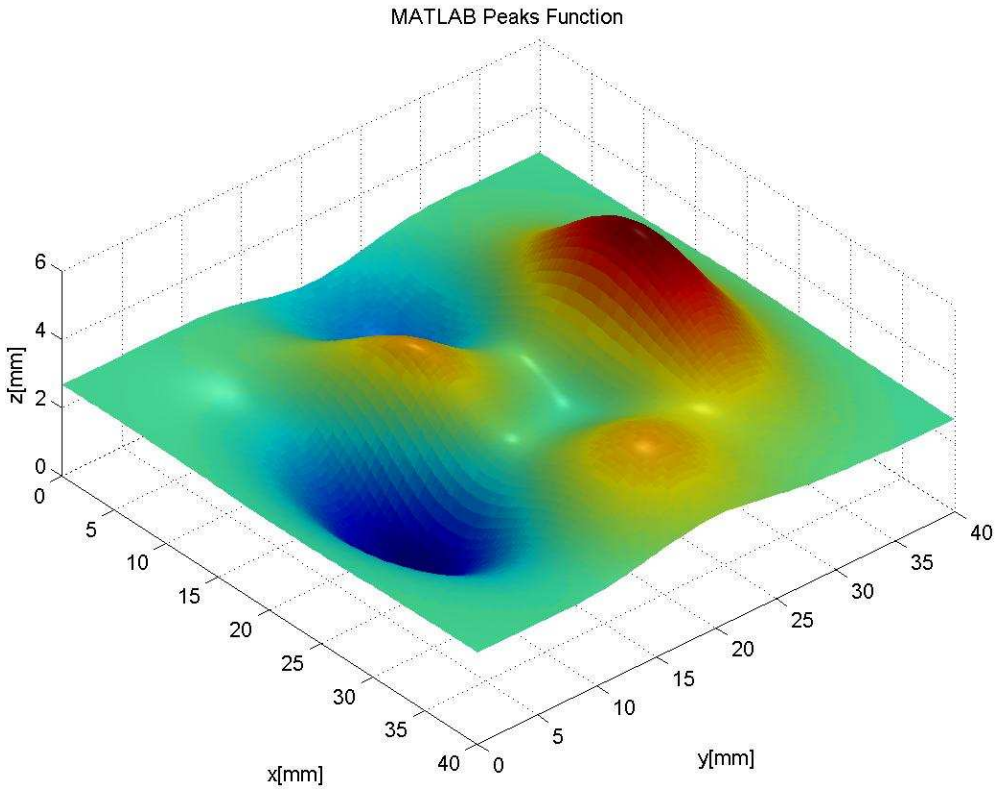

Figure 4.15 3D CAD model for sample 1

For the first step, the CL points are determined using the Collision detection based algorithm. The screen-shoot of the movie for CL determination routine is shown in Figure 4.16.

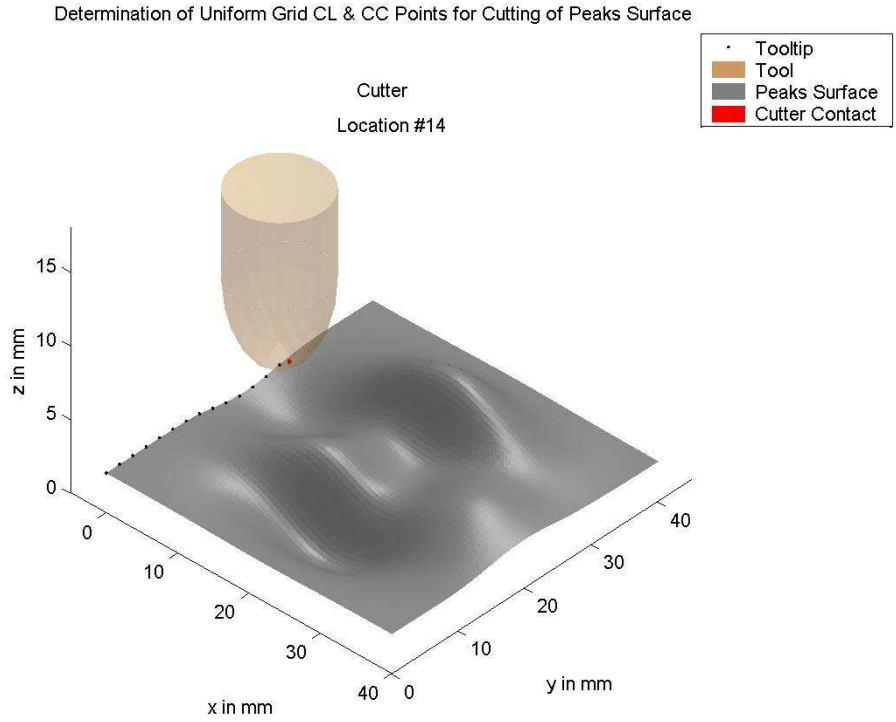

Figure 4.16 Screen shoot of CL point determination routine for sample 1

Then, the force, scallop and cycle time maps are obtained using the force and scallop height models. Cycle time map is easily obtained by calculating cycle times for each edge by division of the distance traveled between the relevant CL points to the constant feed rate of 48 mm/min. Analytically determined scallop points used to calculate scallop heights are plotted in Figure 4.17-a on the cut surface exported from UG NX6 to visually validate the pattern of the predicted scallops; furthermore the errors are calculated from the distance between the cut surface exported from UG NX6 in STL format with 0.001 mm edge tolerance and the scallop points analytically determined with scallop models in 2D and 3D. In Figure 4.17-b, the error histogram of the scallops is shown. The errors are low and reasonable.

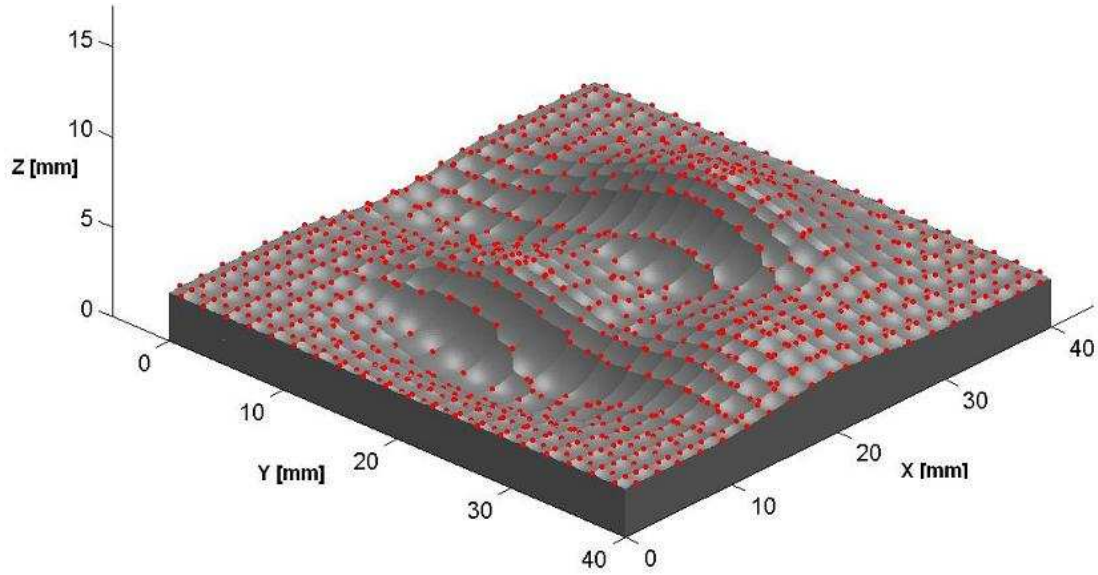

(a)

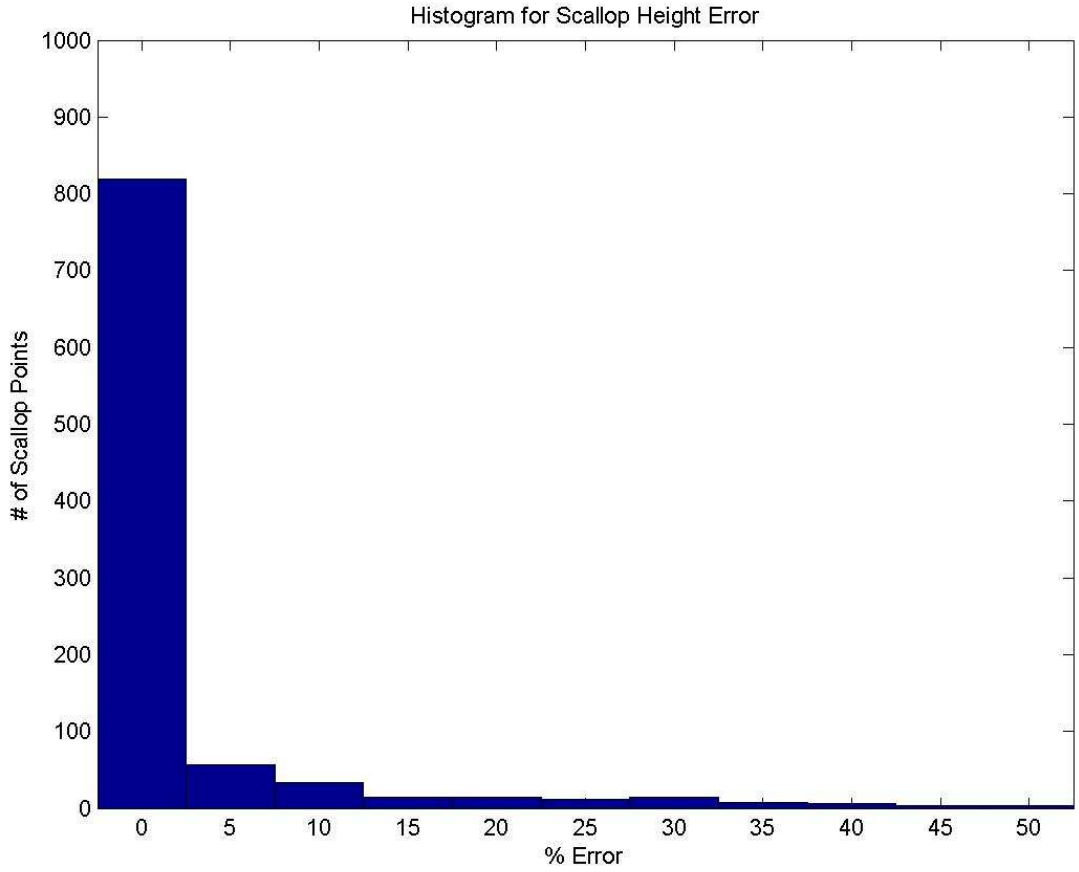

(b)

Figure 4.17 (a) Illustration of predicted scallop points on the reference cut surface

(b) Error histogram of predicted scallop heights

Optimization Criterion 1: wF = wT = wS ≈ 33%

Varying objective weighting algorithm is used with 1% sensitivity where weights of each criterion (mean cutting force, mean scallop height, total cycle time) changed from 0% to 100%. After that, all obtained nondominated solutions are plotted to obtain the pareto surface as shown in Figure 4.18 where also the single point of wF = wT = wS is depicted with pink point. Theoretically this nondominating solution point is the closest point to the ideal point of the objective space.

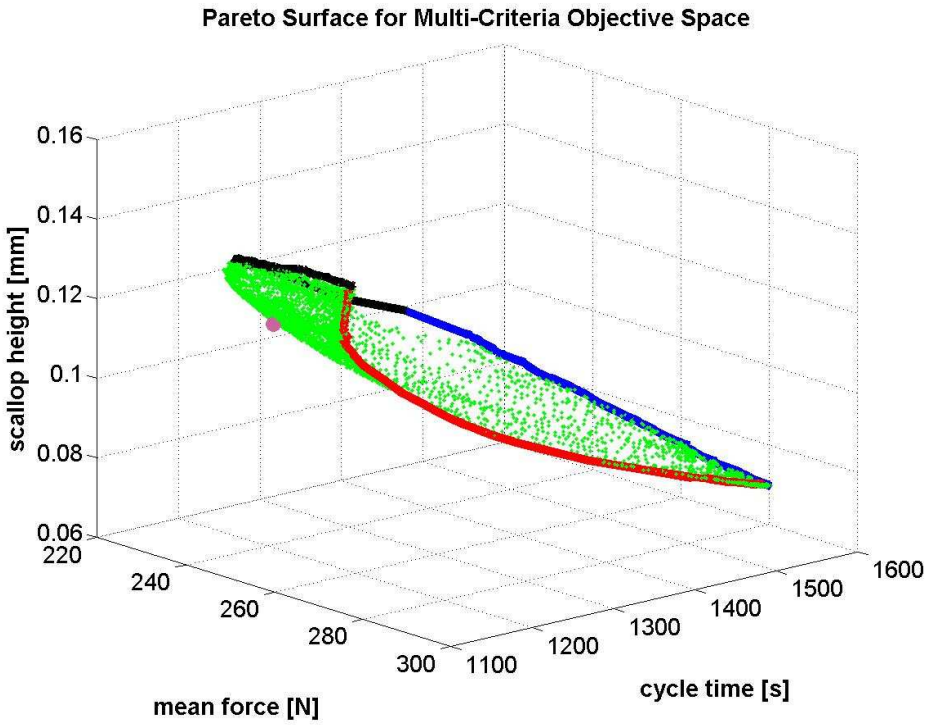

Figure 4.18 Pareto surface and solution point for optimization criterion 1 (sample 1)

All tool path solutions represented in pareto surface with their objective values are stored once the optimization routine is completed. So, for wF = wS = wT only the corresponding point is picked from the solutions. The objective costs of this point are 245 N, 1118 s and 125 μm.

The optimized tool path satisfying the criterion and represented with pink point in the pareto surface are shown in Figure 4.19 below.

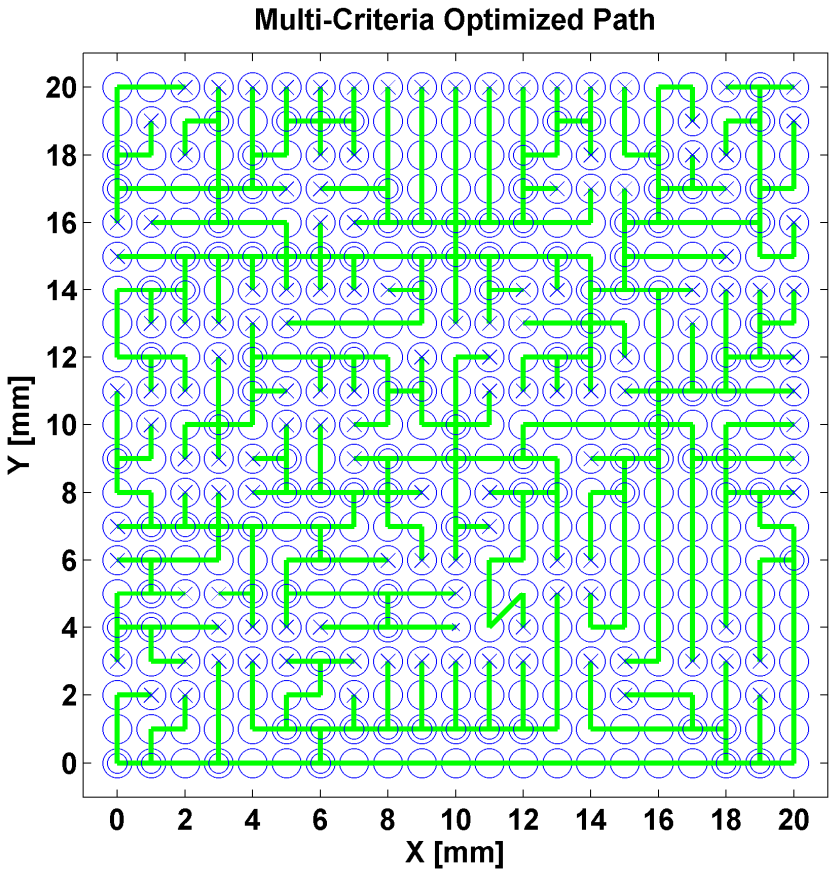

Figure 4.19 Tool path for optimization criterion 1 (sample 1)

As seen in the figure, there are no diagonal edges selected in the tool path, because the weight of total cycle time minimization is reasonably high (wT = 33%) and the optimization routine tends to escape from diagonal edges with a weighting of 33%.

In order to validate mean cutting force and total cycle time, the total cutting operation is firstly simulated and compared with the objective costs, then compared with the experimental cutting forces. Since the force map is formed using slot cutting simulations, it is expected that forces of the simulated tool path would remain below the graph obtained from the force map. In that sense, the simulated mean cutting force needs to be below the objective cost. Also, simulated cutting forces needs to match quite well with experimental cutting forces.

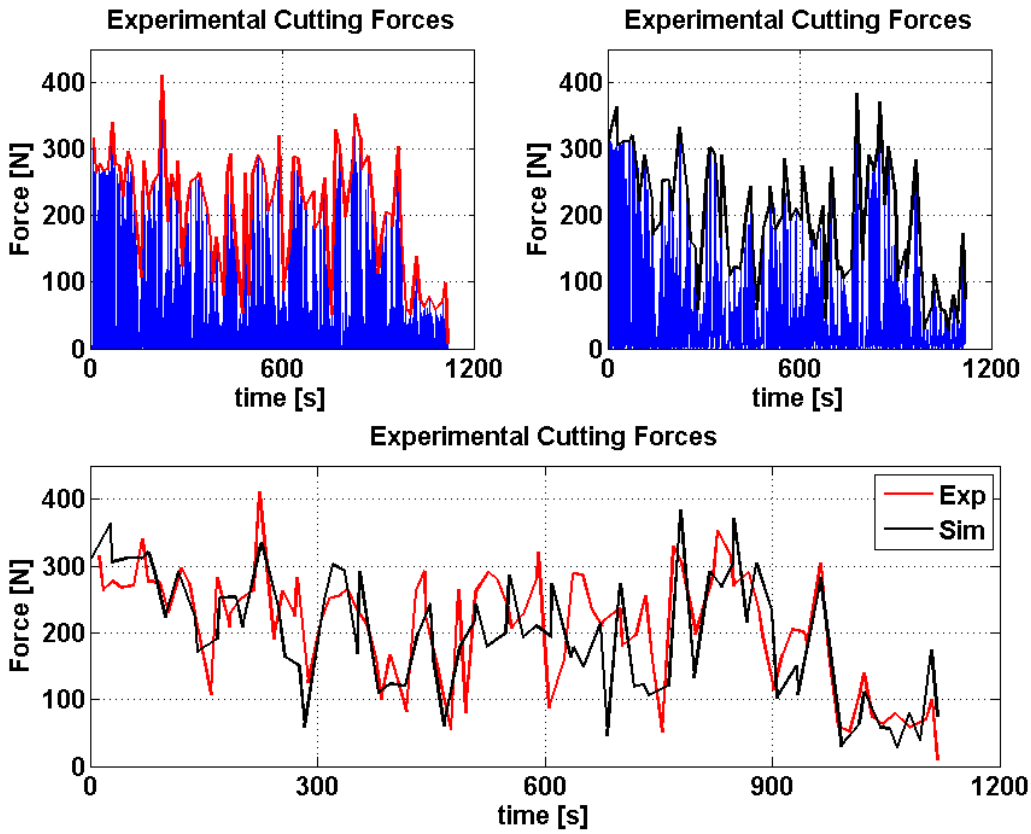

Figure 4.20 Comparing simulated and experimentally measured resultant forces for the optimized tool path.

In Figure 4.20, the experimental and simulated cutting forces and their envelopes are shown. They are matching quite well. Further the mean of the simulated cutting forces and total cycle time are 136 N and 1145 s respectively. Total cycle time is close to the objective cost of total cycle time on the pareto point. Mean cutting force is also below from the objective cost of mean cutting force as expected.

Optimization Criterion 2: Mean Cutting Force < 260 N, Mean Scallop Height < 100µm, Minimize Cycle Time

The nondominating solutions and pareto surface obtained above is used to determine the point to satisfy the optimization criterion 2. In Figure 4.21, nondominated solutions are plotted to obtain the pareto surface where also the limiting thresholds are depicted with two planes, the allowable region to work with pink points and the cycle time minimized point with big red point.

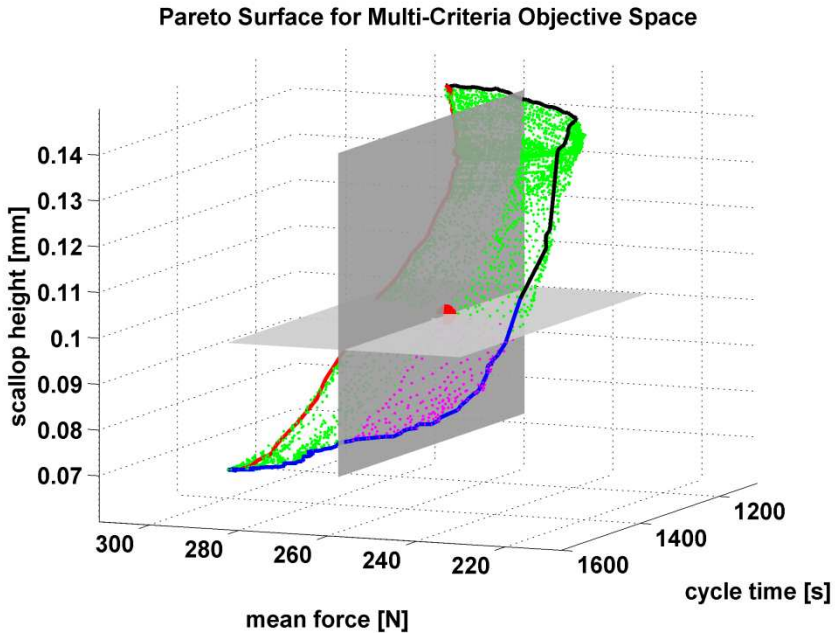

Figure 4.21 Pareto surface and solution point for optimization criterion 2 (sample 1)

All tool path solutions represented in pareto surface with their objective values are stored once the optimization routine is completed. So, for the specified criterion, the relevant point is only picked from the set of solutions. The objective costs of this point are 259 N and 1309 s and 99 μm.

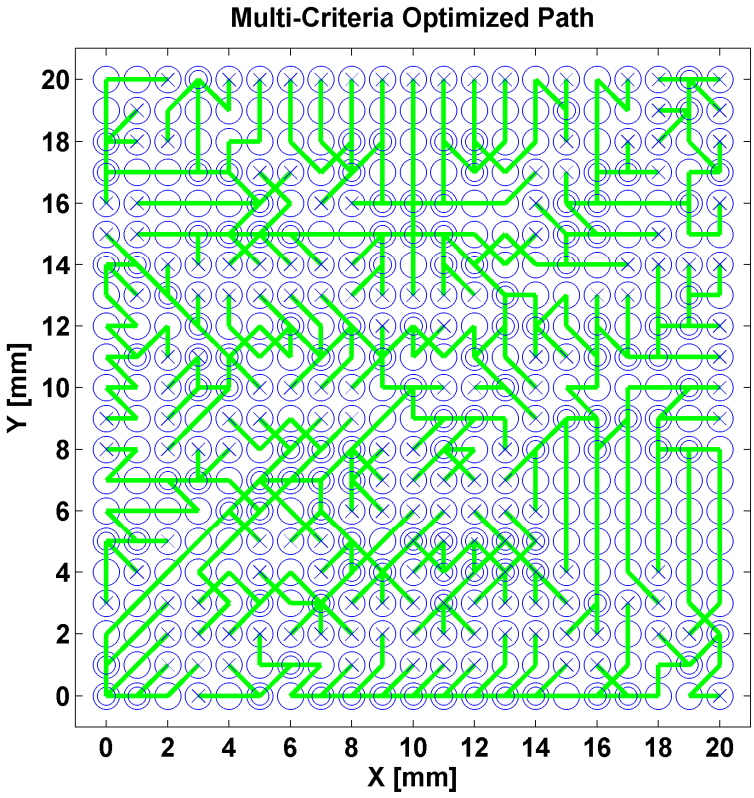

Figure 4.22 Tool path for optimization criterion 2 (sample 1)

The optimized tool path satisfying the criterion and represented with red point in the pareto surface are shown in Figure 4.22. As seen in the figure, there are diagonal edges selected in the tool path, since firstly the force and scallop limitations are determined and so the weight of total cycle time minimization is decreased to wT = 12% where wF =46% and wS=42%. The optimized solution point is outside of the top region which means that diagonal edges are needed to satisfy specified criterion.

In order to validate mean cutting force and total cycle time, the total cutting operation is firstly simulated and compared with the objective costs, then compared with the experimental cutting forces. Since the force map is formed using slot cutting simulations, it is expected that forces of the simulated tool path would remain below the graph obtained from the force map. In that sense, the simulated mean cutting force needs to be below the objective cost. Also, simulated cutting forces needs to match quite well with experimental cutting forces.

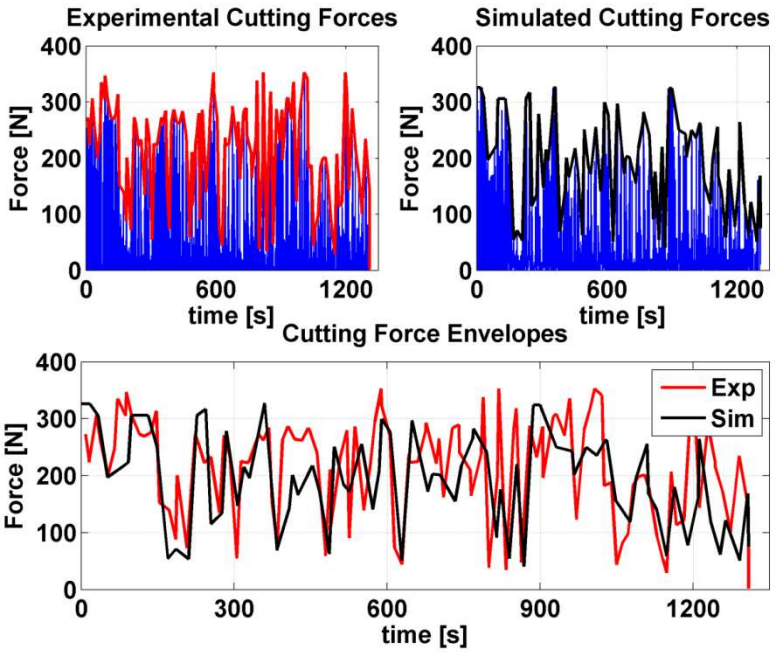

Figure 4.23 Comparing simulated and experimentally measured resultant forces for the optimized tool path.

In Figure 4.23, the experimental and simulated cutting forces and their envelopes are shown. They are matching quite well. Further the mean of the simulated cutting forces and total cycle time are 142 N and 1325 s respectively. Total cycle time is close to the objective cost of total cycle time on the pareto point. Mean cutting force is also below from the objective cost of mean cutting force as expected.

Comparison with Standard Toolpaths

Mean force, cycle time and mean scallop costs for 8 standard zig toolpaths are obtained from corresponding maps and compared with the costs of optimized toolpaths. Furthermore, experimental cutting operations are performed for these standard toolpaths and experimental mean cutting forces are plotted versus cycle times with their envelopes as shown in Figure 4.24 below.

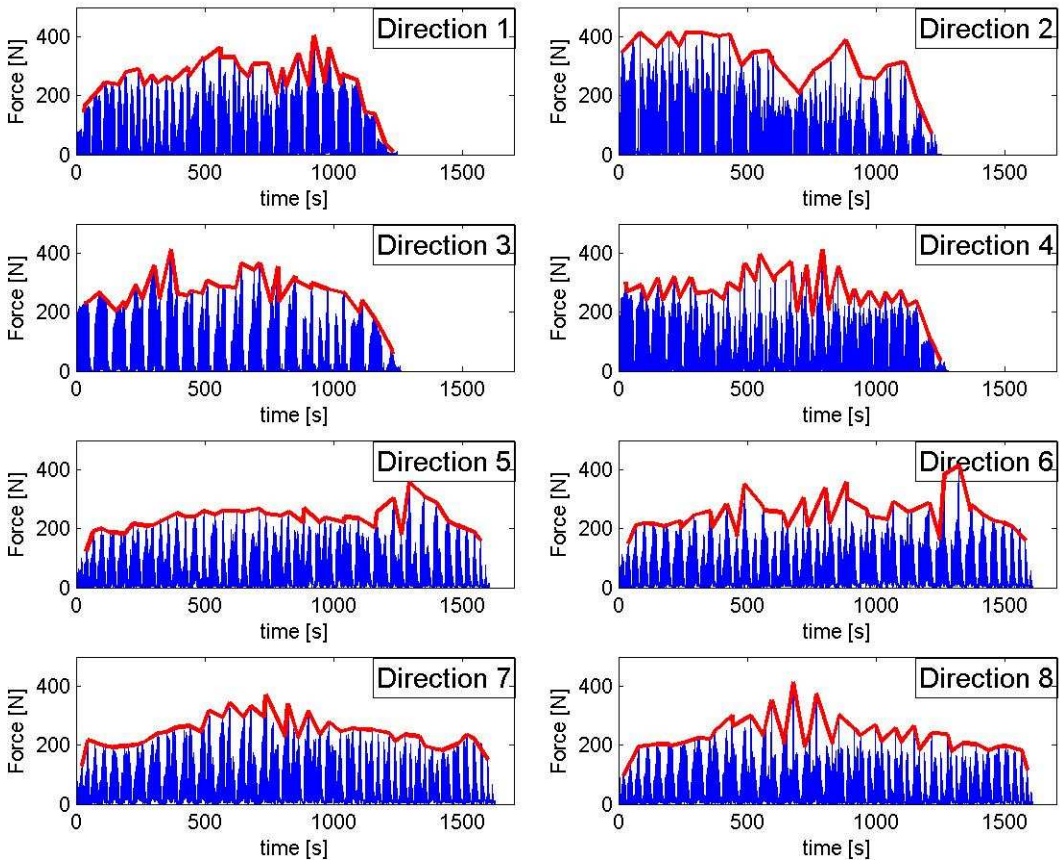

Figure 4.24 Experimental Cutting Force and Envelopes for Standard Toolpaths

Cutting force envelopes are further compared in Figure 4.25, where it is clearly shown that cutting force envelopes for diagonal toolpaths (direction 5 to 8) remain under the cutting forc envelopes for vertical/horizontal toolpaths (direction 1 to 4). However, diagonal toolpaths have longer cycle times.

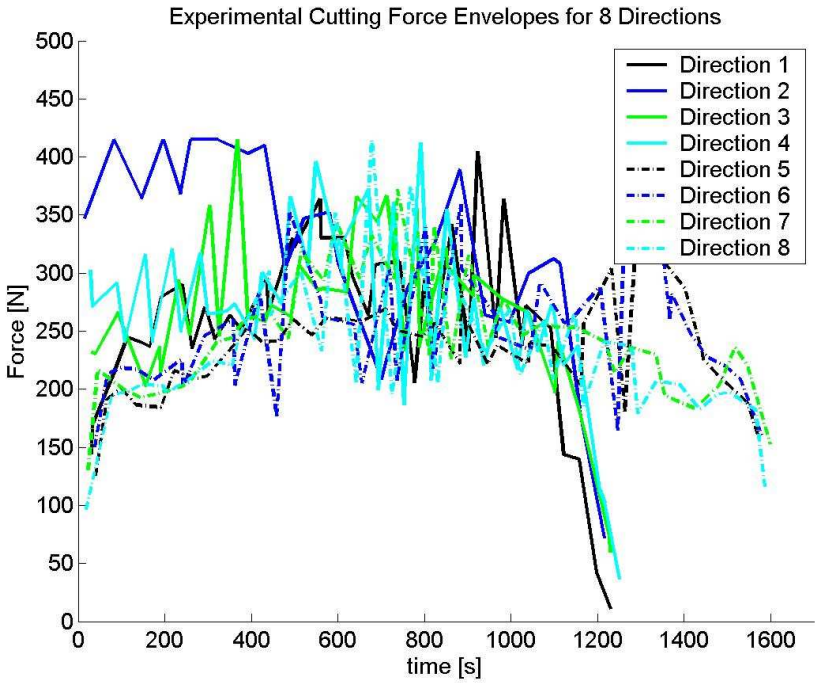

Figure 4.25 Comparison of Cutting Force Envelopes for Standard Toolpaths

Map and experimental costs are compared in the Table 4.5 below. Optimized toolpath 1 has the lowest mean cutting force and shortest cycle time when compared to standard toolpaths, and a mean scallop cost about levels of vertical/horizontal toolpaths. On the other hand, optimized toolpath 2 has a reasonably low mean cutting force and scallop height about levels of diagonal toolpaths, but has approximately 20% shorter cycle time than diagonal toolpaths.

Table 4.5 Experimental & Map Objective Costs for Sample #1

	Fmap	Tmap	Smap	Fexp	Texp
Direction 1	274	1215	138	163	1260
Direction 2	271	1215	138	167	1253
Direction 3	265	1231	128	165	1261
Direction 4	266	1231	128	169	1260
Direction 5	262	1590	87	144	1604
Direction 6	253	1593	87	140	1610
Direction 7	260	1595	87	149	1626
Direction 8	257	1595	87	154	1610
Opt 1	**245**	**1118**	**125**	**136**	**1145**
Opt 2	**259**	**1309**	**99**	**142**	**1325**

So, even the objectives are conflicting, there are pareto optimal solutions which dominate standard solutions lying in the objective space. As shown in Figure 4.26, objective points of standard toolpaths lie above the pareto surface, which assures that standard toolpaths are dominated by optimized solutions.

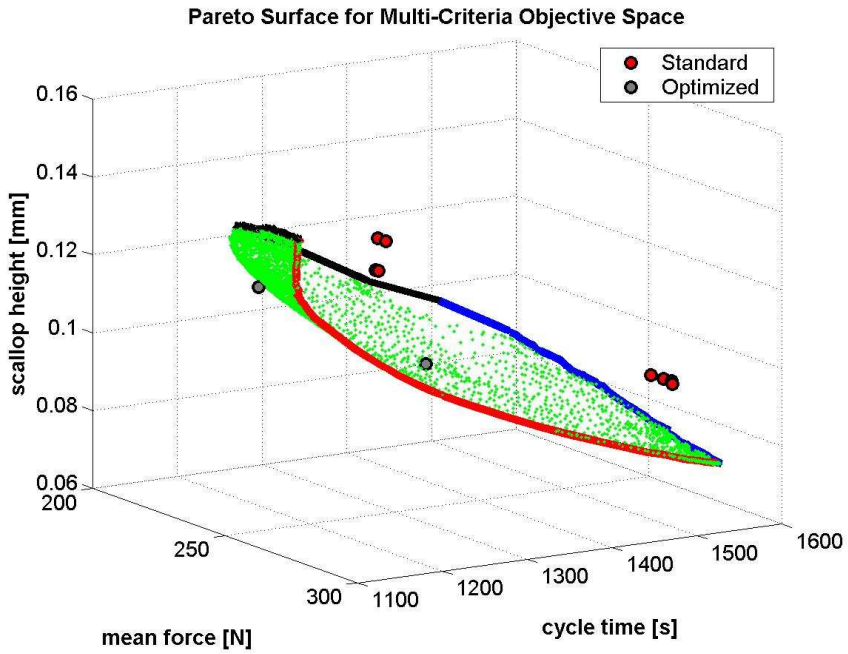

Figure 4.26 Pareto Surface with Objective Points of Standard and Optimized Toolpaths

4.4.2.2 SAMPLE 2: Free Form Surface #2 (40 mm x 40 mm x 6 mm)

Free Form Surface #2 with dimensions 40 mm x 40 mm x 6 mm is illustrated in Figure 4.27 where the equation of the surface is also explicitly shown below.

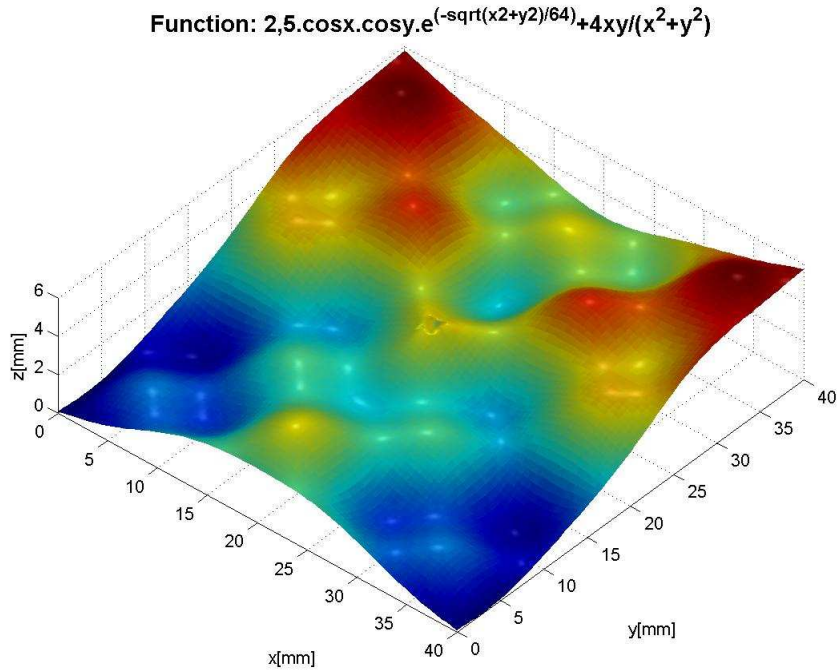

Figure 4.27 3D CAD model for sample 2

For the first step, the CL points are determined using the Collision detection based algorithm. The screen-shoot of the movie for CL determination routine is shown in Figure 4.28.

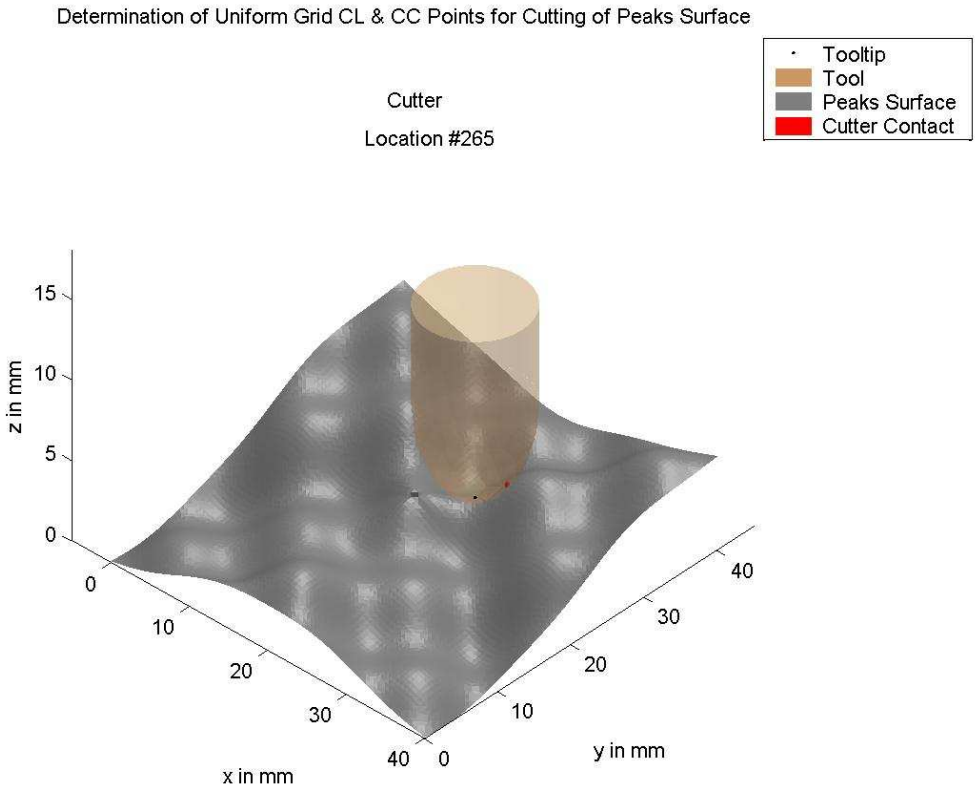

Figure 4.28 Screen shoot of CL point determination routine for sample 2

Then, the force, scallop and cycle time maps are obtained using the force and scallop height models. Cycle time map is easily obtained by calculating cycle times for each edge by division of the distance traveled between the relevant CL points to the constant feed rate of 48 mm/min. Analytically determined scallop points used to calculate scallop heights are plotted in Figure 4.29-a on the cut surface exported from UG NX6 to visually validate the pattern of the predicted scallops; furthermore the errors are calculated from the distance between the cut surface exported from UG NX6 in STL format with 0.001 mm edge tolerance and the scallop points analytically determined with scallop models in 2D and 3D. In Figure 4.29-b, the error histogram of the scallops is shown. The errors are low and reasonable.

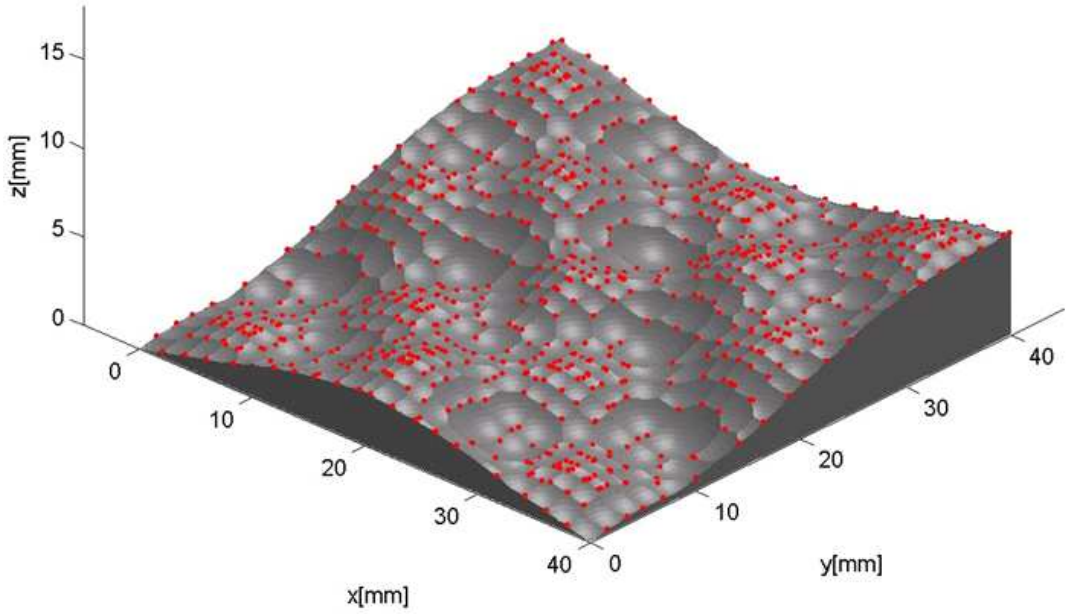

(a)

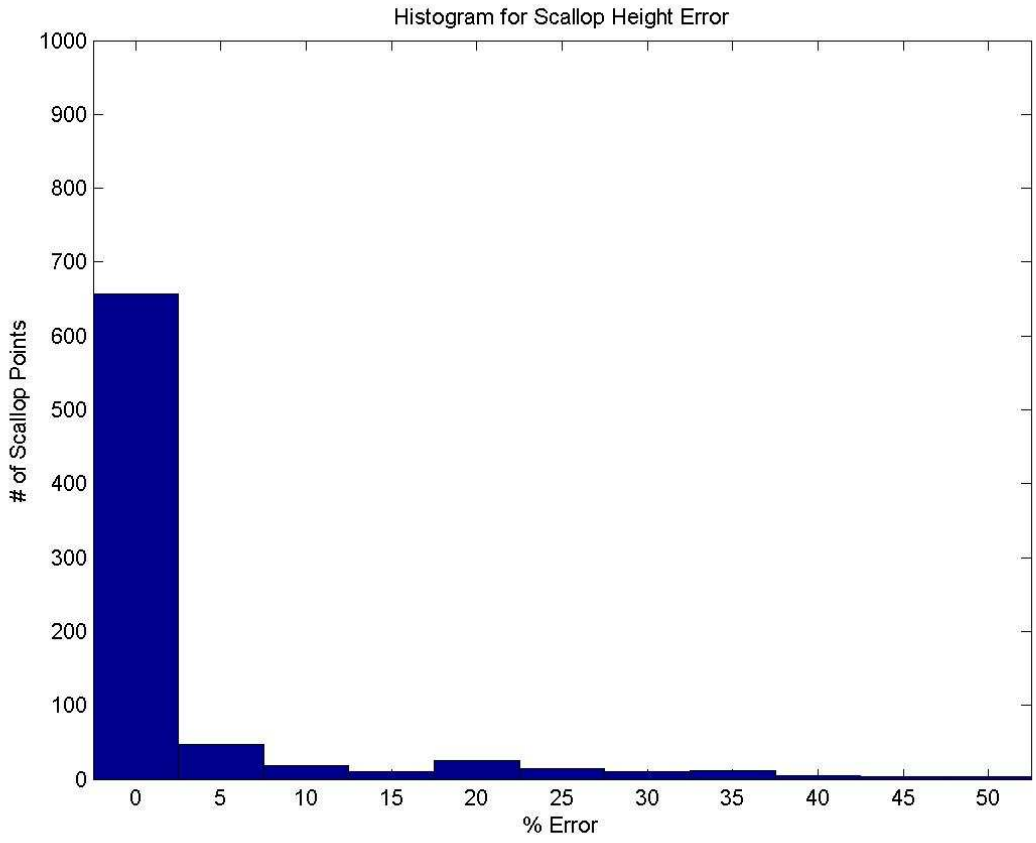

(b)

Figure 4.29 (a) Illustration of predicted scallop points on the reference cut surface

(b) Error histogram of predicted scallop heights

Optimization Criterion 1: wF = wT = wS ≈ 33%

Varying objective weighting algorithm is used with 1% sensitivity where weights of each criterion (mean cutting force, mean scallop height, total cycle time) changed from 0% to 100%. After that, all obtained nondominated solutions are plotted to obtain the pareto surface as shown in Figure 4.30 where also the single point of wF = wT = wS is depicted with pink point. Theoretically this nondominating solution point is the closest point to the ideal point of the objective space.

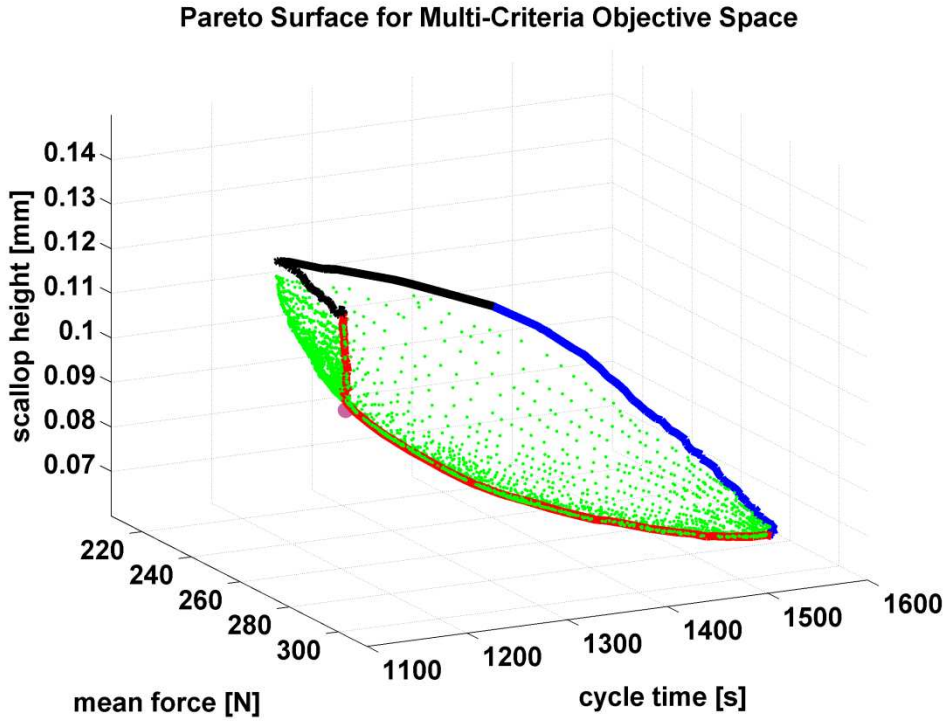

Figure 4.30 Pareto surface and solution point for optimization criterion 1 (sample 2)

All tool path solutions represented in pareto surface with their objective values are stored once the optimization routine is completed. So, for wF = wS = wT only the corresponding point is picked from the solutions. The objective costs of this point are 295 N, 1120 s and 110 μm.

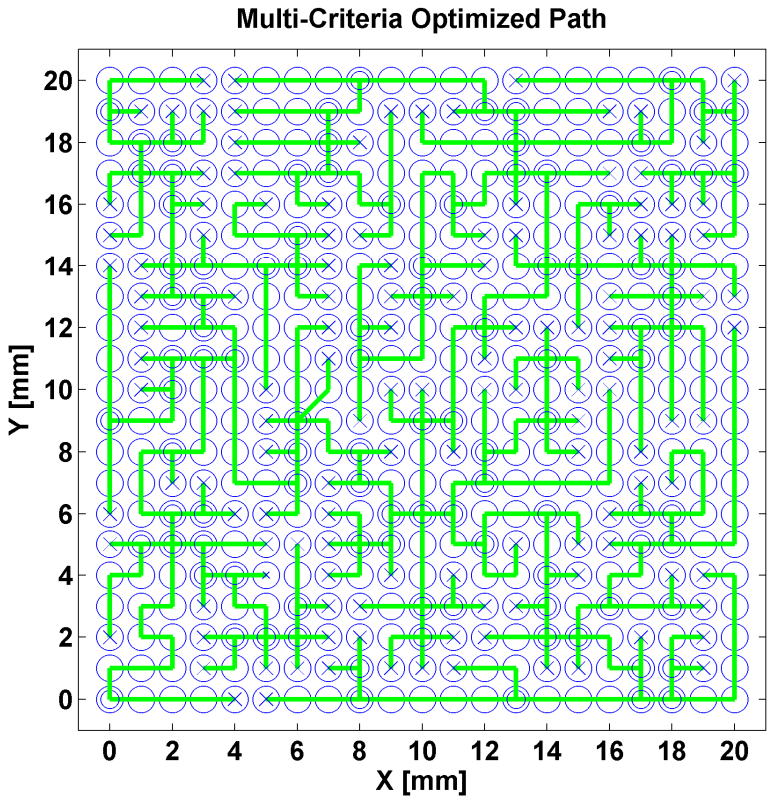

Figure 4.31 Tool path for optimization criterion 1 (sample 2)

The optimized tool path satisfying the criterion and represented with pink point in the pareto surface are shown in Figure 4.31. As seen in the figure, there are no diagonal edges selected in the tool path, because the weight of total cycle time minimization is reasonably high (wT = 33%) and the optimization routine tends to escape from diagonal edges with a weighting of 33%.

In order to validate mean cutting force and total cycle time, the total cutting operation is firstly simulated and compared with the objective costs, then compared with the experimental cutting forces. Since the force map is formed using slot cutting simulations, it is expected that forces of the simulated tool path would remain below the graph obtained from the force map. In that sense, the simulated mean cutting force needs to be below the objective cost. Also, simulated cutting forces needs to match quite well with experimental cutting forces.

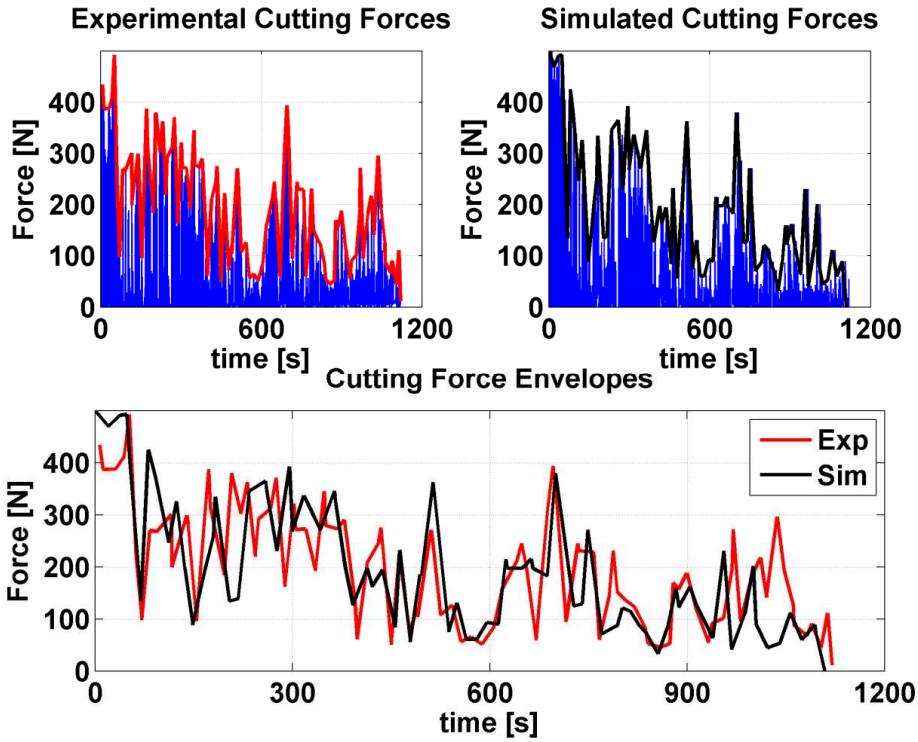

Figure 4.32 Comparing simulated and experimentally measured resultant forces for the optimized tool path.

In Figure 4.32, the experimental and simulated cutting forces and their envelopes are shown. They are matching quite well. Further the mean of the simulated cutting forces and total cycle times are 137 N and 1148 s respectively. Total cycle time is close to the objective cost of total cycle time on the pareto point. Mean cutting force is also below from the objective cost of mean cutting force as expected.

Optimization Criterion 2: Mean Cutting Force < 260 N, Mean Scallop Height < 100 µm, Minimize Cycle Time

The nondominating solutions and pareto surface obtained above is used to determine the point to satisfy the optimization criterion 2. In Figure 4.33, nondominated solutions are plotted to obtain the pareto surface where also the limiting thresholds are depicted with two planes, the allowable region to work with pink points and the cycle time minimized point with big red point.

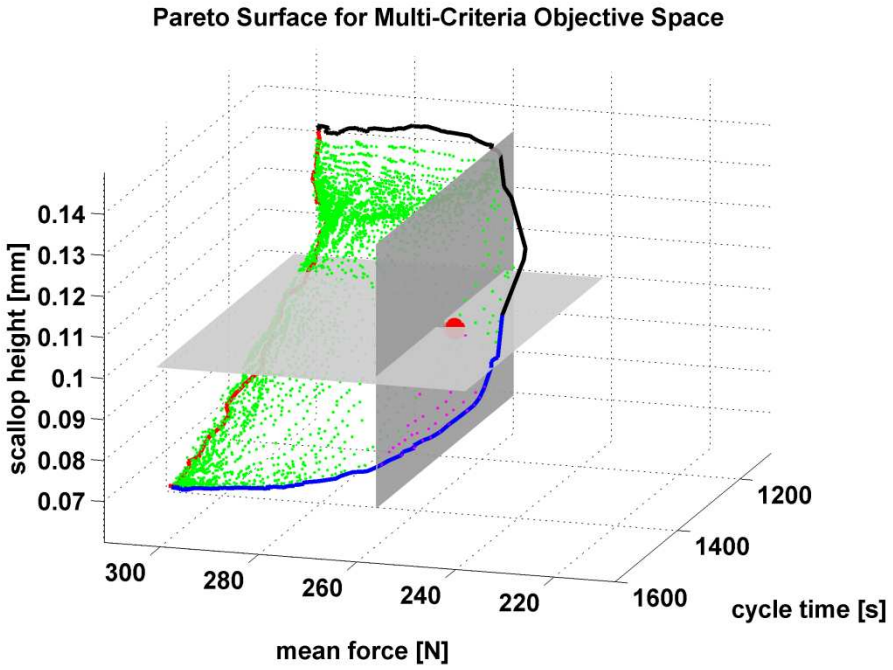

Figure 4.33 Pareto surface and solution point for optimization criterion 2 (sample 2)

All tool path solutions represented in pareto surface with their objective values are stored once the optimization routine is completed. So, for the specified criterion, the relevant point is only picked from the set of solutions. The objective costs of this point are 258 N, 1321 s and 100 μm.

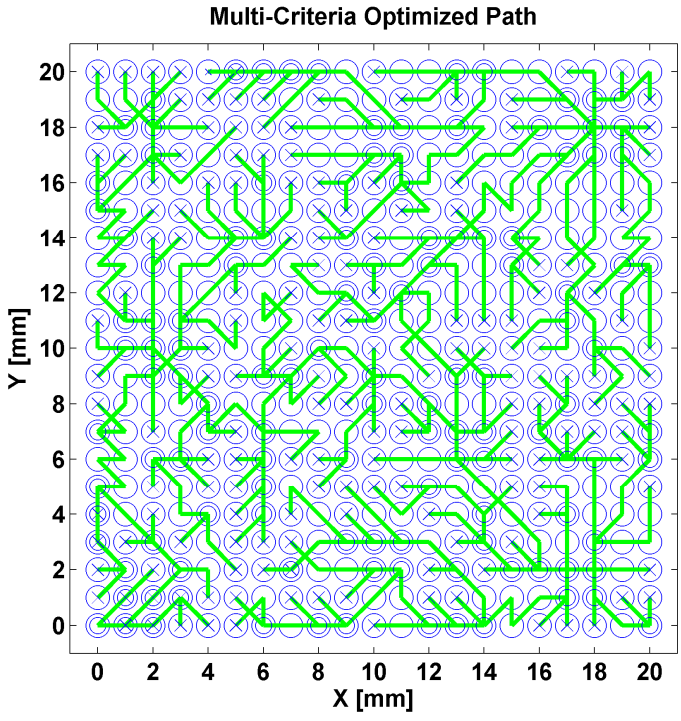

Figure 4.34 Tool path for optimization criterion 2 (sample 2)

The optimized tool path satisfying the criterion and represented with red point in the pareto surface are shown in Figure 4.34. As seen in the figure, there are diagonal edges selected in the tool path, since firstly the force and scallop limitations are determined and so the weight of total cycle time minimization is decreased to wT = 4% where wF is 85% and wS is 11%. The optimized solution point is outside of the top region which means that diagonal edges are needed to satisfy specified criterion.

In order to validate mean cutting force and total cycle time, the total cutting operation is firstly simulated and compared with the objective costs, then compared with the experimental cutting forces. Since the force map is formed using slot cutting simulations, it is expected that forces of the simulated tool path would remain below the graph obtained from the force map. In that sense, the simulated mean cutting force needs to be below the objective cost. Also, simulated cutting forces needs to match quite well with experimental cutting forces.

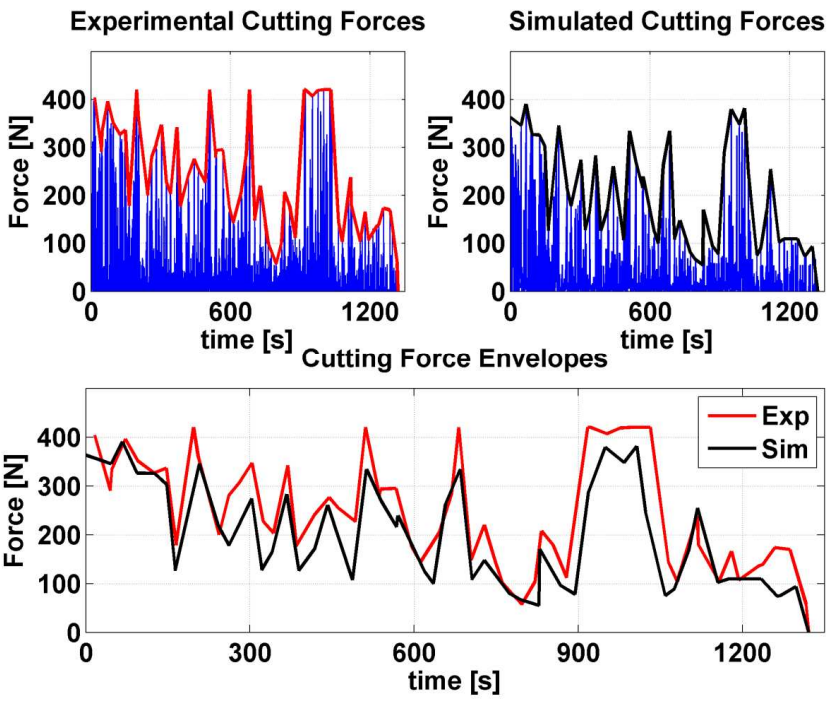

Figure 4.35 Comparing simulated and experimentally measured resultant forces for the optimized tool path.

In Figure 4.35, the experimental and simulated cutting forces and their envelopes are shown. They are matching quite well. Further the mean of the simulated cutting forces and total cycle times are 130 N and 1352 s respectively. Total cycle time is

close to the objective cost of total cycle time on the pareto point. Mean cutting force is also below from the objective cost of mean cutting force as expected.

Comparison with Standard Toolpaths

Mean force, cycle time and mean scallop costs for 8 standard zig toolpaths are obtained from corresponding maps and compared with the costs of optimized toolpaths. Furthermore, experimental cutting operations are performed for these standard toolpaths and experimental mean cutting forces are plotted versus cycle times with their envelopes as shown in Figure 4.36 below.

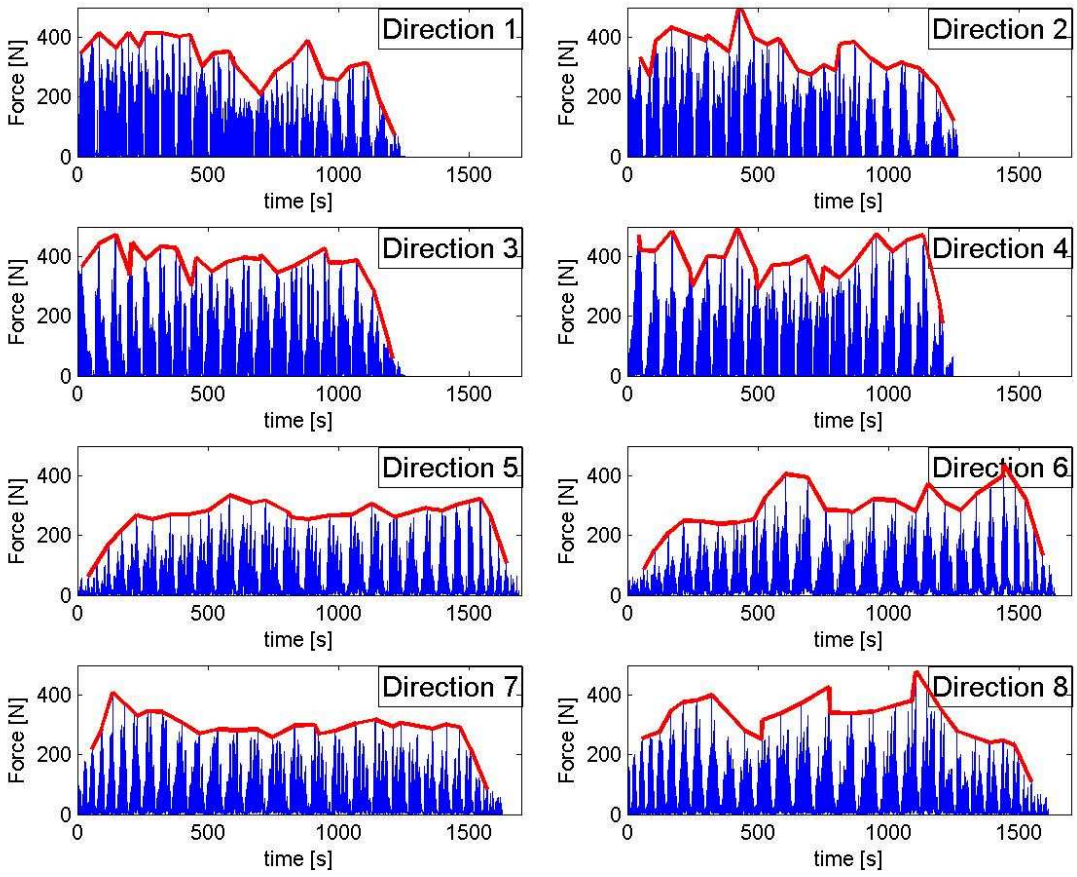

Figure 4.36 Experimental Cutting Force and Envelopes for Standard Toolpaths

Cutting force envelopes are further compared in Figure 4.37, where it is clearly shown that cutting force envelopes for diagonal toolpaths (direction 5 to 8) remain under the cutting force envelopes for vertical/horizontal toolpaths (direction 1 to 4). However, diagonal toolpaths have longer cycle times.

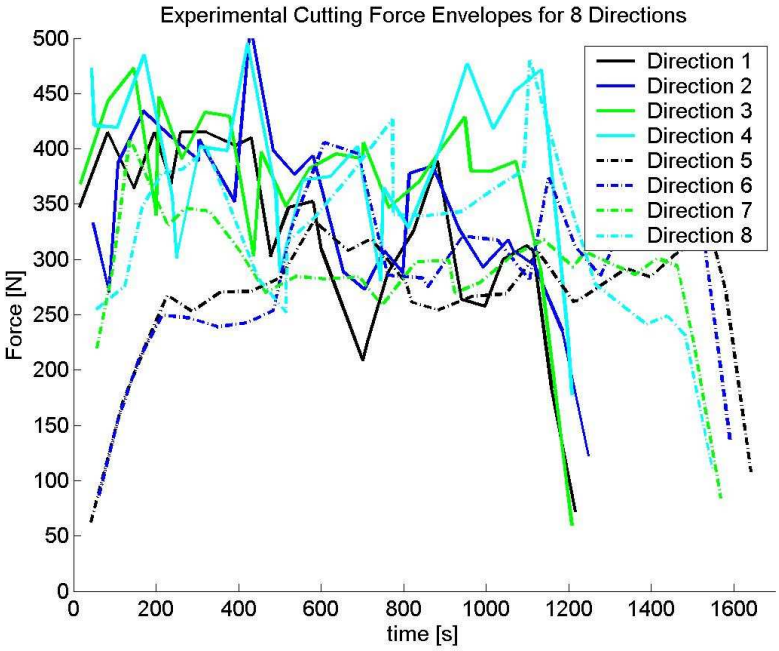

Figure 4.37 Comparison of Cutting Force Envelopes for Standard Toolpaths

Map and experimental costs are compared in Table 4.6 as below. Optimized toolpath 1 has the shortest cycle time when compared to standard toolpaths, and a mean cutting force about levels of vertical/horizontal toolpaths and a mean scallop cost below levels of vertical/horizontal toolpaths. On the other hand, optimized toolpath 2 has lowest mean cutting force and a scallop height about levels of diagonal toolpaths, but has approximately 20% shorter cycle time than diagonal toolpaths.

Table 4.6 Experimental & Map Objective Costs for Sample #2

	Fmap	Tmap	Smap	Fexp	Texp
Zig 1	294	1229	127	183	1253
Zig 2	284	1229	127	179	1265
Zig 3	286	1228	128	192	1255
Zig 4	289	1228	128	198	1248
Zig 5	266	1600	86	132	1631
Zig 6	269	1600	86	134	1638
Zig 7	272	1595	88	149	1628
Zig 8	275	1595	88	157	1611
Opt 1	**295**	**1120**	**110**	**176**	**1148**
Opt 2	**258**	**1321**	**100**	**130**	**1352**

So, even the objectives are conflicting, there are pareto optimal solutions which dominate standard solutions lying in the objective space. As shown in Figure 4.38, objective points of standard toolpaths lie above the pareto surface, which assures that standard toolpaths are dominated by optimized solutions.

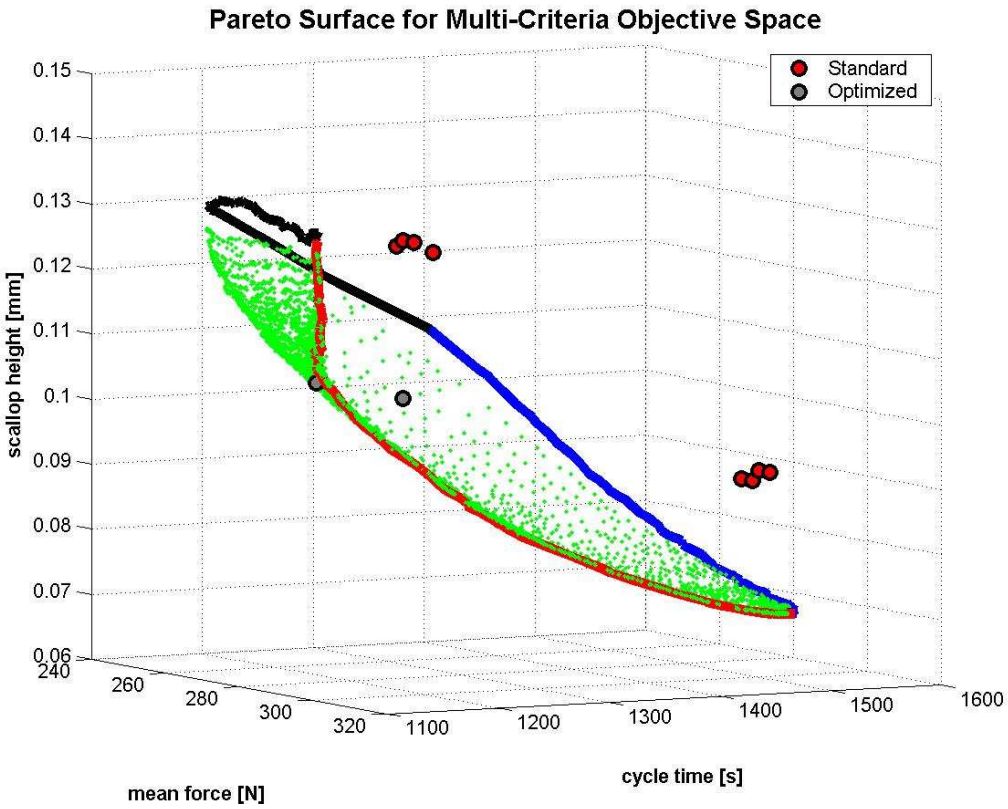

Figure 4.38 Pareto Surface with Objective Points of Standard and Optimized Toolpaths

4.4.2.3 SAMPLE 3: Free Form Surface #3 (40 mm x 40 mm x 6 mm)

Free Form Surface #3 with dimensions 40 mm x 40 mm x 6 mm is illustrated in Figure 4.39 where the equation of the surface is also explicitly shown below.

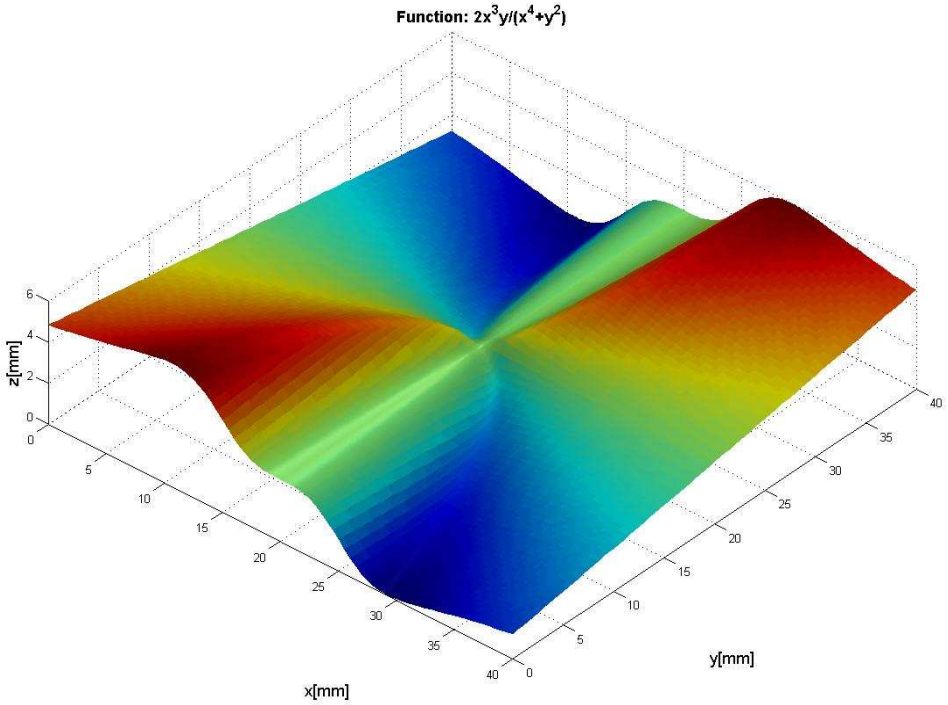

Figure 4.39 3D CAD model for sample 2

For the first step, the CL points are determined using the Collision detection based algorithm. The screen-shoot of the movie for CL determination routine is shown in Figure 4.40.

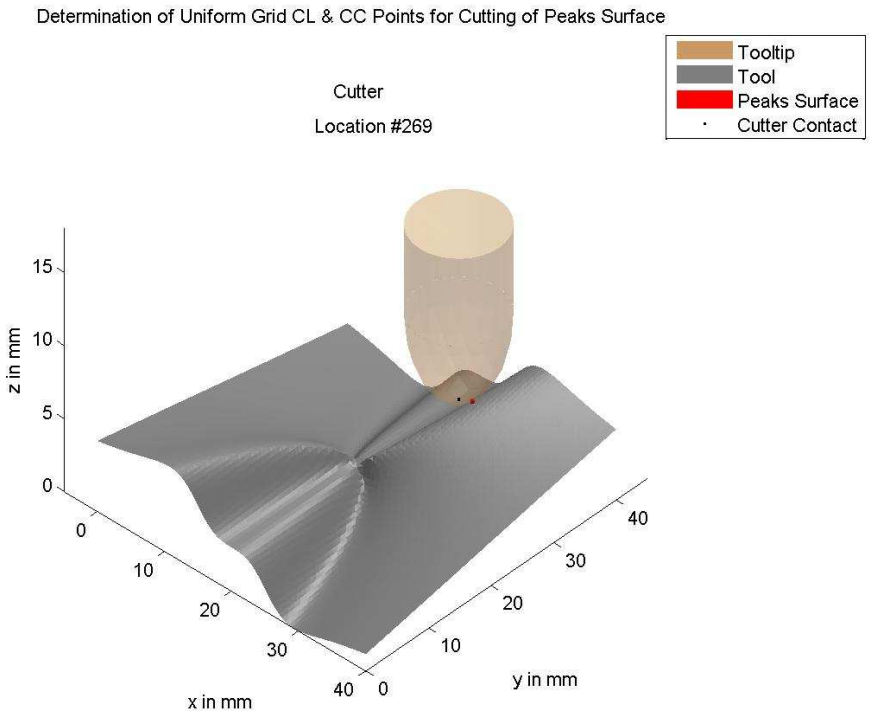

Figure 4.40 Screen shoot of CL point determination routine for sample 3

Then, the force, scallop and cycle time maps are obtained using the force and scallop height models. Cycle time map is easily obtained by calculating cycle times for each edge by division of the distance traveled between the relevant CL points to the constant feed rate of 48 mm/min. Analytically determined scallop points used to calculate scallop heights are plotted in Figure 4.41-a on the cut surface exported from UG NX6 to visually validate the pattern of the predicted scallops; furthermore the errors are calculated from the distance between the cut surface exported from UG NX6 in STL format with 0.001 mm edge tolerance and the scallop points analytically determined with scallop models in 2D and 3D. In Figure 4.41-b, the error histogram of the scallops is shown. The errors are low and reasonable.

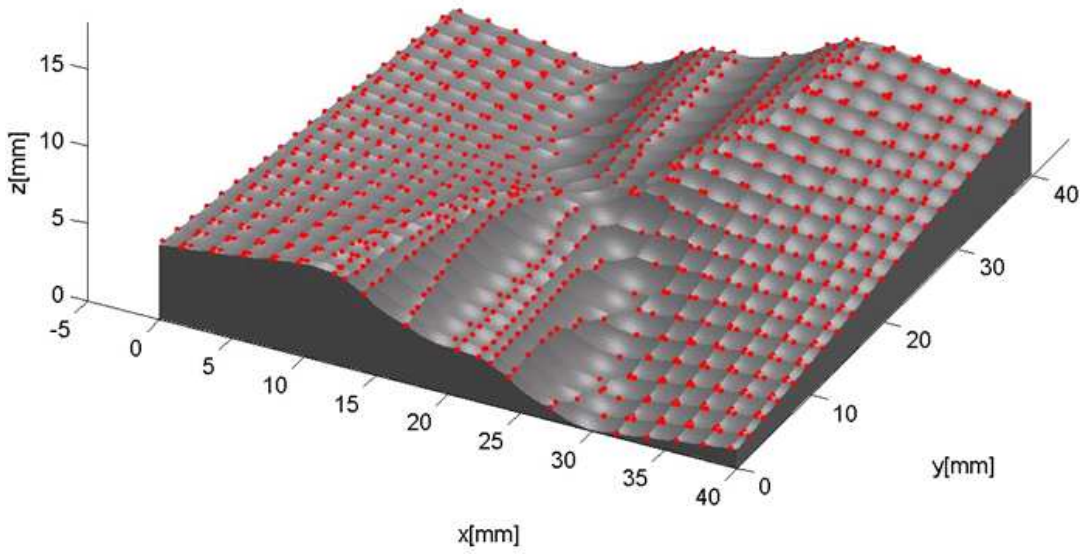

(a)

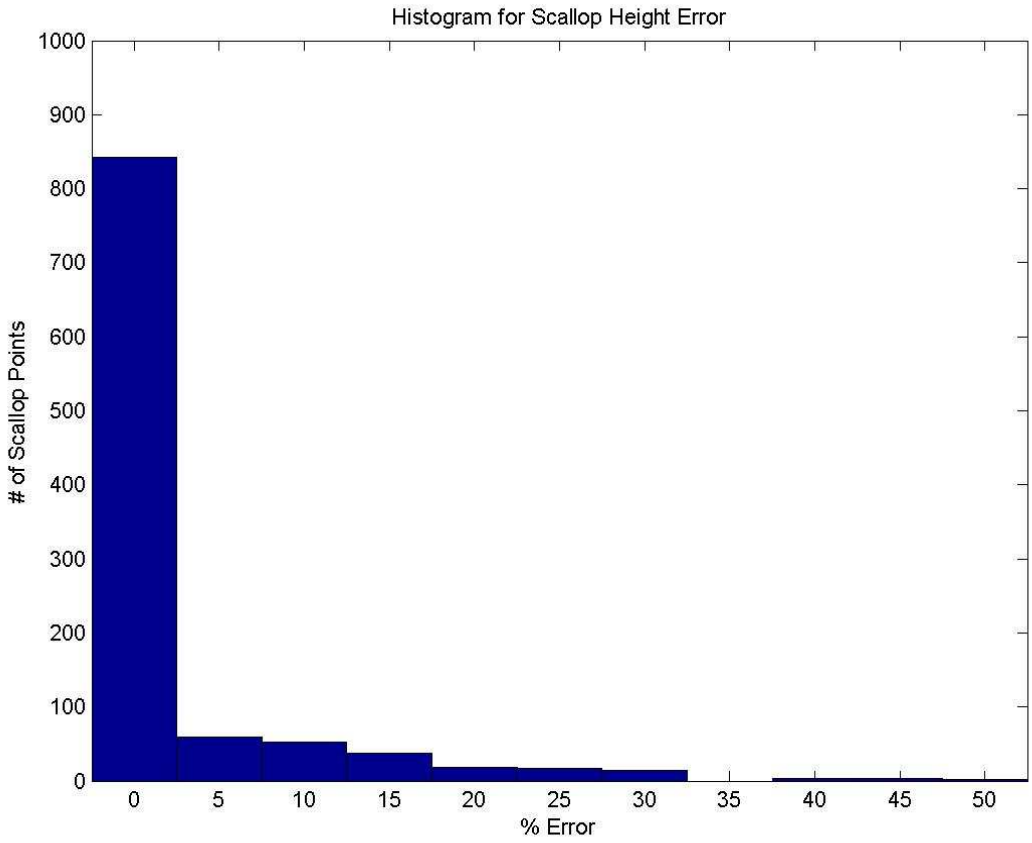

(b)

Figure 4.41 (a) Illustration of predicted scallop points on the reference cut surface

(b) Error histogram of predicted scallop heights

Optimization Criterion 1: wF = wT = wS ≈ 33%

Varying objective weighting algorithm is used with 1% sensitivity where weights of each criterion (mean cutting force, mean scallop height, total cycle time) changed from 0% to 100%. After that, all obtained nondominated solutions are plotted to obtain the pareto surface as shown in Figure 4.42 where also the single point of wF = wT = wS is depicted with pink point. Theoretically this nondominating solution point is the closest point to the ideal point of the objective space.

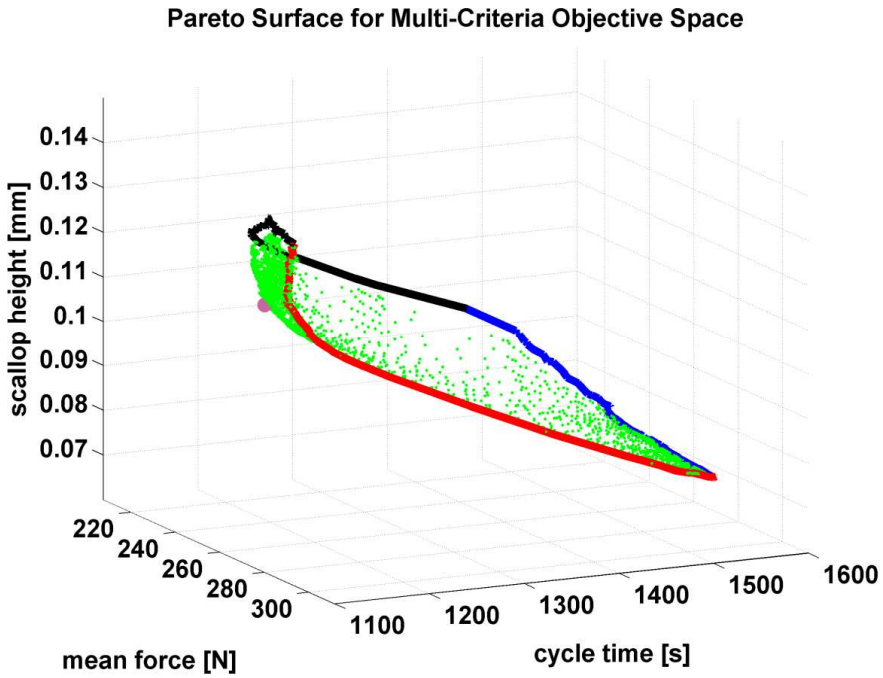

Figure 4.42 Pareto surface and solution point for optimization criterion 1 (sample 3)

All tool path solutions represented in pareto surface with their objective values are stored once the optimization routine is completed. So, for wF = wS = wT only the corresponding point is picked from the solutions. The objective costs of this point are 273 N, 1116 s and 120 μm.

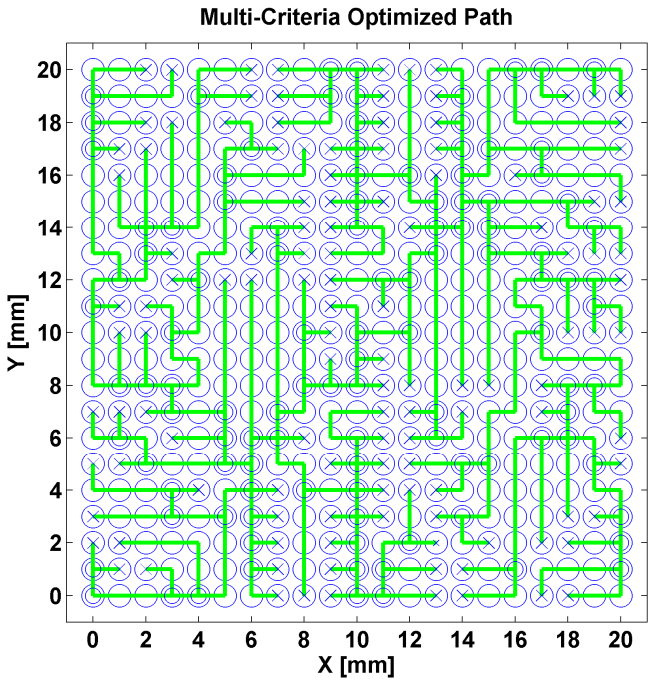

Figure 4.43 Tool path for optimization criterion 1 (sample 3)

The optimized tool path satisfying the criterion and represented with pink point in the pareto surface are shown in Figure 4.43. As seen in the figure, there are no diagonal edges selected in the tool path, because the weight of total cycle time minimization is reasonably high (wT = 33%) and the optimization routine tends to escape from diagonal edges with a weighting of 33%.

In order to validate mean cutting force and total cycle time, the total cutting operation is firstly simulated and compared with the objective costs, then compared with the experimental cutting forces. Since the force map is formed using slot cutting simulations, it is expected that forces of the simulated tool path would remain below the graph obtained from the force map. In that sense, the simulated mean cutting force needs to be below the objective cost. Also, simulated cutting forces needs to match quite well with experimental cutting forces.

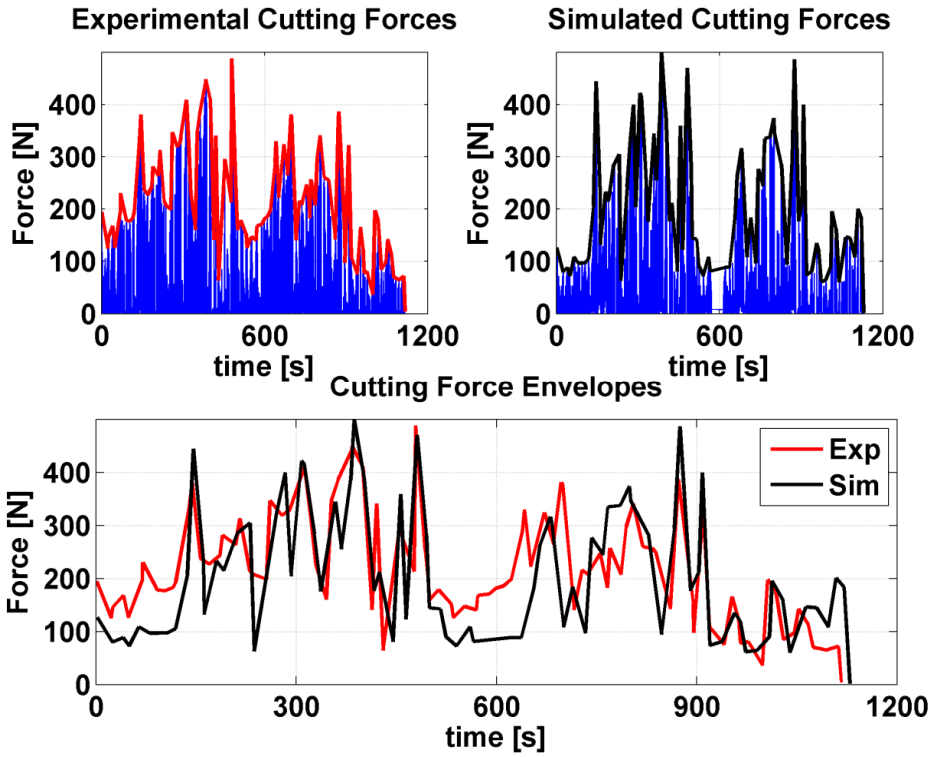

Figure 4.44 Comparing simulated and experimentally measured resultant forces for the optimized tool path.

In Figure 4.44, the experimental and simulated cutting forces and their envelopes are shown. They are matching quite well. Further the mean of the simulated cutting forces and total cycle times are 147 N and 1130 s respectively. Total cycle time is

close to the objective cost of total cycle time on the pareto point. Mean cutting force is also below from the objective cost of mean cutting force as expected.

Optimization Criterion 2: Mean Cutting Force < 260 N, Mean Scallop Height < 100 µm, Minimize Cycle Time

The nondominating solutions and pareto surface obtained above is used to determine the point to satisfy the optimization criterion 2. In Figure 4.45, nondominated solutions are plotted to obtain the pareto surface where also the limiting thresholds are depicted with two planes, the allowable region to work with pink points and the cycle time minimized point with big red point.

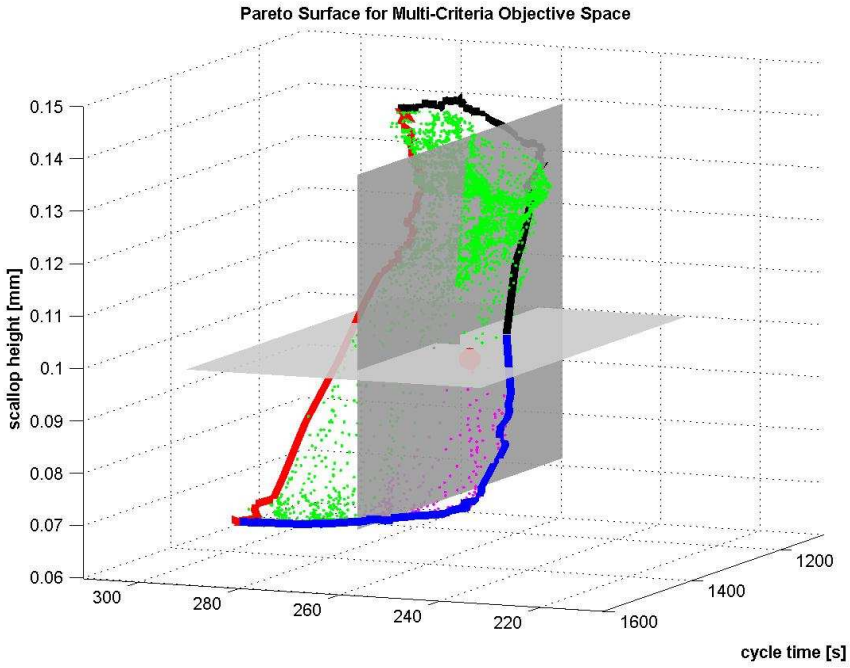

Figure 4.45 Pareto surface and solution point for optimization criterion 2 (sample 3)

All tool path solutions represented in pareto surface with their objective values are stored once the optimization routine is completed. So, for the specified criterion, the relevant point is only picked from the set of solutions. The objective costs of this point are 258 N, 1334 s and 97 µm.

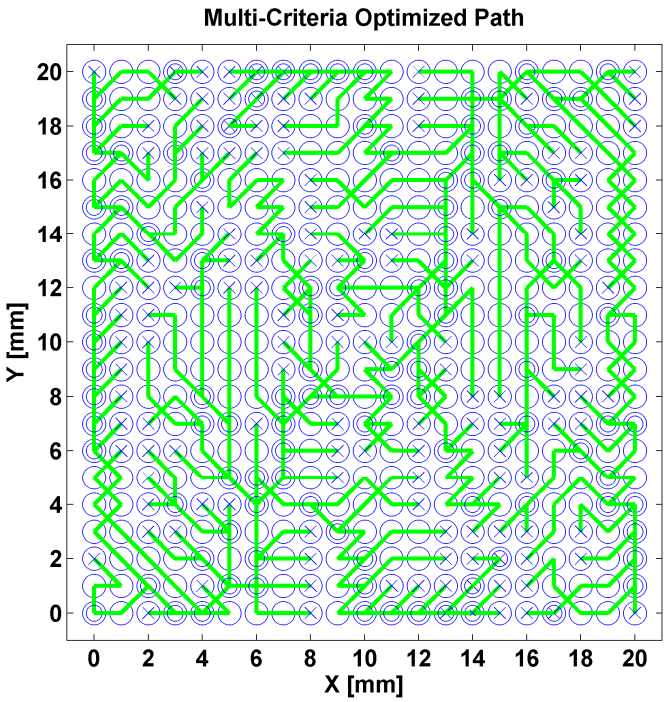

Figure 4.46 Tool path for optimization criterion 2 (sample 3)

The optimized tool path satisfying the criterion and represented with red point in the pareto surface are shown in Figure 4.46. As seen in the figure, there are diagonal edges selected in the tool path, since firstly the force and scallop limitations are determined and so the weight of total cycle time minimization is decreased to wT = 5% where wF = 75% and wS = 20%. The optimized solution point is outside of the top region which means that diagonal edges are needed to satisfy specified criterion.

In order to validate mean cutting force and total cycle time, the total cutting operation is firstly simulated and compared with the objective costs, then compared with the experimental cutting forces. Since the force map is formed using slot cutting simulations, it is expected that forces of the simulated tool path would remain below the graph obtained from the force map. In that sense, the simulated mean cutting force needs to be below the objective cost. Also, simulated cutting forces needs to match quite well with experimental cutting forces.

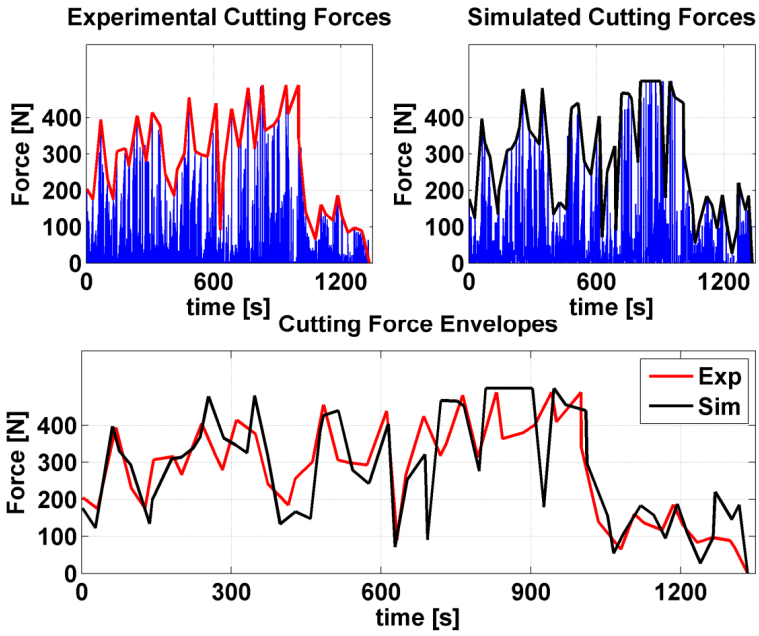

Figure 4.47 Comparing simulated and experimentally measured resultant forces for the optimized tool path.

In Figure 4.47, the experimental and simulated cutting forces and their envelopes are shown. They are matching quite well. Further the mean of the simulated cutting forces and total cycle times are 136 N and 1346 s respectively. Total cycle time is close to the objective cost of total cycle time on the pareto point. Mean cutting force is also below from the objective cost of mean cutting force as expected.

Comparison with Standard Toolpaths

Mean force, cycle time and mean scallop costs for 8 standard zig toolpaths are obtained from corresponding maps and compared with the costs of optimized toolpaths. Furthermore, experimental cutting operations are performed for these standard toolpaths and experimental mean cutting forces are plotted versus cycle times with their envelopes as shown in Figure 4.48 below.

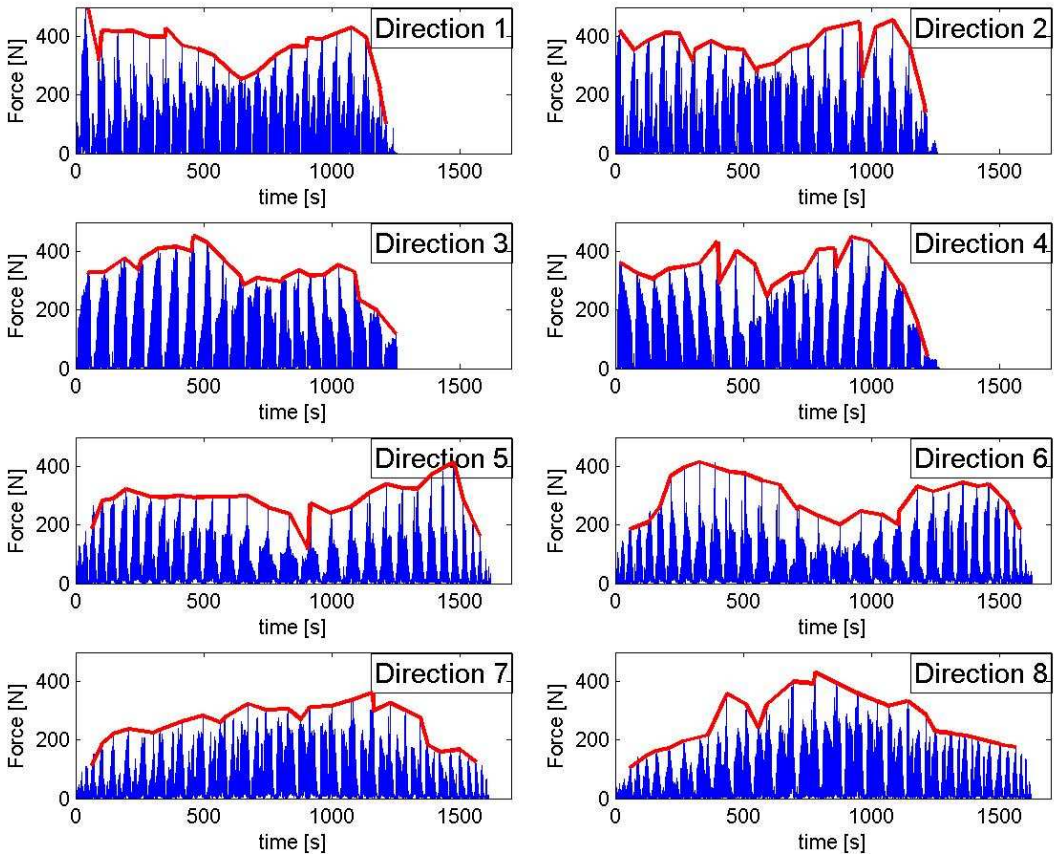

Figure 4.48 Experimental Cutting Force and Envelopes for Standard Toolpaths

Cutting force envelopes are further compared in Figure 4.49, where it is clearly shown that cutting force envelopes for diagonal toolpaths (direction 5 to 8) remain under the cutting forc envelopes for vertical/horizontal toolpaths (direction 1 to 4). However, diagonal toolpaths have longer cycle times.

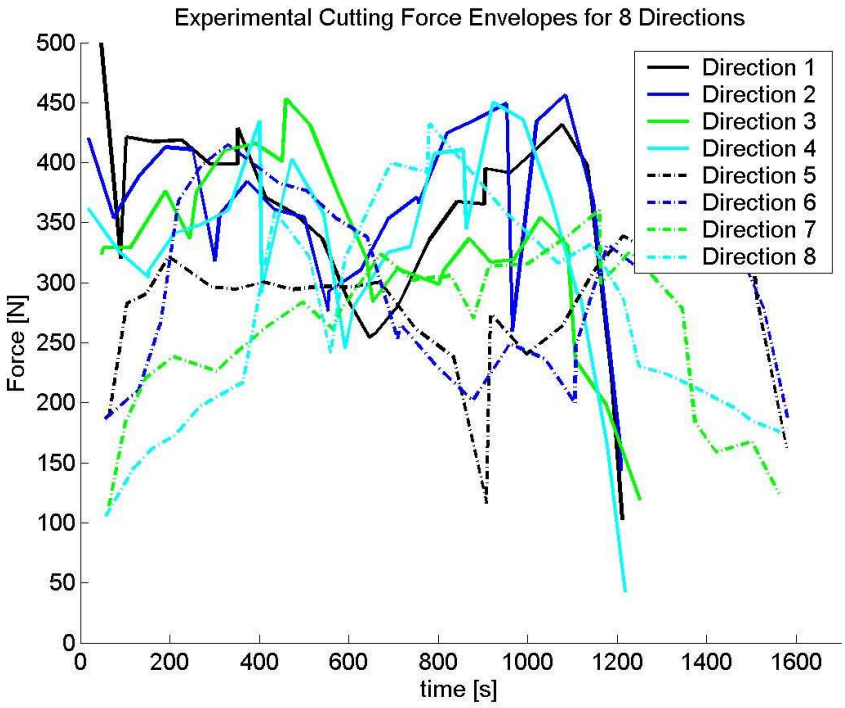

Figure 4.49 Comparison of Cutting Force Envelopes for Standard Toolpaths

Map and experimental costs are compared in Table 4.7 as below. Optimized toolpath 1 has the shortest cycle time when compared to standard toolpaths, and a mean cutting force about levels of diagonal toolpaths and below levels of vertical/horizontal toolpaths, and a mean scallop cost about levels of vertical/horizontal toolpaths. On the other hand, optimized toolpath 2 has lowest mean cutting force and a scallop height about levels of diagonal toolpaths, but has approximately 20% shorter cycle time than diagonal toolpaths.

Table 4.7 Experimental & Map Objective Costs for Sample #3

	Fmap	Tmap	Smap	Fexp	Texp
Zig 1	285	1234	128	184	1256
Zig 2	284	1234	128	186	1258
Zig 3	285	1217	133	186	1255
Zig 4	284	1216	133	182	1265
Zig 5	264	1595	87	140	1621
Zig 6	265	1595	87	139	1627
Zig 7	277	1595	88	143	1614
Zig 8	276	1595	88	147	1625
Opt 1	**273**	**1116**	**120**	**147**	**1130**
Opt 2	**258**	**1334**	**97**	**136**	**1346**

So, even the objectives are conflicting, there are pareto optimal solutions which dominate standard solutions lying in the objective space. As shown in Figure 4.50, objective points of standard toolpaths lie above the pareto surface, which assures that standard toolpaths are dominated by optimized solutions.

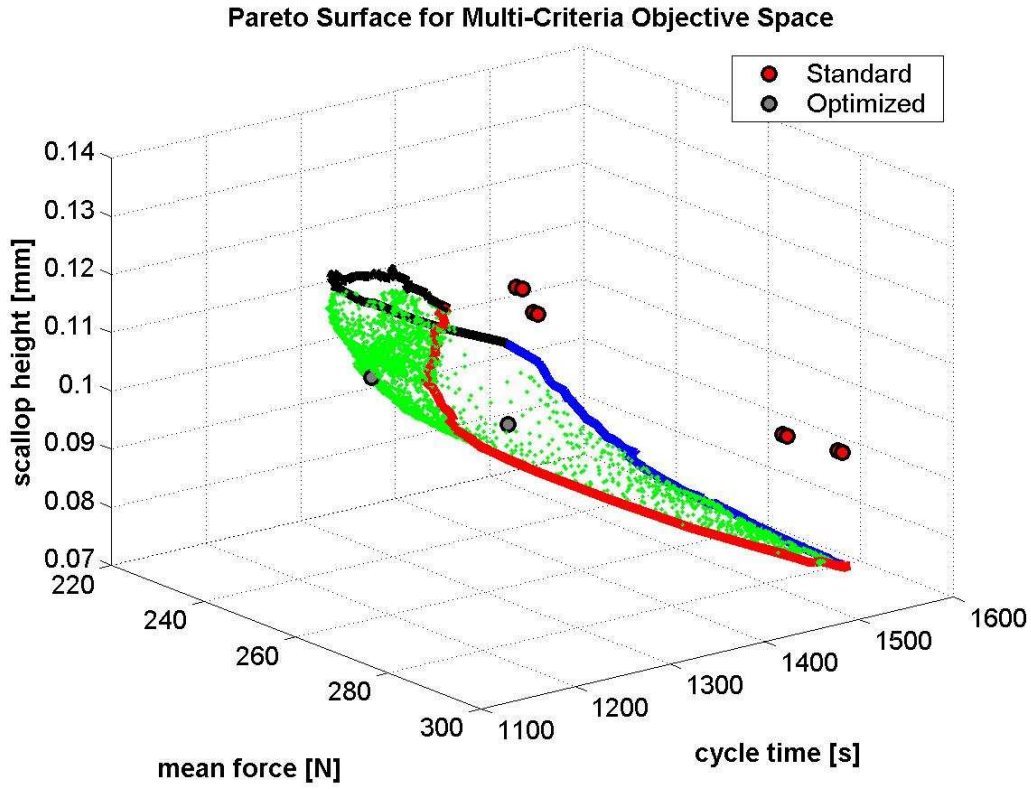

Figure 4.50 Pareto Surface with Objective Points of Standard and Optimized Toolpaths

Chapter 5
Conclusions

The aim of this study has been to develop an accurate tool path optimization method based on cutting operation and part surface parameters such as cutting forces, scallop height and cycle time to improve the productivity and part quality. Free-form sculptured surfaces are very popular in many industries and in machining of dies, molds, automobile and aerospace parts. Therefore, tool path optimization via accurate prediction of cutting forces, scallop heights and cycle times during machining allows improving productivity by minimizing cutting forces, scallop heights and cycle time according to the applied user defined objectives regarding to the demanded and desired tool life, operation time and surface quality. As a result, knowledge gained from this thesis can be used to select appropriate tool paths and cutting conditions which result in better part quality in a shorter cycle time.

The geometry of the ball-end mill used in this study was defined according to the previous studies of Guzel and Lazoglu [1], and Erdim [2]. Solid based approach to the tool-workpiece engagement region and mechanistic cutting force model was defined according to the previous studies of Kaymakci [35] and used for 3D complex sculptured free-form surfaces with ball-end milling for simulating and validating force predictions. Measured forces, force patterns and simulations for these parts showed very good agreement.

As stated before, as the demand for free-form surfaces in industry increases, CAD/CAM software companies develop different tool path strategies for machining of complex sculptured surfaces. However, since there are different tool paths available to carry out the same process, a question arises that which tool path strategy is the best choice for a specific free-form surface. As it can be predicted, each tool path strategy offers different cutting time, cutting force magnitude and surface quality.

In this study, a new methodology is introduced to determine the optimum tool paths for free form surfaces. Unlike only geometric computational analysis of commercial CAM systems, the newly developed optimization process includes the mechanics of milling process for the tool path generations. The tool path optimization algorithm presented is a force-scallop height-cycle time-minimal approach. In other words, the

objective of the optimization process is to find the tool path for minimizing the average cutting forces, scallop heights and cycle time with the user defined preset maximum values or objective weightings.

A 3D scallop model is introduced where initial reference scallop points and scallop heights are estimated to use for scallop height mapping. Reference scallop points are validated with the comparison of the reference cut surface obtained from CAD/CAM software. Cutting force, scallop height and cycle time maps are formed and used further in tool path optimization algorithms. Two multi-criteria tool path optimization routines are offered in this study: firstly a GA based multi-criteria tool path optimization routine is developed upon the previous studies of Zhou and Gen et al. [14] on multi-criteria GA network optimization; secondly a varying objective weighting algorithm based on single-criteria network optimization is offered. For the single-criteria network optimization, MCC-transformed path is developed and compared with known network optimization algorithms such as minimum cost traveling salesman (MCTS) and minimum spanning tree (MST).

In the demonstrated free form surfaces, with the simulation and experimental results, it is shown that optimal paths can be achieved for free form surfaces with the novel approach. Results showed that tool path selection could be optimized depending on the aim of the user, since there is a trade-off criterion between cutting forces, scallop heights and cycle times; for example, lower cutting forces result in longer cycle times.

References

1. **Kaymakci, M., Lazoglu, I., Murtezaoglu, Y.** Machining of Complex Sculptured Surfaces with Feedrate Scheduling. *International Journal of Manufacturing Research, Special Edition on Sculptured Surfaces, Inderscience Publishers,* 2006, 1(2), pp.157-175.

2. **B.U. Guzel, I. Lazoglu.** Increasing Productivity in Sculpture Surface Machining via Off-line Piecewise Variable Feedrate Scheduling Based on the Force System Model. *International Journal of Machine Tools Manufacture.* 2004, Vol. 4, pp. 21-28.

3. **Erdim, H.** *Improving Productivity in Free-form Surface Machining*, M.Sc. thesis, Koç University, 2005.Istanbul.

4. **Lazoglu I., Manav C., Murtezaoglu Y.** Tool path optimization for free form surface machining. CIRP Annals. 2009, 58, pp 101–104.

5. **Martelotti, M.E.** An Analysis of the Milling Process. *Transactions of the ASME.* 1943, 63, pp. 677-700.

6. **Koenigsberger F., Sabberwal A.J.P.,** An Investigation into the Cutting Force Pulsations During Milling Operations. *International Journal of Machine Tool Design and Research.* 1961, 1, pp 15-33.

7 **Armarego E.J.A, Deshpande N.P.** Force Prediction Models and CAD/CAM Software for Helical Tooth Milling Processes, I, *Basic approach and Cutting Analyses, International Journal of Production Research*. 1993, 31, pp 1991-2009.

8. **Yucesan, G. and Altintas, Y.** [ed.] Mechanics of Ball End Milling Process. *Manufacturing Science and Engineering.* New Orleans, USA : ASME Winter Annual Meeting. pp. 543-551. 64.

9. **Armarego E.J.A.,Whitfield R.C.** Computerized End-Milling Force Predictions with Cutting Models Allowing Eccentricity and Cutter Deflections, *CIRP Annals*, 1991, 40, pp 25-29.

10. **Budak E., Altintas Y., Armarego E.J.A.** Prediction of Milling Force Components from Orthogonal Cutting Data.

11. **Yang, M. and Park, H.** The Prediction of Cutting Force in Ball-End Milling. *International Journal of Machine Tools and Manufacturing.* 1991, pp. 41-54.

12. **Lazoglu I., Liang S.Y.** Modeling of Ball-End Milling Forces with Cutter Axis Inclination, *Journal of Manufacturing Science and Engineering, Transactions of the ASME* 2000, 122, pp 3-11.

13. **She Q, Kannasoot N, Jue JP, Kim YC.** On Finding Minimum Cost Tree for Multi-resource Manycast in Mesh Networks. *Optical Switching and Networking.* 2009, 6(1), pp. 29-36.

14. **Zhou G., Gen M.** Genetic Algorithm Approach on Multi-criteria Minimum Spanning Tree Problem. *European Journal of Operational Research.* 1999, 114(1), pp. 141-152.

15. **Weinert K., Enselmann A., Friedhoff J.** Milling Simulations for Process Optimization in the Field of Die and Mold Manufacturing. *CIRP Annals.* 1997, 46(1), pp. 325-328.

16. **Altan T., Lilly B., Yen Y.C.** Manufacturing of Dies and Molds. *CIRP Annals.* 50(2), pp. 404-422.

17. **B, Lauwers.** Efficient NC-Programming of Multiple-Axes Milling Machines through the Integration of Tool Path Generation and NC Simulation. *CIRP Annals.* 2000, 49(1), pp. 367-370.

18. **Castelino K., D'Souza R., Wright P.K.** Toolpath Optimization for Minimizing Airtime during Machining. *Journal of Manufacturing Systems.* 2003, 22(3), pp. 173-180.

19. **A., Rangarajan and D., Dornfeld.** Efficient Tool Paths and Part Orientation for Face Milling. *CIRP Annals.* 2004, 53(1), pp. 73-76.

20. **Lacalle LN, Lamikiz A, Sa´nchez JA, Salgado MA.** Toolpath Selection based on the Minimum Deflection Cutting Forces in the Programming of Complex Surfaces Milling. *International Journal of Machine Tools and Manufacture.* 2007, 47(2), pp. 388-400.

21. **S, Makhanov.** Optimization and Correction of the Tool Path of the Five-Axis Milling Machine. Part 1. Spatial Optimization. *Mathematics and Computers in Simulation.* 2007, 75(5-6), pp. 210-230.

22. **Feng, H.-Y., Su, N.** Integrated toolpath and feedrate optimization for the finishing machining of 3D plane surfaces. *International Journal of Machine Tools & Manufacture*, 2000, 40, pp 1557-1572.

23. **Budak E., Lazoglu I., Guzel B.U.** Improving Cycle Time in Sculptured Surface Machining Though Force Modeling. *CIRP Annals.* 53, 2004, Vol. 1, pp. 103–106.

24. **Lazoglu, I.** Sculpture surface machining: a generalized model of ball end milling force system. *International Journal of Machine Tools & Manufacture.* 2003, 43, pp. 453-462.

25. **Chen, J.-S., Huang, Y.-K., Chen, M.-S.** A Study of the Surface Scallop Generating Mechanism in the Ball-End Milling Process. *International Journal of Machine Tools and Manufacture.* 2005, 45, pp. 1077-1084.

26. **Manav A. C., Akgun E., Lazoglu I.,** Improving free form surface machining performance by ball end milling model. *International Journal of Design Engineering.* 2008, 1(4), pp 434-444.

27. **Manav A. C., Akgun E., Lazoglu I.,** Process optimization of free form surface machining. *International Conference On Machine Design and Production (UMTIK).* 2008.

28. **Monreal, M., Rodriquez, C.A.** Influence of Tool Path Strategy on the Cycle Time of High-Speed Milling. *Computer-Aided Design.* 2003, 35, pp. 395-401.

29. **Kim, B.H., Choi, B.K.** Machining Efficiency Comparison Direction-parallel Tool Path with Contour-parallel Tool Path. *Computer-Aided Design.* 2002, 34, pp. 89-95.

30. **Feng H.-Y., Li H.** Constant scallop height tool path generation for three-axis sculptured surface machining. *Computer Aided Design*. 2002, 34, pp 647-654.

31. **Lee S.-G., Kim H.-C., Yang M.-Y.** Mesh-based tool path generation for constant scallop-height machining. *The International Journal of Advanced Manufacturing Technology.* 2008, 37, pp 15-22.

32. **Agrawal R. K., Pratihar D.K., Choudhury A.R.** Optimization of CNC isoscallop free form surface machining using a genetic algorithm. *International Journal of Machine Tools & Manufacture.* 2006, 46, pp 811–819.

33. **Kim, S.-J., Yang M.-Y.** A CL surface deformation approach for constant scallop height tool path generation from triangular mesh. *The International Journal of Advanced Manufacturing Technology*. 2006, 28, pp 314–320.

34. **Choi Y.-K, Banerjee A., Lee J.-W.** Tool path generation for free form surfaces using Bezier curves/surfaces. *Computers & Industrial Engineering*. 2007, 52, pp 486–501.

35. **Kaymakci, M.** [ed.] *Tool Path Selection and Feed Rate Scheduling Strategies for Complex Sculptured Surfaces.* M.Sc. thesis, Koç University, 2006.Istanbul.

36. **Altintas, Y.** *Manufacturing Automation: Metal Cutting Mechanics, Machine Tool Vibrations, and CNC Design.* s.l. : Cambridge University Press, 2000.

37. **Raidl G.R., Julstrom B. A.** A weighted coding in a genetic algorithm for the degree-constrained minimum spanning tree problem. *Proceedings of the 2000 ACM Symposium on Applied Computing*. ACM Press 2000, pp 440–445.